THESIS FOR THE DEGREE OF DOCTOR OF PHILOSOPHY

Buildings' Transition to Active Nodes: Assessing the Viability of DC Distribution, PV and Battery Storage

Patrik Ollas

Department of Electrical Engineering
Chalmers University of Technology
Gothenburg, Sweden, 2024

Buildings' Transition to Active Nodes: Assessing the Viability of DC Distribution, PV and Battery Storage

Patrik Ollas
ISBN 978-91-8103-033-4

Doktorsavhandlingar vid Chalmers tekniska högskola
Ny serie nr 5491
ISSN 0346-718X

Department of Electrical Engineering
Chalmers University of Technology
SE-412 96 Gothenburg, Sweden
Phone: +46 (0)31 772 1000
`www.chalmers.se`

Printed by Chalmers Reproservice
Gothenburg, Sweden, March 2024

To my family.

ABSTRACT

Historically, buildings have been passive nodes in the electric grid system with one-way power flows. However, with the recent market development of solar photovoltaic (PV) and stationary behind-the-meter battery storage systems, buildings are now transitioning to active nodes, offering bi-directional power flows. Various system topologies and modelling aspects are of interest for these active nodes and their viability. This thesis compares internal building direct current (DC) distribution with the conventional alternating current (AC) distribution for single-family and office buildings. For both building types, the geographical location is altered to examine the effect of PV and load correlation on the DC performance. The energy loss over a year and the loss distribution across various components are examined for three DC topologies, including one with constant power electronic converter (PEC) efficiencies, to quantify the loss discrepancy to experimentally derived PEC efficiency characteristics. Using constant efficiencies for a single-family building underestimates the annual losses by 34% (63 kWh/a). With load-dependant PEC efficiencies and without battery storage, DC operation shows no performance enhancements compared to AC. Depending on the studied case, DC operation results in loss savings, -16.3 to -43.6% with PV and battery.

Two methods are proposed to reduce the grid-tied converter (GC) losses from partial load operation. One method—a modular GC design consisting of a smaller and a larger GC—is modelled for two cases: a single-family building and an office building, and presents an optimal GC size configuration of 15/85%. The loss savings relative to AC operations for a 15/85% configuration are 26% for the single-family building and 15–40% for the office. The savings depend on the office's location and system design (PV and battery sizing). For the offices, the effect on DC loss savings is examined via a parametric sweep by varying PV and battery sizes, with resulting savings up to 40% (-12.8 MWh/a) compared to AC operation. The results highlight the effect of GC sizing on the DC performance, the effect of battery storage, and how the PV and load correlation affects the DC performance.

Furthermore, a battery model is derived from experimental measurements of the cell's current—resistance and open-circuit voltage (OCV)—state-of-charge (SOC) dependencies. The battery model is verified against the measured voltage with good compliance (RMSE<7 mV). Three representations—including the round trip efficiency approximation—are compared for annual battery system losses. The results indicate that the cell's losses—making up 22–45% of losses for the examined case—and that the internal resistance's current dependency is essential for an accurate representation. The loss discrepancy for the round trip approximation varies between -5% to 29%, relative to the experimentally derived representation, depending on the modelled battery size.

The role of PV and battery storage for an airport micro grid is examined in a forward-looking case with electric aviation (EA) and electric vehicles (EVs). Seven scenarios are studied, including four with battery storage and different operation algorithms. One of the algorithms is a novel operation combining self-consumption (SC) and peak power shaving. Compared to the current situation, the techno-economic evaluation shows a significant increase in energy (89.4%) and power (+1 MW) demands from EA and EV. For the nominal battery price and peak power tariff ($\mathbb{C}_t$), the novel operation shows the shortest Payback Period (PBP) of 4.8 years for the battery scenarios. With varying battery prices and peak power tariffs, the sensitivity analysis shows that $\mathbb{C}_t$ can significantly affect the PBP.

Lastly, the effect of PV module operating temperature on performance is empirically evaluated and quantified for seven arrays from annual operation. For the Building–Applied PV (BAPV) c-Si modules, the elevated operating temperature adds 1% to the total losses and 2% for the c-Si Building–Integrated PV (BIPV). Examining the results of SC and self-sufficiency (SS) verifies the correlation between SC and power rating and introduces the correlation between SS and annual yield, considering the effect of system design, level of roof integration and PV cell type. For this case study, comparing two systems with and without battery storage shows the weekly variation in SS and SC and highlights the drawback of single-objective dispatch.

Keywords: Solar photovoltaic, Battery Storage, Direct Current, Buildings, Energy Management

LIST OF PUBLICATIONS

This thesis is based on the following publications:

I. **Patrik Ollas**, Torbjörn Thiringer, Mattias Persson, Caroline Markusson, “Battery loss prediction using various loss models: A case study for a residential building”. Published in *Journal of Energy Storage* (2023).

II. **Patrik Ollas**, Sara Ghaem Sigarchian, Hampus Alfredsson, Jennifer Leijon, Jessica Santos Döhler, Christoffer Aalhuizen, Torbjörn Thiringer, Karin Thomas, “Evaluating the role of solar photovoltaic and battery storage in supporting electric aviation and vehicle infrastructure at Visby Airport”. Published in *Applied Energy* (2023).

III. **Patrik Ollas**, Torbjörn Thiringer, Caroline Markusson, “Energy Loss Savings Using Direct Current Distribution in a Residential Building with Solar Photovoltaic and Battery Storage”. Published in *Energies* (2023).

IV. **Patrik Ollas**, Torbjörn Thiringer, Huijuan Chen, Caroline Markusson, “Increased photovoltaic utilisation from direct current distribution: Quantification of geographical location impact”. Published in *Progress in Photovoltaics: Research and Applications* (2021).

V. **Patrik Ollas**, Torbjörn Thiringer, Mattias Persson, “Enhanced DC building distribution performance using a modular grid-tied converter design”. *Submitted manuscript.*

VI. **Patrik Ollas**, Jon Persson and Peter Kovacs, “Technical Performance Evaluation of BIPV and BAPV Systems”. Published in *38th European Photovoltaic Solar Energy Conference and Exhibition* (2021).

VII. **Patrik Ollas**, Jon Persson and Peter Kovacs, “Effect of Energy Storage on Self-Consumption and Self-Sufficiency: A Field Study in a Nordic Climate”. Published in *38th European Photovoltaic Solar Energy Conference and Exhibition* (2021).

Other publications by the author, not included in this thesis, are:

VIII. **Patrik Ollas**, Torbjörn Thiringer, Niclas Samuelsson and Ahmed Sunjaq, “Reducing Electrical Losses in Buildings: A Study of Load-Side DC/DC Converter Topologies for Low–Power Appliances”. *IEEE PES Innovative Smart Grid Technologies, Europe. IEEE, 2023* (2023).

IX. **Patrik Ollas**, Jon Persson, Caroline Markusson and Usama Alfadel, “Impact of battery sizing on self-consumption, self-sufficiency and peak power demand for a low energy single-family house with PV production in Sweden”. *2018 IEEE 7th World Conference on Photovoltaic Energy Conversion (WCPEC) (A Joint Conference of 45th IEEE PVSC, 28th PVSEC & 34th EU PVSEC)* (2018).

X. **Patrik Ollas**, Caroline Markusson, Jörgen Eriksson, Huijuan Chen, Markus Lindahl and Torbjörn Thiringer, “Quasi-Dynamic Modelling of DC Operated Ground-Source Heat Pump”. *BuildSIM-Nordic 2020* (2020).

XI. Hampus Alfredsson, **Patrik Ollas**, Sara Ghaem Sigarchian, Christoffer Aalhuizen, Jennifer Leijon and Karin Thomas, “Transportation Goes Electric – Exploring the Potential of Smart Charging Strategies for Airports”. *36th International Electric Vehicle Symposium and Exhibition (EVS36) Sacramento, California, USA, June 11-14* (2023).

XII. Jennifer Leijon, Jens Hagman, Hampus Alfredsson, Sara Ghaem Sigarchian, **Patrik Ollas**, Christoffer Aalhuizen, Jéssica Santos Döhler, Cecilia Boström and Karin Thomas, “Airports with increased electrification–an ongoing project with case studies in Sweden”. *35th International Electric Vehicle Symposium and Exhibition (EVS35)* (2022).

MY CONTRIBUTIONS TO THE PAPERS

I contributed with the following in the included papers:

Paper I: I co-developed the conceptualisation, did most of the data curation and result analysis, and wrote the evaluation software and the original draft paper.

Paper II: I co-developed the conceptualisation, did all the modelling—except the generation of EV, EA and PV profiles—and performed the formal analysis and evaluation, and wrote the original draft paper.

Papers III: I developed the conceptualisation, wrote the evaluation software, performed the result analysis and investigation, and wrote the original draft paper.

Papers IV: I co-developed the conceptualisation, wrote the evaluation software, using inputs from the buildings' energy demands, and performed the result analysis and investigation, and wrote the original draft paper.

Papers V: I developed the conceptualisation, battery and converter energy managements, wrote the evaluation software—using inputs from the office buildings' energy demands—and performed the analysis and investigation, and wrote the original draft paper.

Papers VI–VII: I co-developed the conceptualisation, wrote the evaluation software, performed the formal analysis and investigation, and wrote the original draft paper.

ACKNOWLEDGEMENTS

I want to express my deepest gratitude to Professor Torbjörn Thiringer for his unwavering support, invaluable guidance, and encouragement throughout the entire journey of this thesis. His expertise, patience, and insightful feedback have been instrumental in shaping this work.

I am also immensely grateful to my supervisors, Caroline Markusson and Mattias Persson at RISE, for their valuable suggestions, constructive criticism, and time dedicated to reviewing this thesis.

I thank the Swedish Energy Agency for their financial support, which made this research possible.

Special thanks to my co-authors and colleagues for their collaboration, stimulating discussions, and moral support throughout.

I owe a debt of gratitude to my family for their unwavering love, encouragement, and understanding throughout this endeavour. Their sacrifices and belief in me have been my greatest source of strength.

Lastly, I am thankful to all those whose names may not appear here but have contributed in various ways to the completion of this thesis.

This work would not have been possible without the collective support and encouragement of all those mentioned above. Thank you from the bottom of my heart.

Acronyms

AC	Alternating current
BAPV	Building–Applied PV
BAU	Business As Usual
BESS	Battery Energy Storage System
BIPV	Building–Integrated PV
DC	Direct current
DoD	Depth-of-discharge
DOO	Dual-Objective Operation
EA	Electric Aviation
EV	Electric Vehicle
GC	Grid-tied Converter
LCC	Life-Cycle Cost
MO	Multi–objective (battery dispatch)
OC	Operational Cost
OCV	Open–circuit voltage
$\mathbf{P}/p$	Rated ($\mathbf{P}$) or instantaneous (p power)
PBP	Payback period
PEC	Power electronic converter
PLS	Proposed load-distribution
PR	Performance Ratio
PV	Solar photovoltaic

RBC	Relative Battery Capacity
RBS	Relative Battery Size
SC	Self-consumption
SOC	State–of–charge
SS	Self-sufficiency
STC	Standard Test Conditions

Symbols

β	Grid-tied converter threshold share
δ	PV module temperature coefficient
δ_{soc}	Step-wise adjustment of $soc^{\mathrm{sv}}_{\mathrm{min}}$
κ_{PV}	PV utilisation
κ_{system}	System efficiency
χ	Size ratio of smaller grid-tied converter
ψ	Building main fuse
$\mathbb{C}_{\mathrm{buy}}$	Price of bought electricity (from the grid)
$\mathbb{C}_{\mathrm{deg}}$	Monetised battery degradation
$\mathbb{C}_{\mathrm{net}}$	Net electricity bill
$\mathbb{C}_{\mathrm{sell}}$	Revenue from sold electricity (to the grid)
$\mathbb{C}_t$	Peak power tariff
$\mathbb{S}$	Scenarios from parametric sweep of β and χ
A_h	Battery capacity throughput
c_k	Temperature correction term

$f(s)$	Efficiency as a function of loading
$\mathbf{DC}^{\star}$	DC reference ($\psi = 16$ A and $\chi = 0\%$)
$\mathbf{E}_{\text{batt}}$	Battery energy capacity
$\mathbf{i}_{\text{batt}}$	Battery current
$\mathbf{i}_{\text{cell}}$	Cell current
$\mathbf{I}_{\text{C}}^{\text{batt}}$	Battery investment cost
$\mathbf{m}_{\text{strings}}$	Number of of parallel battery strings
$\mathbf{n}_{\text{cell}}$	Number of series connected battery cells
$\mathbf{P}_{\text{lim}}^{h}$	Grid-tied converter power threshold
$\mathbf{P}_{\text{max}}^{\text{conv}}$	Power constraint for battery charge/discharge
p_{net}	Grid net power
p_{sh}	Peak shaving power
q_{batt}	Battery charge level (Ah)
$\mathbf{Q}_{\text{batt}}^{\text{rated}}$	Battery rated capacity (Ah)
$\mathbf{Q}_{\text{cell}}$	Battery cell capacity (Ah)
q_{loss}	Battery capacity loss from degradation
$\mathbf{R}_0$	Battery cell internal resistance (fixed)
$\mathbb{R}$	Battery cell series resistance; $\mathrm{R}_0 \vee r(i_{\text{cell}})$
$r(i_{\text{cell}})$	Battery cell resistance as a function of current
$\mathbf{r}_{\text{PV}}$	PV to load share ratio
$\mathbf{r}_s$	Spearman's rank correlation coefficient
$soc_{\text{min}}^{\text{sv}}$	Seasonal variation of minimum SOC
t_m	Measured (PV) module temperature

$\mathbf{T}_m^{\text{avg}}$	Irradiance-weighted (PV) module temperature
$u_{\text{cell}}^{\star}$	Measured cell voltage
$\mathbf{U}_{\text{nom}}^{\text{batt}}$	Nominal battery voltage
$u_{\text{ocv}}^{\text{lin}}$	Linear approximation of OCV as a function of SOC
$u_{\text{ocv}}^{\text{mean}}$	OCV approximation of mean from charge and discharge

Contents

Part I

OVERVIEW

CHAPTER 1

INTRODUCTION

1.1 Background

From 2010 to 2021, the energy use in buildings increased from 115 EJ to 135 EJ, representing 30% of the global final energy usage [1]; out of which, 35% was electricity (+30% from 2010). EU's 'Fit for 55' package aims for a 55% net greenhouse gas emission reduction by 2030 [2], with energy usage in buildings as one targeted sector. Until recently, buildings have been passive nodes with a one-way power flow in the electric grid. However, given the market development and striving for resilience, environmental awareness, and economic prosperity, this momentum has shifted buildings to active nodes, offering bi-directional power flows and enhanced grid involvement.

In recent years, the market for behind-the-meter electrical storage has grown significantly, partly driven by the development in the solar photovoltaic (PV) market [3]. Figure 1.1 shows the historical and forecasted cumulative power per technology for 2010–2027 [4]. By 2027, PV is expected to surpass coal and become the largest power source in the world. The homeowners' incentive for coupling battery storage with PV generation is partly associated with the ambition to increase the self-consumed share of locally generated energy.

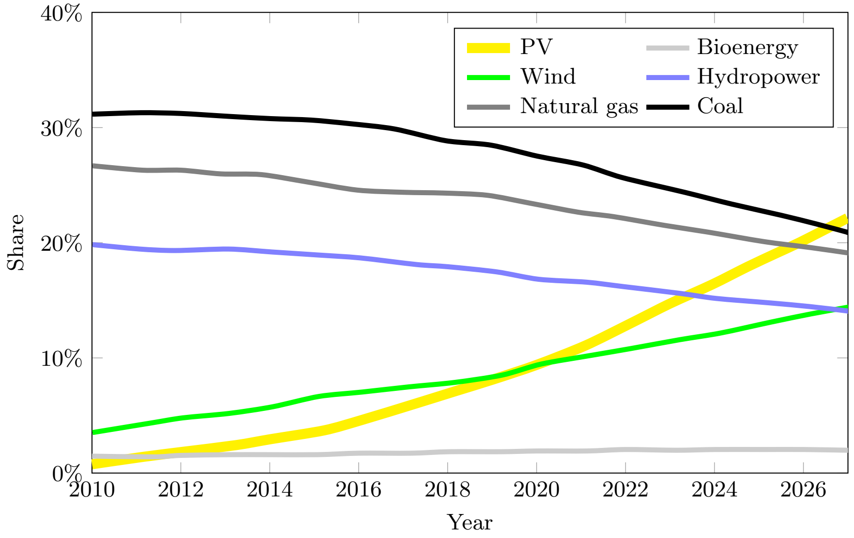

Figure 1.1: Current and trajectory of cumulative power capacity shares by technology, 2010–2027 [4].

This thesis examines the viability of DC building distribution, PV and behind-the-meter battery storage systems. It highlights loss discrepancies and optimises DC distribution performance to minimise losses. The work develops a battery model based on experimental measurements. It evaluates various battery operation algorithms for microgrid applications, demonstrating economic viability and the importance of accurately representing battery characteristics. Additionally, it examines the effect of PV module operating temperature on performance and system design considerations.

AC and DC Building Distribution

The interest in DC systems has gained more momentum following the latest technological development in power electronics [5] and the increased penetration of PV and battery storage [6]. As PV modules generate DC and batteries operate with DC, a DC building distribution topology enables efficient interaction with fewer power semiconductors in the current path for voltage conversion. Furthermore, almost all electronic loads in buildings are

DC-operated [7]. The expected growth in electric vehicles, which are also DC-operated, is an additional motivator for DC in and adjacent to buildings [8]. Today's conventional alternating current (AC) topologies require conversions between AC and DC before the final user stage, generating losses. Adopting DC distribution reduces or avoids some conversion losses, thereby increasing the system's performance and resource efficiency.

In an expert survey among market stakeholders [9], more research on DC distribution in buildings was the top priority identified to enhance market adoption. As pointed out in previous works, e.g., [10]–[12], this research topic requires more comprehensive efforts, deepening the detail level of modelling to enable accurate comparisons. A comprehensive review article by Gelani et al. [13] concludes that the findings from previous works are conflicting, and the combined efforts fail to give a verdict on the feasibility of DC operation and under what circumstances DC is favourable.

The work in [11] quantified the loss sources for residential DC distribution and concluded that the bi-directional grid-tied converter (GC) is the primary loss source. The same conclusion is made in [14], and despite modelling of optimal converter sizing, the loss share exceeds 30%. In related works, the GC loss shares comprise 65% [Paper IV] or 60% [Paper III] when accounting for the efficiency characteristics at partial loading. As acknowledged in [11], the GC is optimised for high powers but often operates at partial loading, resulting in poor efficiency. The work in [15] performs a sensitivity analysis on the essential modelling parameters and a quantitative comparison of AC vs DC distribution and concludes that the GC's efficiency has the highest effect on the relative comparison.

Residential Battery System Modelling

In literature related to PV and battery systems modelling, works are found on the system's techno-economic performance when adding battery storage; evaluated for the increased self-consumption (SC) and self-sufficiency (SS), e.g., [16]–[19] or the profitability [20]–[22]. Typically, these works use a constant round trip efficiency, ranging from 85% [23] to 98% [24] when dealing with battery-associated losses. Other studies on PV and battery systems identify the round trip efficiency as a critical parameter for the system's performance [25]–[27]. As pointed out in [23], battery system losses originate from the battery itself (mainly the cells) and the power electronic converter (PEC), both with load-dependent efficiency characteristics. In many cases, the PECs and battery losses are represented by a constant value, e.g., [16], [17], [23], [26]. A constant efficiency offers a static and low-level complexity option but may not accurately reflect the dynamic operation observed in reality. Eventually, this simplification could lead to wrongful performance estimations as it misses out on the loss variations both in the battery cells and the converter.

Methods and models to predict the battery's current and voltage relation are available in the literature to capture the loss characteristics of the battery cells under dynamic operation. Examples of this are found for electrical vehicles (EVs) using a resistance [28] or resistance network representations [29], [30]. These representations are applicable when studying fast phenomena (>1 Hz). However, for buildings—with less rapid changes—it is proven in [31] that a single resistance is sufficient to represent the voltage–current relation in a battery cell for slower current changes. The work in [31] also acknowledges the scarcely treated subject of relating the battery's internal resistance variations to the current level.

Airport Micro Grid Modelling

In the EU, aviation emissions in 2017 accounted for 3.8% of the total CO_2 emissions, making it the second largest emitter of transport greenhouse gas after road transport [32]. If global aviation were a country, it would rank among the top ten emitters. Before the Covid pandemic, the International Civil Aviation Organization forecasted that the emissions could triple by 2045 compared to 2015 [33].

Aviation is vital for urban development [34], and electric aviation (EA) could significantly reduce the environmental impact and eliminate aviation-originated CO_2 and non-CO_2 emissions while reducing noise. With today's technology, short-haul flights (less than 1500 km) are best suited for electrified aircraft with zero-operation emissions. In 2019, these fossils-driven short-haul flights accounted for one-third of the CO_2 emissions [35].

The effect of transport electrification on the airport's energy demand is demonstrated in [36], [37]. The work in [36] replaces all global flights up to 600 nautical miles with EA and estimates an increased energy demand of 112–344 TWh (0.6–1.7% of 2015 global consumption). From a study of the O'Hare International Airport, a portion of the flights are replaced by hybrid electric aircraft and the change in electricity demand was studied [37]. The results report a substantial increase in the energy demand, requiring airport grid upgrades.

Airports require vast and flat areas for their operation, with large open fields along the runway, offering safe take-offs and landings, and usually with a sound buffer area to reduce noise pollution. The energy consumption of a larger airport is equivalent to a six-digit population city with around-the-clock energy demand, putting significant stress on the electricity grid. Potential grid stress relief is deploying PV arrays in open, flat, and, in many cases, shading-free spaces. The work in [38] analyses which sustainability practices are used at airports today. Ten indicators, including Energy Management, were identified, where alternative and renewable energy sources, such as solar energy, were categorised as one sub-indicator. The works in [39], [40] highlight the advantages of PV airport deployment and conclude that the benefits of PV depend on the timely correlation with load demand. As highlighted in [41], stationary battery energy storage could further enhance the PV benefits by reducing grid energy demand, electricity cost, and access to renewable energy.

1.2 Aims

The main aim of this work is to assess the viability of DC building distribution, PV and battery storage for active node buildings in the electric power system. The aim can be divided into the following goals:

i) evaluate the loss saving potential from DC building distribution and present measures to enhance the DC operational performance,

ii) examine the techno-economic effect of PV and battery inclusion for DC performance, and the effect of PV and load correlation,

iii) investigate suitable battery representations for stationary residential battery systems, including accounting for the resistance dependence on the current level, and,

iv) quantify the role of PV and battery storage systems in an airport micro grid energy infrastructure.

1.3 Identified Research Gaps

Building DC Distribution

Typical in previous works, e.g., [42]–[45], is constant PEC and battery efficiencies. This approach neglects the load-dependent characteristics, a decisive factor for an accurate comparison [46]–[48]. Despite acknowledging the importance of the PEC characteristics, the work in [49] only includes a variety of constant efficiency values when quantifying the effect of the converter characteristic. Studies which acknowledge the load dependency are, e.g., [11], [14], [50], where the presented efficiency curves only include part of the PEC's loading range and thus make it unclear how the partial loading range is treated. Using constant efficiency or neglecting the entire operating range leads to inaccurate results. Examples of varying efficiency characteristics and their effect on system performance are examined in [48], [49], [51]. However, these studies only present the effect on a single day's performance [48], [51] or the effect of various constant efficiency values [49]. While the referred studies leave room for improvement, they demonstrate the need for proper PEC modelling for a fair and accurate comparison.

In addition to constant efficiency, another gap is the access and usage of data profiles (PV and load) [13]. Several of the previous studies use synthetic profiles for the full-year comparison, and these are either based on average profiles [11], [42], [48], [49] or modelled using building and occupant-specific factors [14]. Averaging data leaves out peaks and dynamic variations while modelling synthetic data using performance indexes, e.g., internal heat dissipation (W/person or appliance) and ventilation flow rates (l/s), often resulting in repetitive profiles that may not reflect actual behaviour. Another vital aspect is the data period, where comparisons based on a single day's operation [48], [50], [52] neglect the influence of seasonal variations and thus do not capture the annual performance [53], [54]. With these arguments, an accurate comparison requires full-year, measured PV and load demand data.

Furthermore, other studies [11], [13] identify the need for detailed modelling of the battery system losses and dynamic load behaviour, which previous important works, e.g. [11], [42], [55] lack.

A modular GC converter design for partial-load reduction is one measure to reduce the loss contribution as suggested in [46], [47]. Several works exist on modular converter design. The work in [56] uses a genetic algorithm efficiency optimisation for current sharing among three parallel DC/DC converters in a low-voltage DC application. The work in [57] compares linear droop operation for an islanded micro grid with an improved primary regulation using non-linear droop control. Other parallel converters load-sharing examples in DC micro grids are [58], [59], focusing on the converters' interplay and power qualities. The work in [60] applies hierarchical control management on parallel-operated DC/DC converters in a hardware-in-the-loop simulation on four converters to demonstrate the potential system improvements. However, to the best of the author's knowledge, studies of modular converter operation are lacking in applied cases of DC distribution systems targeting the GC's operation, including the effect of varying loading conditions and a quantified performance gain. A related approach for loss minimisation is presented in [52], where the energy management system chooses the operation mode with the lowest losses. Real-time monitoring of the PV supply load demand and battery status dictate the power flows. However, it is not described how the PEC losses are accounted for, which are essential aspects of the loss analysis.

Table A.1 gives an overview of related journal publications on DC energy savings in buildings concerning PEC and battery efficiencies (load-dependant (f(s)) or fixed), data profiles (synthetic or measured), inclusion of DC sources (PV and battery), and studied period (single day(s) or annual operation). The last row in the table relates Papers III–V and the unpublished work for the office buildings included in this thesis to these previous efforts.

Residential Battery System Modelling

The work in [61] performs a battery storage size determination for a PV and battery system and acknowledges the limitation of using a constant round trip efficiency, concluding that a dynamic approach is preferred in future studies. The work in [23] acknowledges the non-linear power-dependent characteristic but still uses a constant round trip efficiency for their profitability study. Despite the comprehensive techno-economic assessment in [62], the authors use a constant round trip characteristic. The works in [25], [63] use the battery's voltage and state-of-charge (SOC), but it is not clear whether they consider the battery's cell losses. A detailed loss analysis of twelve PV and battery systems in a laboratory setup is presented in [64]. The measurements include a single sample day extracted from synthetic data and scaled to full-year operation. Results include efficiency curves for different power conversion pathways and conclude that the dominating losses originate from the PECs and emphasise the effect of partial load operation. However, the referred work treats the internal battery losses with a constant round trip efficiency value. The work in [65] lists previous works on PV and battery systems and concludes that the majority use constant values to represent the battery system's (cells and converter) efficiency, e.g., [66]–[68]. The work in [65] identifies studies which acknowledge the load-dependency and model the efficiency characteristics of the PEC, e.g., [69]–[72]. However, the referred studies, including [65], treat the battery internal losses using a constant round trip efficiency.

A critical research gap is the need for studies accounting for the effect of the battery system's partial load operation, considering the load-dependent efficiency characteristics from both the PEC and battery cells and their impact on the system's performance. Another area for improvement in the literature is the limited data sheet descriptions. Often, a single resistance value is given, sometimes with a frequency where this value is valid, and sometimes not. So, an essential question is: How valid is such a value for loss representations?

Airport Micro Grid Modelling

The work in [73] reviewed the concept and potential for micro grids and acknowledged that the airport's cross-sector coupling could benefit from a micro grid implementation. The refereed study also concludes that airports are the least explored transport-related sector addressing the micro grid concept and the electrification challenge. The works in [74], [75] also acknowledge the need for airport micro grid studies. In [74], the effect of vehicle-to-grid (V2G) and EA charging strategies are studied for an airport micro grid with PV and hydrogen storage. The work in [39] uses a mixed integer linear programming (MILP) optimisation to compare the techno-economic performance of five airport energy configuration systems, including combinations of PV, battery energy storage system (BESS) and hydrogen storage. The study excludes EA but concludes that cost and emission savings are achieved when implementing PV and storage by reducing electricity from the grid. In [76], a modified MILP is used to evaluate an airport micro grid's techno-economic potential with PV, BESS and a backup diesel generator. Similar to [39], [76], the work in [77] uses a MILP based on life cycle theory to evaluate an airport's techno-economic feasibility and resilience, excluding the electricity usage at the terminals. Typical for the reviewed studies on airport micro grid operation is using a single-objective storage (BESS and hydrogen) dispatch to maximise SC [39], [74]. The work in [78] models the optimal airport battery sizing to support EA charging (single-objective) and acknowledges the potential of revenue-stacking operation. Examples of operational shortcomings of BESS single-objective operation are shown through simulations in [79], highlighting the poorly managed operation when relying solely on PV surplus. As identified in [80]–[83], single-objective operation limits the BESS's full potential, thus leaving out technical and economic possibilities.

Missing from the available literature on airport micro grid studies are works considering the combined and multi-facilitated energy infrastructure, including EA and EV charging, PV generation and BESS. Works including BESS typically use single-objective operations and thus limit the full BESS potential. This work targets the identified research gaps with the following specific contributions:

i) holistic airport micro grid modelling, including EA, EV, PV and BESS,

ii) exploring the techno-economic effect of varying BESS operations and

iii) presenting a novel revenue-stacking multi-objective (MO) battery dispatch operation.

1.4 Contributions

The believed to be novel contributions from this work—with reference to the included paper—are:

1. Quantified discrepancy when using constant and load-dependent power electronic converter efficiencies in building loss analysis [Papers III and IV],
2. Determining the effect on DC loss savings from PV and load correlation [Papers IV and V],
3. Novel methods for grid-tied converter partial-load elimination [Paper V],
4. Quantified loss discrepancies of three battery system loss representations and their effect on the system's performance [Paper I],
5. Derived experimentally supported battery cell and power electronic loss models [Paper II],

6. Quantified techno-economic effect from various battery dispatch operations for an airport micro grid energy system [Paper II], and

7. Novel revenue-stacking MO battery dispatch for combined SC and peak shaving operation [Paper II],

8. Quantified effect of module operating temperature on various PV system types and installations from field evaluation [Paper VI],

9. Empirically verified effect of battery single-objective operation in a Northern climate, and quantified enhancement of self-consumption and self-sufficiency [Paper VII].

CHAPTER 2

Theoretical Framework

This chapter introduces the theoretical framework for the battery (losses and current–voltage characteristics), the techno-economic evaluation indexes and the building's electrical losses.

2.1 Battery Model

An equivalent battery circuit model is shown in Fig. 2.1 for n number of parallel RC links. This model is typically used when studying a fraction-of-a-second temporal resolution [84], [85]. In this work, a simplified circuit model is used, neglecting the series inductance (L) and the parallel-connected resistance and capacitor elements (RC) since the temporal resolution of the available data is coarse enough to be represented by full polarisation [47]. Figure 2.2 shows the resulting *Rint* battery circuit model [86] used in this work. This model consists of an ideal voltage source to represent the open-circuit voltage (OCV), u_{OCV}, and a series resistance, $\mathbb{R}$, which describes the cell's internal ohmic resistance. The cell's terminal voltage, u_{cell}, is approximated as [87]

$$u_{\text{cell}}(t) = u_{\text{OCV}}(\text{SOC}) + i_{\text{cell}}(t)\mathbb{R} \tag{2.1}$$

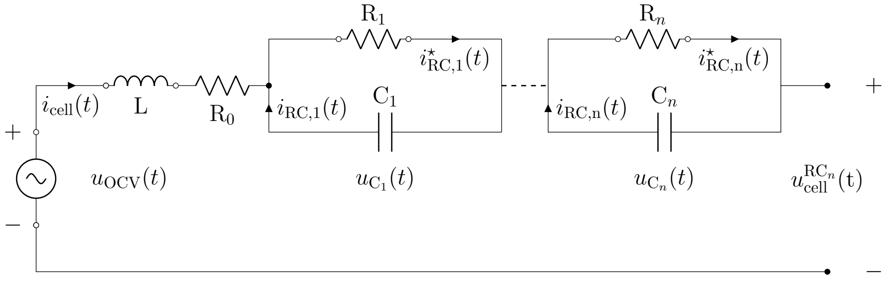

Figure 2.1: Principle design of an equivalent battery circuit with inductance, L, series resistance, R$_0$, and n parallel circuits with resistance, R, and capacitance, C.

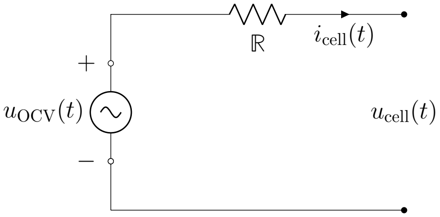

Figure 2.2: Simplified equivalent battery circuit model.

where i_{cell} is the battery cell's current. The representation in (2.1) neglects the hysteresis and voltage measurement noise. In case of m parallel connected strings ($\mathrm{m_{strings}}$) and an assumed cell uniformity, the cell current in (2.1) is calculated as

$$i_{\mathrm{cell}}(t) = \frac{p_{\mathrm{batt}}(t)}{u_{\mathrm{batt}}(t)} \frac{1}{\mathrm{m_{strings}}} \tag{2.2}$$

where p_{batt} and u_{batt} are the battery power and voltage, respectively. The number of parallel strings, $\mathrm{m_{strings}}$ is calculated as

$$\mathrm{m_{strings}} = \frac{\mathrm{E_{batt}}}{\mathrm{U_{nom}^{batt}} \mathrm{Q_{cell}}} \quad \mathrm{m_{strings}} \in \mathbb{N} \tag{2.3}$$

where $\mathrm{E_{batt}}$ is the battery's energy capacity, $\mathrm{U_{nom}^{batt}}$ the nominal battery voltage, and $\mathrm{Q_{cell}}$ the cell capacity (in Ah). The battery energy capacity is given as

$$\mathrm{E_{batt}} = \mathrm{U_{nom}^{cell}} \mathrm{n_{cell}} \mathrm{Q_{cell}} \mathrm{m_{strings}} \tag{2.4}$$

where $\mathrm{n}_{\mathrm{cell}}$ is the number of series-connected cells. The scaling from battery cell to pack level is done by first defining the nominal battery voltage, $\mathrm{U}_{\mathrm{nom}}^{\mathrm{batt}}$. The required number of series-connected cells, $\mathrm{n}_{\mathrm{cell}}$ is then calculated from

$$\mathrm{n}_{\mathrm{cell}} = \frac{\mathrm{U}_{\mathrm{nom}}^{\mathrm{batt}}}{\mathrm{U}_{\mathrm{nom}}^{\mathrm{cell}}} \tag{2.5}$$

where $\mathrm{U}_{\mathrm{nom}}^{\mathrm{cell}}$ is the cells nominal operating voltage.

The battery's operating voltage is determined by the OCV, which is a function of the battery's state-of-charge (SOC). The battery's SOC is a representation of the charge content and calculated as

$$\mathrm{SOC}(t) = \frac{q_{\mathrm{batt}}(t)}{\mathrm{Q}_{\mathrm{batt}}^{\mathrm{rated}}} \equiv \frac{\int i_{\mathrm{batt}}(t)dt}{\mathrm{Q}_{\mathrm{batt}}^{\mathrm{rated}}} \tag{2.6}$$

where $q_{\mathrm{batt}}(t)$ and $\mathrm{Q}_{\mathrm{batt}}^{\mathrm{rated}}$ are the charge level and rated capacity, respectively.

Battery Loss Representation – Constant Ohmic Resistance

One way of representing the battery's losses is to base them on the internal resistance, R, and current [88]. Assuming that the total battery current, i_{batt}, is divided equally on all parallel strings, the power loss as a function of the cell current, is calculated as

$$p_{\mathrm{loss}}^{\mathrm{R_0}}(t) = \mathrm{R}_0 i_{\mathrm{cell}}(t)^2 \mathrm{n}_{\mathrm{cell}} \mathrm{m}_{\mathrm{strings}} \tag{2.7}$$

where, R_0 is the cell's constant internal resistance and $\mathrm{n}_{\mathrm{cell}}$ the number of series-connected cells per string. With this approach, the battery's ohmic losses, $p_{\mathrm{loss}}^{\mathrm{R_0}}$ are related to the current.

Battery Loss Representation – Dynamic Resistance

A battery has an internal resistance dependency as a function of its current [89], [90]. For this representation, the current-dependent resistance is found through the voltage–current ratios at different charge and discharge rates (C-rates), making it possible to establish the internal resistance variation per cell as a function of current. The current-dependent resistance, $r(i_{cell})$, is calculated using the following relation

$$r(i_{\text{cell}}) = \frac{u_{\text{cell}}^{\text{ch}}(i_{\text{cell}}) - u_{\text{cell}}^{\text{dis}}(i_{\text{cell}})}{2i_{\text{cell}}(t)} \tag{2.8}$$

where $u_{\text{cell}}^{\text{ch}}(i_{\text{cell}})$ and $u_{\text{cell}}^{\text{dis}}(i_{\text{cell}})$ are the charge and discharge voltages respectively at a certain SOC level for the current i_{cell}. The cell losses are then calculated using (2.7) and considering the variation in the internal resistance as a function of current as

$$p_{\text{loss}}^{r(i_{\text{cell}})}(t) = r(i_{\text{cell}}) i_{\text{cell}}(t)^2 \mathrm{n}_{\text{cell}} \mathrm{m}_{\text{strings}}. \tag{2.9}$$

Using (2.9), the loss determination utilises the fact that the loss varies with the current squared and the current-dependant resistance from (2.8).

Battery Loss Representation – Round Trip Efficiency

A fixed round trip efficiency is commonly used in the applied building energy genre. Examples of this are presented in technical studies of solar photovoltaic and battery systems [91]–[93]. Here follows a brief definition of these relations.

Constant charge and discharge efficiency's, η_{ch} and η_{dis} respectively are defined in [94], [95] as

$$\eta_{\text{ch}}(t) = \frac{\Delta Q(t)}{Q_{\text{ch}}(t)} \tag{2.10}$$

$$\eta_{\text{dis}}(t) = \frac{Q_{\text{dis}}(t)}{\Delta Q(t)} \tag{2.11}$$

where $\Delta Q(t)$ is the change in battery energy capacity, and $Q_{\text{ch}}(t)$ and $Q_{\text{dis}}(t)$ the charged and discharged energies, respectively. The round trip efficiency, η_{RT}, without considering any throughput dependency, is then defined from (2.10) and (2.11) as

$$\eta_{\text{RT}} = \eta_{\text{dis}} \times \eta_{\text{ch}} \equiv \frac{Q_{\text{dis}}}{Q_{\text{ch}}}. \tag{2.12}$$

The battery losses using a constant round trip efficiency and identical start and end SOCs, are given as the difference in charge and discharge energies as

$$\mathrm{E}_{\text{loss}}^{\text{fixed}} = \int_0^T p_{\text{batt}}^{\text{ch}}(t)\mathrm{d}t - \int_0^T p_{\text{batt}}^{\text{dis}}(t)\mathrm{d}t. \tag{2.13}$$

Battery Degradation

Battery ageing consists of calendar and cycle ageing, where the former depends on time, temperature and SOC, and the latter also on the operation, e.g., the number of equivalent cycles, depth of discharge (DoD) and C-rate [96].

Based on the power law equation introduced in [97], the work in [98] developed a cycle degradation model for a graphite-LiFePO$_4$ battery cell. The model considers the operating temperature, time, depth of discharge (DoD) and discharge rate to calculate the cell's capacity fade. Derived from the power law equation, the work in [98] replace the time dependency for capacity throughput (A_h) and define the capacity loss ($q_{\text{loss}}(t)$) as

$$q_{\text{loss}}(t) = \mathrm{B} \exp\left(\frac{-\mathrm{E}_a}{\mathrm{R}_g \mathrm{T(K)}}\right) A_h(t)^{\mathrm{z}} \tag{2.14}$$

where R_g is the gas constant, T(K) is the absolute temperature, and z is the power law factor. The pre-exponential factor, B, and the activation energy, E_a, are parameterized from experimental tests for different C-rates and operating temperatures in [98]. The capacity throughput (A_h) is calculated as

$$A_h(t) = n(t) \cdot \mathrm{DoD} \cdot \mathrm{Q}_{\text{cell}} \tag{2.15}$$

where $n(t)$ is the cycle number.

2.2 Economic Performance Indexes

For grid-connected buildings with decentralised energy generation, the net electricity bill, $\mathbb{C}_{\text{net}}(t)$, is calculated as,

$$\mathbb{C}_{\text{net}}(t) = \mathbb{C}_{\text{sell}} e_{\text{sell}}(t) - \mathbb{C}_{\text{buy}} e_{\text{buy}}(t) \tag{2.16}$$

where $\mathbb{C}_{\text{sell}}$ and $\mathbb{C}_{\text{buy}}$ are the revenue from sold and price of bought electricity, respectively, and $e_{\text{sell}}(t)$ and $e_{\text{buy}}(t)$ the hourly energy quantities.

The payback period (PBP) measures the time to recoup an initial investment cost ($\mathrm{I_C}$) via the generated cash flows. In its simplest form, PBP is calculated as,

$$\mathrm{PBP} = \frac{\mathrm{I_C}}{\mathrm{CF}} \tag{2.17}$$

where CF is the net cash flow, and without considering of the time value of money.

The Life-Cycle Cost (LCC) is calculated from the investment cost and the present worth value of the operational costs (OC) as

$$\mathrm{LCC} = \mathrm{I_C} + \mathrm{UPV} \times \mathrm{OC}. \tag{2.18}$$

The Uniform Present Value (UPV), for N years of equal cash flows and with a discount rate, r, is calculated as [99]

$$\mathrm{UPV} = \frac{(1+r)^N - 1}{r(1+r)^N}. \tag{2.19}$$

The product UPV×OC gives the Lifetime Operating Cost (LOC) for N years with a discount rate r.

The battery degradation, $q_{\mathrm{loss}}(t)$ from (2.14), impose a cost of battery usage calculated from the initial investment ($\mathrm{I_C^{batt}}$) as [100], [101]

$$\mathbb{C}_{\mathrm{deg}} = \mathrm{I_C^{batt}} \int^T q_{\mathrm{loss}}(t)\mathrm{d}t \quad t \in T. \tag{2.20}$$

This approach is commonly used in the literature, e.g., [102], [103], with a constant $\mathbb{C}_{\mathrm{deg}}$ throughout the BESS life time.

2.3 Self-consumption and Self-sufficiency

The quantity of self-consumed electricity from PV generation ($M(t)$) is defined as [104]

$$M(t) = \min\left[L(t); P(t) + S(t)\right] \tag{2.21}$$

where $L(t)$ is the load demand, $P(t)$ is the PV generation, and $S(t)$ the battery charge and discharge powers[1]. Integrating (2.21) over time, T, gives the SC share as

$$\vartheta_{\mathrm{SC}} = \int^T \frac{M(t)}{P(t)} dt. \tag{2.22}$$

---

[1] $S(t)$ is defined positive for discharge.

The definition in (2.22) is true if there is no interaction between the battery and the grid. If the battery is allowed to interact with the grid, (2.22) expands to [105]

$$\vartheta^{\star}_{\mathrm{SC}} = \int^{T} \frac{M(t) - B(t)}{P(t)} dt \tag{2.23}$$

where $B(t)$ is the grid charging energy. The SS is calculated from (2.22) and (2.23) by replacing PV generation with the load demand in the denominators.

2.4 Building Electrical Loss Modelling

Losses in an electrical system occur in the cable power transfer (conduction) and through conversions between voltage levels and different states, that is, inversion (DC/AC) or rectification (AC/DC).

Cable Conduction

For a power demand p_{load}, the cable conduction losses ($p^{\mathrm{loss}}_{\mathrm{cond}}$) can be expressed using the following relation:

$$p^{\mathrm{loss}}_{\mathrm{cond}}(t) = i_{\mathrm{load}}(t)^2 \mathrm{R_c} = \left(\frac{p_{\mathrm{load}}(t)}{u_{\mathrm{load}}(t)} \right)^2 \mathrm{R_c} \tag{2.24}$$

where i_{load} is the load current and R_c the cable resistance as

$$\mathrm{R}_c = \rho \frac{L}{A} \tag{2.25}$$

where ρ is the resistivity of the cable material, L is the length of the cable, and A is the cable cross-section area [47]. The thermal limitations set the latter, and in [106] determined as a function of maximum current as,

$$A = \max_{t \in \mathrm{T}} \left(i_{\mathrm{load}}(t) \right). \tag{2.26}$$

Voltage Conversion

Few loads operate directly on the incoming 230/110 AC voltage, and conversion between voltage levels, and AC/DC is performed in different ways. For smaller loads, a so-called power factor correction (PFC) circuit is typically used that consists of a diode bridge rectifier followed by a boost converter step. The large-load AC/DC rectifiers can either be a PFC circuit or a three-phase transistor rectifier. The conversion efficiency is calculated using the ratio of input and output powers as

$$\eta_{\text{conv}}(t) = \frac{p_{\text{out}}(t)}{p_{\text{in}}(t)} \tag{2.27}$$

where the inputs and outputs can be either AC or DC at different voltage levels. The corresponding conversion losses are calculated as

$$p_{\text{conv}}(t) = (1 - \eta_{\text{conv}}(t))\, p_{\text{load}}(t) \tag{2.28}$$

where $p_{\text{load}}(\mathrm{t})$ is the converter power throughput, including load demand and converter losses.

2.5 PV System Performance Indexes

There are several indexes to assess the field performance of a PV system. Two examples are the total and specific energy yields, where the former is the aggregated energy output, and the latter is defined as the energy output over the installed rated power as [107]

$$\mathrm{E}_s = \frac{\int^T p(t)\mathrm{d}t}{\mathrm{P}_r} \tag{2.29}$$

where $p(t)$ is the measured power output and P_r the rated array power. The total and specific yields are applicable for comparing and evaluating systems at the exact location, experiencing the same external conditions [108]. Another index is the Performance Ratio (PR)—identified as a key parameter for PV system evaluation [109]—and better captures the external conditions, e.g., irradiance, and enables a comparison of systems regardless of location. The PR also quantifies the system's total losses [110]. In its simplest form, the PR is defined from the measured to expected energy output ratio, where the latter is based on the system nameplate rating. In [111], PR is defined as

$$\mathrm{PR}_i(t) = \frac{y_f(t)}{y_r(t)} \tag{2.30}$$

where $y_f(t)$ and $y_r(t)$ are defined as

$$y_f(t) = \frac{e^i_{\text{out}}}{\mathrm{P}^i_r} \tag{2.31}$$

$$y_r(t) = \frac{H(t)}{\mathrm{G}_{\text{ref}}} \tag{2.32}$$

where e^i_{out} is the measured energy output, P^i_r the array's rated power, $H(t)$ the measured solar irradiance in the module's plane, and G_{ref} the reference irradiance. In [112], G_{ref} is set to 1000 W/m^2 to represent the irradiance level at STC. Using (2.30) gives the relation between the measured and theoretical output and the index can be evaluated for a defined period. However, (2.30) lack the compensation for elevated temperature operation and its effect on the performance [113]. In [113], a compensation term is introduced to account for the difference between module and STC reference temperature (25°C). This term, $\mathrm{PR}_{\mathrm{STC}}$, is defined in [113] as

$$\mathrm{PR}_{\mathrm{STC}}(t) = \frac{y_f(t)}{y_r(t)} \frac{1}{c^{\mathrm{STC}}_k(t)} \tag{2.33}$$

where the compensation term, c^{STC}_k, is given as

$$c^{\mathrm{STC}}_k(t) = (1 + \delta\,(t_m(t) - 25)) \tag{2.34}$$

with δ as the module's temperature coefficient and t_m the measured module temperature. Another alternative to (2.34) is the weather–corrected PR defined as

$$\mathrm{PR}_{\text{corr}}(t) = \frac{y_f(t)}{y_r(t)} \frac{1}{c^{\text{corr}}_k(t)} \tag{2.35}$$

where c^{corr}_k is given as [114]

$$c^{\text{corr}}_k(t) = (1 + \delta\,(t_m(t) - \mathrm{T}^{\text{avg}}_m)) \tag{2.36}$$

where $\mathrm{T}^{\text{avg}}_m$ is the irradiance–weighted average annual module temperature, calculated as

$$\mathrm{T}^{\text{avg}}_m = \frac{\sum H(t) t_m(t)}{\sum H(t)}. \tag{2.37}$$

Since the module temperature is weighted against the irradiance, night-time values (with zero irradiance) are discarded from the evaluation. The reason for using (2.33) and (2.35) is to reduce the seasonal variations that are otherwise observed when the PR is calculated from (2.30).

To quantify the effect of the elevated temperature on the energy output, the temperature correction terms from (2.34) and (2.36) are used to compensate for the measured power output [115] as

$$p_{\mathrm{STC}}(t) = \int^{T} p(t)\frac{1}{(1+\delta\,(t_m(t)-25))}\mathrm{d}t \tag{2.38}$$

$$p_{\mathrm{corr}}(t) = \int^{T} p(t)\frac{1}{(1+\delta\,(t_m(t)-\mathrm{T}_m^{\mathrm{avg}}))}\mathrm{d}t. \tag{2.39}$$

2.6 Parameter Correlation

Different correlation indexes—analytical [116], [117] or numerical [118], [119]—can be used to quantify the match between PV generation and load demand.

The Spearman's rank correlation coefficient (r_s) computes the statistical dependence between the rankings of two variables. Unlike Pearson's correlation—assessing the linear relation—Spearman's correlation assesses the monotonic correlation, defined as

$$\mathrm{r_s} = 1 - \frac{6\sum \mathrm{d}_i^2}{n(n^2-1)} \tag{2.40}$$

where n is the number of observations and d_i^2 the difference between two ranks of each observation, calculated as

$$\mathrm{d}_i^2 = \mathrm{R}(X_i) - \mathrm{R}(Y_i). \tag{2.41}$$

The correlation using (2.40) ranges from perfectly negative (-1) and positive ($+1$) correlations, with 0 meaning no correlation.

CHAPTER 3

Case Setup

This chapter presents the case setup for the buildings used in this work. Papers I, III and V use the case from Section 3.1, Paper IV the simulated data from Section 3.2, and the unpublished work use the case from Section 3.3 for the office assessment of AC vs DC performance. In Section 3.4, the PV and load correlations are examined. Paper II uses the airport load demand described in Section 3.5. Section 3.6 presents the measurement setup and the results from the efficiency characterisation of the DC converters.

3.1 Single-family Residential Building – RISE Research Villa

RISE's Research Villa (Fig. 3.1) is a single-family residential building located in Sweden, with space heating and domestic hot water (DHW) generation using a ground-source heat pump (GSHP). Fourteen PV panels (each of 260 kWp) are installed at a 45° tilt angle due south to help achieve a primary energy consumption of 60 kWh/m^2/a. Blueprints and more detailed information about the building can be found in [47]. The PV and load demand data

Figure 3.1: RISE Research Villa in Borås, Sweden.

is acquired with a 15-minute temporal resolution.

Individual measurements were obtained for the following appliances: GSHP, ventilation, water pumps, and PV generation. As there were no individual measurements of the other appliances, synthetic profiles for lighting and other appliances were created and used with the measured profiles. The works in [120], [121] were used as inspiration for the load profiles of the white goods. A comparison was made with the measured aggregated profile to verify the magnitude and time distribution to verify the synthetic profiles.

In a study on the battery size's effect on self-consumption and self-sufficiency it was concluded that additional SC gains were limited for sizes beyond 7.5 kWh [105]. Thus, this size is used for case-studies of the Research Villa if nothing else is stated.

3.2 Single-family Residential Building – Simulated Data

To examine the effect of geographical location on the DC savings potential, load demand and PV generation data are modelled for two locations: Borås, Sweden and Phoenix, USA, which have two different load and generation (PV) characteristics. The first location has a poor correlation between PV generation and load demand, while the second location has a better correlation. Both cases are for a single-family residential building.

The building energy load demands are obtained from simulations using the IDA Indoor Climate and Energy (IDA ICE) software. The model from [122] is modified to represent a conventional Swedish single-family house with an average U-value of 0.26 $W/m^2/K$. For Borås and Phoenix, the energy demand from household appliances, e.g. TV, cooking, cleaning and DHW usage, is assumed equal. The load for household appliances and DHW production were specified to 30 kWh/m^2 and 25 kWh/m^2 per year, respectively [123]. Thus, the difference in energy demand in space and time comes from the HVAC.

The HVAC usage depends on the system type, operation, and control. In the Swedish case, a GSHP with an electrical backup heater provides space heating and DHW. The GSHP has a rated capacity of 8.4 kW, and the modelling is done to keep the indoor temperature $\geq 21°C$ during the heating season.

For Phoenix, the DHW is generated from a water heater using a resistive element, and space heating is provided by a gas-fired furnace with negligible electricity usage. For cooling and ventilation, a centralised all-air HVAC system is used [124].

The System Advisor Model (SAM) [125] was used to acquire the PV generation profiles using the array size from Section 3.1. The PV orientation was optimised for maximised annual yield by adjusting the tilt angles: 41° for Borås and 28° for Phoenix [126]. Table 3.1 summarises the annual energy demand and PV generation for the simulated residential buildings in Borås and Phoenix.

Table 3.1: Annual energy demand and PV generation (both in AC quantities) from the simulated residential buildings in Borås, Sweden and Phoenix, USA.

	Borås, Sweden	**Phoenix, USA**
Load demand [kWh/a]	10744	11946
PV generation [kWh/a]	3583	7077

Table 3.2: Office building specifications.

Heating/cooling system	GSHP and district heating
Area	11171 m^2
PV array peak power	69.8 kWp

3.3 Office Building – Simulated Data

An office building is modelled using the IDA ICE software. Table 3.2 shows the buildings specifications. The office has a 69.8 kWp roof-mounted PV array with panels mounted at 15° tilt angle due south-southwest (200° azimuth angle). Figure 3.2 shows the office building and the placements of the PV modules. The heating and cooling system operates to maintain 21°C indoor temperature. The heat pump uses the latent capacity from the boreholes for cooling. The occupancy, and thus, the demand from user appliances and the latent heat dissipation (from the metabolism), is modelled from a pre-defined attendance schedule.

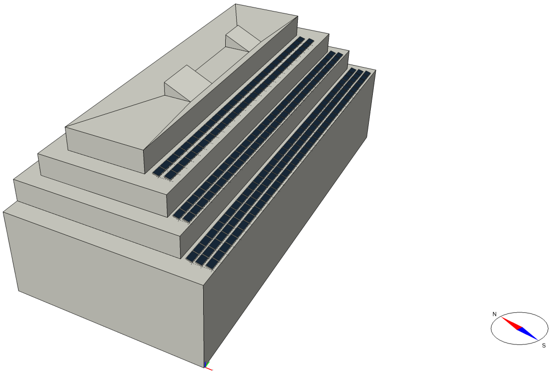

Figure 3.2: Office building and the placements of the PV modules.

The office is modelled at three locations and selected based on the Köppen-Geiger climate classification [127]; see Table 3.3. Typical Meteorological Years (TMY) weather data for the locations are retrieved from [128]. The annual load demands and PV yields are shown in Table 3.4. The PV-to-load share

Table 3.3: Köppen-Geiger climate classification for the simulated office buildings.

Location	**Köppen-Geiger climate class** [127]
Gothenburg, Sweden	*Cfb*: Oceanic climate
Denver, USA	*BSk*: Cold semi-arid
Phoenix, USA	*BWh*: Hot desert

Table 3.4: Office building annual electrical load demands, PV yield and PV-to-load share (r_{PV}) for the three locations.

Parameter	**Gothenburg**	**Denver**	**Phoenix**
Load demand [MWh]	307	301	326
Peak load [kW]	130	123	148
PV yield [MWh]	50	91	104
PV-to-load share, r_{PV} [%]	16	30	32

(r_{PV}) is defined as the PV yield (E_{PV}) to load demand ($\mathrm{E}_{\mathrm{load}}$) ratio as,

$$r_{\mathrm{PV}} = \frac{\mathrm{E}_{\mathrm{PV}}}{\mathrm{E}_{\mathrm{load}}}. \tag{3.1}$$

For the same PV size, the PV yields differ between the sites (+108% between Gothenburg and Phoenix), primarily because of the difference in annual solar irradiance, but also because of the more favourable PV tilt[1] in Phoenix [126].

3.4 PV and Load Correlation

Figure 3.3 shows the normalised weekly mean powers for the load demand and PV generation for the residential and office buildings outlined in Sections 3.1–3.3. The Swedish cases (Figs. 3.3a–3.3c) show a clear seasonal miss-correlation between PV and load demand. The seasonal effect on load demand is due to the dependence on electrical heating, while the PV's dependency comes from the geographical location and difference in irradiance. In contrast, the US cases (Figs. 3.3d–3.3f) show less seasonal variations in load demand and PV generation. The correlations are quantified with Spearman's rank correla-

---

[1] The PV tilt is set by the roof inclination and thus equal for all locations.

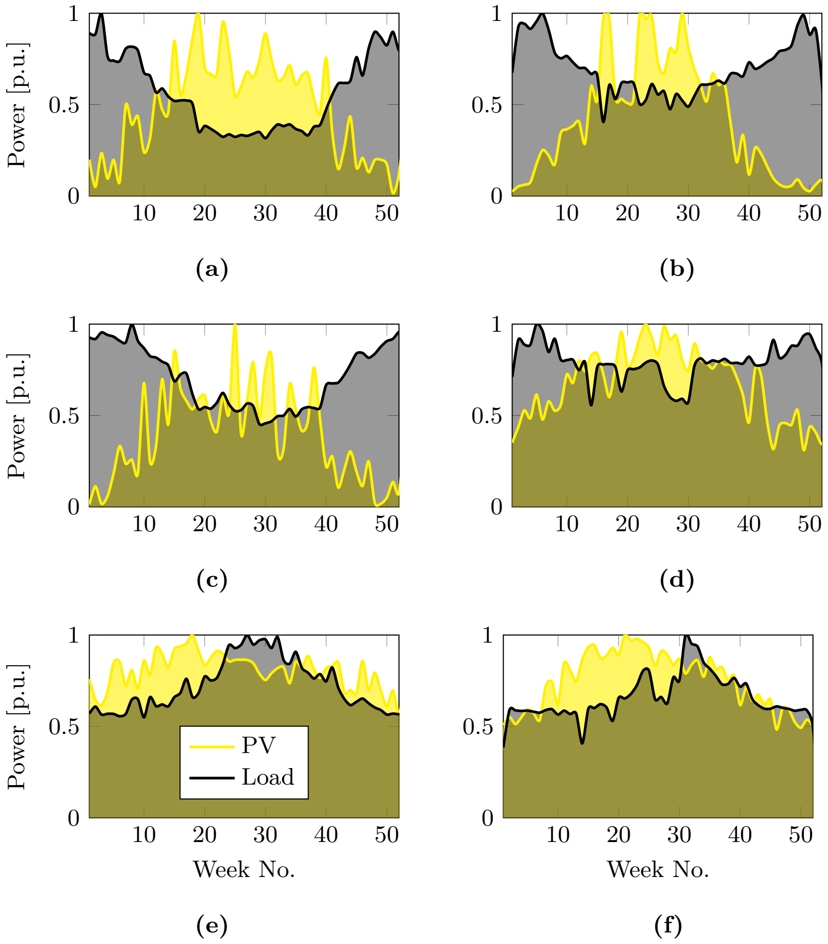

(a) **(b)** **(c)** **(d)** **(e)** **(f)**

Figure 3.3: Normalised weekly mean PV generation and load demand for: **(a)** RISE Research Villa, **(b)** office building in Gothenburg, Sweden, **(c)** single-family residential building in Borås, Sweden, **(d)** office building in Denver, US, **(e)** single-family building in Phoenix, US, and **(f)** office in Phoenix, US.

Table 3.5: Spearman's rank correlation between load demand and PV generation for the residential and office buildings.

Case	r_s [−]
RISE Research Villa, Borås	−0.36
Single-family building, Borås (simulated)	−0.44[a]
Single-family building, Phoenix (simulated)	0.04[a]
Office building, Gothenburg	0.36
Office building, Denver	0.56
Office building, Phoenix	0.71

[a] In [Paper IV], Pearson's correlation coefficient ($\rho = -0.31$ and $\rho = -0.18$ for Borås and Phoenix, respectively) was used but Spearman better assess monotonic correlations, and thus used in this work.

tion (r_s) using (2.40) and shown in Table 3.5 for each case. The negative correlations for the measured and simulated profiles in Borås come from the general seasonal miss-correlation in demand (see Figs. 3.3a and 3.3c) and the demand from the user appliances. The latter peaks outside office hours and, thus, poorly correlates to the available PV generation. The correlation for the residential building in Phoenix improves from the Borås cases because of the cooling demand ($r_s = 0.36$ for only cooling). In contrast, the load and PV correlations for the office buildings are better than the residential cases. The improved correlations are due to the coincidence of working hours and available PV from the south-facing arrays.

3.5 Visby Airport

Located in Gotland (Sweden), the only competing transportation to mainland Sweden and neighbouring countries is via ferry. In 2019, before the Covid pandemic, the airport had more than 8000 arriving passengers.

The hourly load demand from 2018 is acquired from measured data and denoted as 'Business As Usual' (BAU) for this work, and Fig. 3.4 shows the recorded daily mean power. A seasonal variation in load demand and potential PV generation is evident. An apparent seasonal variation is present as the electricity demand is dominated by (electric) heating. The seasonal load demand and PV availability have a negative correlation, meaning that PV's

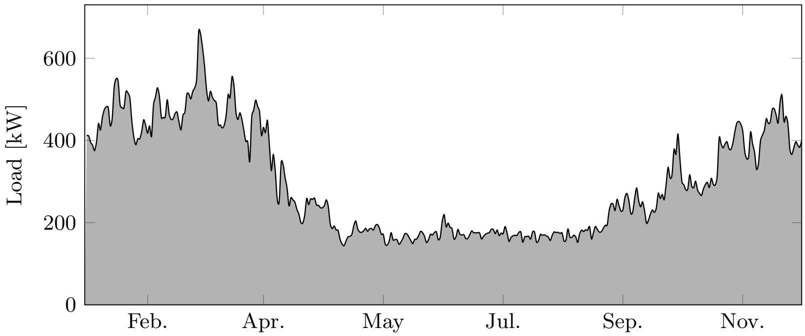

Figure 3.4: Recorded daily mean power from the airports 'Busniess As Usual' operation in 2018.

ability to aid the increased energy and power demands varies throughout the year.

3.6 Converter Characterisation

Accurate converter loss modelling requires performance characterisation over the entire (power) operating range. The converter performance found in the literature, e.g., [42], [45], [129]–[132], varies considerably. Due to this discrepancy, laboratory measurements were made on three PECs to model the efficiency characteristics accurately. These included:

i) 14 kVA transformerless bidirectional grid-tied converter (GC) with a neutral-point-clamped topology,

ii) 6 kW transformerless bidirectional (DC/DC) buck-boost converter with two interleaved legs, and

iii) 6 kW transformerless unidirectional boost (DC/DC) converter with two interleaved legs.

The bidirectional converter is located between the AC grid and the DC main link voltage; the bidirectional DC/DC converter at the battery; and the unidirectional DC/DC converter at the PV array[2]. Table C.1 shows the technical specifications of the measured converters.

---

[2] See Fig.4.2 for a layout of the DC distribution topology.

Figure 3.5a depicts the layout for the efficiency measurements, with the symbols 'A', 'W', and 'V' show measurement points for current, power and voltage, respectively. A Norma D6100A power analyser was used for the battery, PV converter, and the GC's AC side, while the DC side of the GC was measured with a Yokogawa WT1600. Figure 3.5b shows the measurement setup with the solar emulator, power analyser, battery module, battery management system (BMS), and converter.

Figure C.1 shows the measurement points (markers) and curve-fitted efficiency characteristics. The curve fit is done to the polynomial as

$$\eta_{\text{conv}}^{\text{fit}}(s) = \frac{k_1 s^2 + k_2 s + k_3}{s^2 + m_1 s + m_2} \tag{3.2}$$

where s is the converter loading, as a percentage of rated power, the curve-fit constants (k and m) are presented in Table C.2. The bidirectional DC/DC converter was measured for charge and discharge. The difference in performance between charge and discharge comes from the converter topology, with discharge using a buck combination of semiconductors and charge through a boost combination of the semiconductors. The results show that the assumption of fixed efficiency might be sufficient under loading >20% but greatly overestimates the performance for points below that.

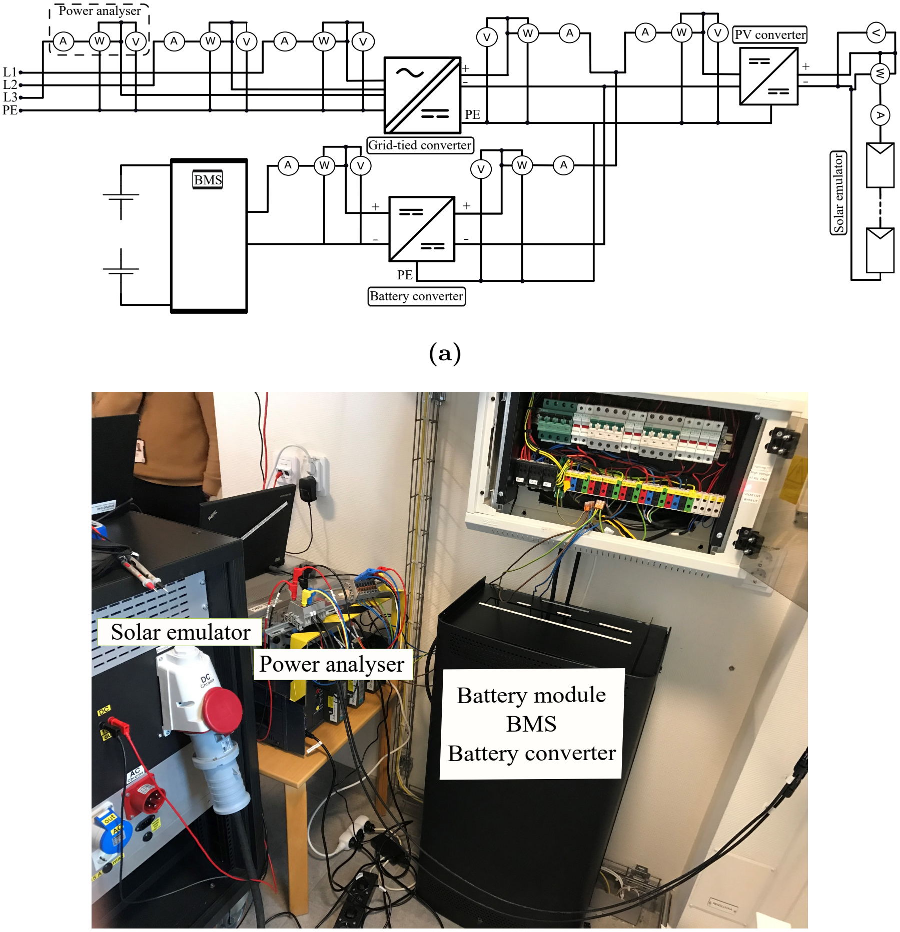

(a)

(b)

Figure 3.5: Measurement setup for the efficiency characterisation of the DC converters. Principle measurement scheme (a) and actual installation (b) with the solar emulator, power analyser, battery module, battery management system (BMS) and converter.

CHAPTER 4

AC vs DC Building Distribution: Effect from PV and Battery, and Supply–Demand Correlation

This chapter is based on Papers III–V and the unpublished material for the office buildings, evaluating the techno-economic performance of AC and DC building distribution. Papers III–V assess the performance of a single-family residential building (cases from Sections 3.1 and 3.2) and the unpublished material uses the office case outlined in Section 3.3. The analysis includes electrical loss modelling—considering the power electronic converter and cable conduction losses—and an economic assessment of the LCC. Two methods are also proposed (from Paper V) to enhance the DC distribution performance by eliminating the grid-tied converter's (GC's) partial-load operation.

4.1 Methodology

In urban areas with access to the electrical grid, AC power is the primary source of electricity in buildings. Figure 4.1 illustrates a typical AC configuration for a residential building with PV and battery storage connected through the main AC link (AC-coupled). The loads are divided into 'big' and

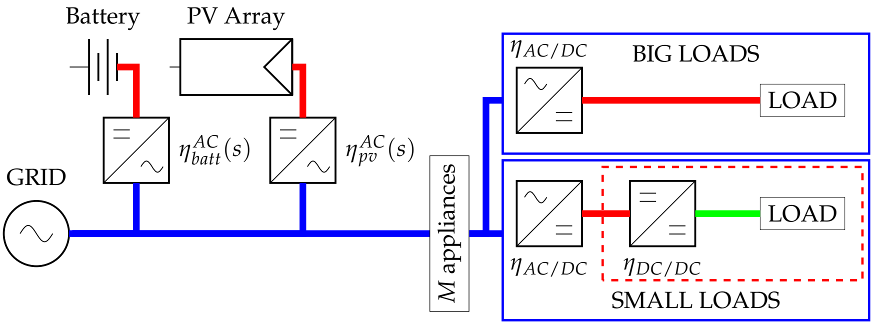

Figure 4.1: Modelled AC distribution topology with AC-coupled PV and battery system.

'small' based on their rated powers, and it is assumed that these are met using DC power in the final stage. The small loads require two conversion steps [49]: rectification (AC/DC) and then DC/DC conversion, where the galvanic isolation is realised in the second stage. A power flow path from PV energy, p_{pv}, to the load (p_{load}) through intermediate battery storing reveals that several conversion steps are needed,

$$p_{\text{load}}(t) = p_{\text{pv}}(t)\eta^{\text{AC}}_{\text{pv}}(s)\eta^{\text{AC}}_{\text{batt}}(s)^2\eta_{\text{AC/DC}}\eta_{\text{DC/DC}} \tag{4.1}$$

where the PV and battery AC/DC efficiencies, $\eta^{\text{AC}}_{\text{pv}}$(s) and $\eta^{\text{AC}}_{\text{batt}}$(s), respectively, are functions of loading (s); and $\eta_{\text{AC/DC}}$ and $\eta_{\text{DC/DC}}$ are load-specific conversions.

Figure 4.2 shows an example of a DC topology for a residential building with separate DC voltage levels for 'big' and 'small' loads. The larger loads operate directly via the main DC bus, and the smaller via a DC/DC converter. The proposed DC topology is commonly found in related studies [133] and effectively integrates the PV array, energy storage, and loads at a common side [134]. Unlike the AC topology, the DC topology includes a three-phase bi-directional GC that links the AC grid and the main DC bus. The main DC link voltage is set to 380 VDC per previous conclusions on suitable DC levels [133], and all big loads operate directly on this voltage level.

The DC topology allows more efficient use of the PV energy because of the reduced conversion losses. Using the power flow example from (4.1), the

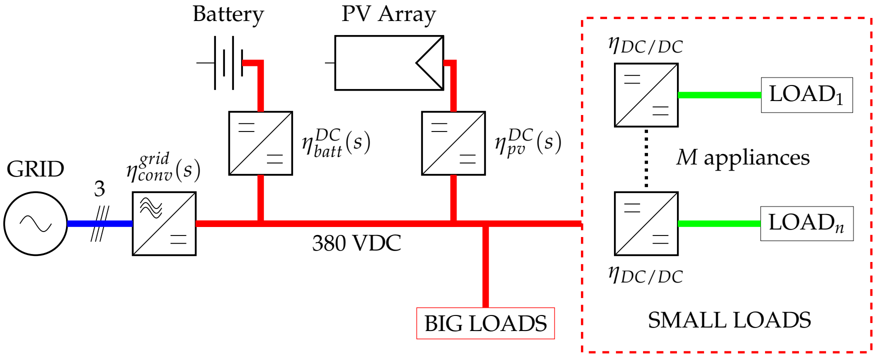

Figure 4.2: Modelled DC distribution topology with individual converters for the PV and battery system. Loads are distinguished as 'BIG' and 'SMALL' depending on their rated powers, where the m smaller loads are supplied by 20 VDC via galvanic isolated DC/DC converters.

equivalent conversion steps could be reduced from five to four as

$$p_{\text{load}}(t) = p_{\text{pv}}(t)\eta_{\text{pv}}^{\text{DC}}(s)\eta_{\text{batt}}^{\text{DC}}(s)^2\eta_{\text{DC/DC}} \tag{4.2}$$

where the low-power DC/DC conversion ($\eta_{\text{DC/DC}}$) is equal for both the AC and DC topologies, as indicated by the dashed perimeters in Figs 4.1 and 4.2.

Investigated System Topologies

In this work, four system topologies are presented, modelled and compared:

- **AC**—230 VAC with load-dependent efficiency.

  Conventional system. See Fig. 4.1 for the system layout including PV and battery system. Here, cable conduction losses occurred with the 230 VAC distribution.

- **DC$_1$**—380 VDC with load-dependent efficiency.

  Conduction losses with 380 VDC distribution. This voltage level was chosen from the EMerge Alliance 380 VDC standard for data centre power distribution [135]–[137] and the result of an expert assessment [12] of suitable DC distribution levels.

- **DC**$_2$—380 VDC with constant converter efficiency.

  To quantify the loss discrepancy with DC$_1$, constant efficiency values were used for all converters and the battery system. This represented the approach used in previous works, e.g., [44], [49], [138].

- **DC**$_3$—380 and 20 VDC with load-dependent efficiency.

  A 20 VDC sub-voltage level is added to DC$_1$ and DC$_2$ to supply the smaller loads and lighting through a central DC/DC converter[1]. Since this ”Class A” voltage level is considered not to be dangerous for humans, safety designs are substantially cheaper [140]. Additionally, this sub-voltage level aligns with the supply voltage of the USB Type-C standard.

Table 4.1 outlines which topologies are included in Papers III–V and the unpublished material from the office building.

Table 4.1: Modelled topologies per Papers III–V and the unpublished material (Unpub.) for the office building.

	AC	**DC**$_1$	**DC**$_2$	**DC**$_3$
Paper III	✓	✓	✓	✓
Paper IV	✓	✓	✓	
Paper V	✓	✓		
Unpub.	✓	✓		

Building Loss Modelling

Cable Conduction Losses

The cable conduction losses are evaluated in [Paper III] for the case outlined in Section 3.1. In the modelling, the feeder lengths from the house's drawings[2], were used together with the distribution voltage, U_{dist}, and (2.24)–(2.25). The cable cross-section area from Table 4.2 was fixed for each appliance and set according to the maximum current of one year's operation in each cable branch. For the lighting, it was assumed that the current to each room, being the sum of the current to all active lamps, was fed through one cable

---

[1] See Fig. 1 in [139] for an example of such a system topology

[2] See Appendix A in [47].

Table 4.2: Standardised cable cross-section area, A, per maximum current according to IEC 60228 [106] and the corresponding resistance, R_c, per meter from (2.25), using the resistivity of copper ($\rho = 0.0171\ \Omega\text{mm}^2/\text{m}$).

Current [A]	**Cross-section [mm^2]**	**Resistance, R_c [Ω/m]**
6	0.75	0.023
10	1.5	0.011
16	2.5	0.007
20	4	0.004

and then distributed to individual branches depending on the lighting layout [47]. Each room consists of 2–11 LED lights at 7 W each. The model treats individual room sockets similarly by distributing a common current to the active socket(s) at each time step. In addition, stationary appliances have a fixed feeder length, and conduction losses were calculated using (2.24)–(2.25).

The required cable cross-section area for a building is found in the IEC 60228 standard [106], as shown in Table 4.2, together with the cable resistance per meter length, using (2.25).

Converter Losses

The AC and DC topologies operate with a fixed main link voltage, U_{dist}; 230 VAC and 380 VDC, respectively. Therefore, the battery voltage requires conversion to the desired voltage, with the losses calculated as

$$p_{\text{bc}}^{\text{loss},j}(t) = \left(1 - \eta_{\text{conv}}^{\text{batt},j}(s)\right) p_{\text{batt}}(t) \quad j = \text{AC} \vee \text{DC} \tag{4.3}$$

where $\eta_{\text{conv}}^{\text{batt},j}$ is the load-dependent efficiency and p_{batt} is the battery power. In addition to the losses of the battery converter, the losses of the battery cells are calculated using (2.9).

The losses of the PV converter[3] are calculated from the gross yield ($p_{\text{pv}}^{\text{gross}}$) and the AC output as

$$p_{\text{pv}}^{\text{gross}}(t) = \frac{p_{\text{pv}}^{\text{AC}}(t)}{\eta_{\text{pv}}^{\text{AC}}(s)} \tag{4.4}$$

where $\eta_{\text{pv}}^{\text{AC}}$ is the inverter efficiency as a function of loading. From the gross

---

[3] PV inverter for the AC topology.

Table 4.3: PEC efficiency characteristics used for system topology modelling.

Efficiency \ Case	**AC**	**DC$_1$**	**DC$_2$**	**DC$_3$**
$\eta_{\mathrm{conv}}^{\mathrm{grid}}$ [%]	100	$f(s)$	97.6[a]	$f(s)$
$\eta_{\mathrm{conv}}^{\mathrm{batt,j}}$ [%]	$f(s)$[b]	$f(s)$[b]	98.5[a]	$f(s)$
$\eta_{\mathrm{pv}}^{\mathrm{j}}$ [%]	$f(s)$[b]	$f(s)$[b]	98.3[a]	$f(s)$
$\eta_{\mathrm{AC/DC}}$ [%]	97	100	100	100
$\eta_{\mathrm{DC/DC}}$ [%]	87	87	87	87

[a] Peak efficiency from PEC measurements.

[b] Constant efficiencies were used in Paper IV.

yield in (4.4), the losses are calculated as

$$p_{\mathrm{pv}}^{\mathrm{loss},j}(t) = p_{\mathrm{pv}}^{\mathrm{gross}}(t)\left(1 - \eta_{\mathrm{pv}}^{j}(s)\right) \quad j = \mathrm{AC} \vee \mathrm{DC} \tag{4.5}$$

where the efficiency (η_{pv}^{j}) dependent on the modelled topology (AC $\vee$ DC).

In this work, all loads operate with DC in the final stage. The rectification in the AC topology uses the appliances' built-in load-side PEC(s) and the DC topology via the bi-directional GC. The rectification losses for each topology are calculated as

$$p_{\mathrm{rect}}^{\mathrm{loss},j}(t) = \begin{cases} \displaystyle\sum_{m=1}^{M} (1 - \eta_{\mathrm{AC/DC}}) p_{\mathrm{load}}^{m}(t), & \text{for } j = \mathrm{AC} \quad (4.6) \\ \left(1 - \eta_{\mathrm{conv}}^{\mathrm{grid}}(s)\right) p_{\mathrm{g}}(t), & \text{for } j = \mathrm{DC} \quad (4.7) \end{cases}$$

where p_{load}^{m} is the power to load m, $\eta_{\mathrm{conv}}^{\mathrm{grid}}$ the GC efficiency and p_{g} the power to/from the grid. In (4.6), the losses are summarised for all loads M assuming a constant load-side H-bridge rectifier efficiency ($\eta_{\mathrm{AC/DC}}$) of 97% [47].

A summary of the efficiency characteristics for the four cases (AC, DC$_1$–DC$_3$) is given in Table 4.3. Here, $f(s)$ denotes the load-dependant efficiency (see Fig. C.1), and $\eta_{\mathrm{AC/DC}}$ and $\eta_{\mathrm{DC/DC}}$ are the load-side converter efficiencies. Note that the last DC/DC conversion ($\eta_{\mathrm{DC/DC}}$) for the low-power appliances is present in both topologies; see dashed perimeter in Figs. 4.1 and 4.2. The losses of the GC are calculated using load-dependent (DC$_1$) and constant (DC$_2$) efficiency characteristics. The efficiency characteristics of the PV and battery converters in the AC case are extracted from the measurements (see Fig. C.1) with a −1.5-percentage-point efficiency offset caused by an extra-semiconductor crossing [47]. In the AC topology, the AC/DC conversion is performed using an H-bridge (97% [47]) for each load-side converter and an assumed binary operation (ON/OFF). In DC_2, the peak efficiency values from the respective measurements are used for the grid, battery, and PV converters.

Reduced GC Partial-Load Operation

Two measures are proposed to reduce the losses from the GC in the DC topology: (i) battery dual-objective operation (DOO) and (ii) GC modular design.

Battery Dual-Objective Operation for Converter Partial-Load Reduction

The battery DOO combines the SC dispatch (Fig. D.1) with an objective to minimise the GC's partial loading. The latter reduces the low-power import and export operations through the converter using a rule-based charge and discharge control with DoD = 100%. The rule-based control compares the instantaneous net demand with a power threshold value, $\mathrm{P}^{h}_{\mathrm{lim}}$. The $\mathrm{P}^{h}_{\mathrm{lim}}$ is modelled as a share (β) as

$$\mathrm{P}^{h}_{\mathrm{lim}} = \beta \times \mathrm{P}^{\mathrm{grid}}_{\mathrm{conv}} \qquad h \ = \ \{\beta_1, ..., \beta_n\}. \tag{4.8}$$

where $\mathrm{P}^{\mathrm{grid}}_{\mathrm{conv}}$ is calculated as,

$$\mathrm{P}^{\mathrm{grid}}_{\mathrm{conv}} = 400\psi\sqrt{3} \tag{4.9}$$

and set by the ampere rating ($\mathrm{I}_{\mathrm{RMS}}$) of the building's main fuse, ψ.

The battery DOO completes the reference battery operation from Paper III with two additional conditions:

1. Suppose net demand is lower than $\mathrm{P}^{h}_{\mathrm{lim}}$. In that case, a check is made whether the available charge content (or gap[4]) can meet the net demand completely. If true, the battery uses full DoD to charge or discharge to meet the net demand ($\mathbf{P}_1$). If this is false, the battery either charge or discharge the extra amount so that the GC power equals $\mathrm{P}^{h}_{\mathrm{lim}}$ ($\mathbf{P}_2$).

---

[4] Battery charge gap is defined as available storage capacity to 100% SOC.

2. If the available charge content (or gap) can fully meet the net demand, it charges or discharges so that the power through the converter is zero; no grid interaction (**P**$_3$). If this is false, the battery is not engaged for partial load coverage and passes all net demand through the GC.

Figure 4.3 displays P$_1$–P$_3$ operations for $\beta = 5\%$, eliminating GC partial-load operation (grey area).

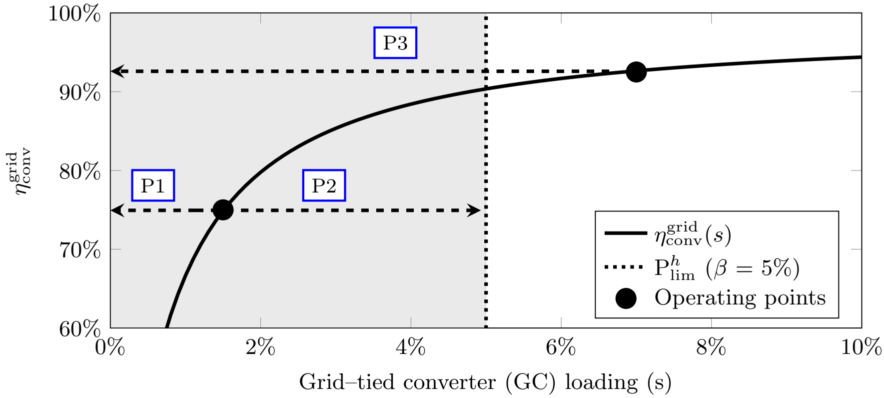

Figure 4.3: Operating principle of battery DOO with $\beta = 5\%$ and demonstration of P$_1$–P$_3$ operations to eliminate grid-tied converter (GC) partial-load (grey area).

Modular Converter Design

A modular GC design is proposed to reduce partial-load operation and thus enhance conversion efficiency. Two converters operate in a Master-Slave configuration [141] at the tertiary control level [142]. Since this design only targets the converters' load distribution, the battery dispatch remains the same as the reference operation. Figure 4.4 depicts the proposed load distribution (PLS), with $\mathrm{P}_{\mathrm{conv}}^{\mathrm{aux.},k}$ and $\mathrm{P}_{\mathrm{conv}}^{\mathrm{main},k}$ as the rated powers of the auxiliary and main converter, respectively, calculated as

$$\mathrm{P}_{\mathrm{conv}}^{\mathrm{aux.},k} = \chi^{k}\mathrm{P}_{\mathrm{conv}}^{\mathrm{grid}} \tag{4.10}$$

$$\mathrm{P}_{\mathrm{conv}}^{\mathrm{main},k} = \left(1-\chi^{k}\right)\mathrm{P}_{\mathrm{conv}}^{\mathrm{grid}}. \tag{4.11}$$

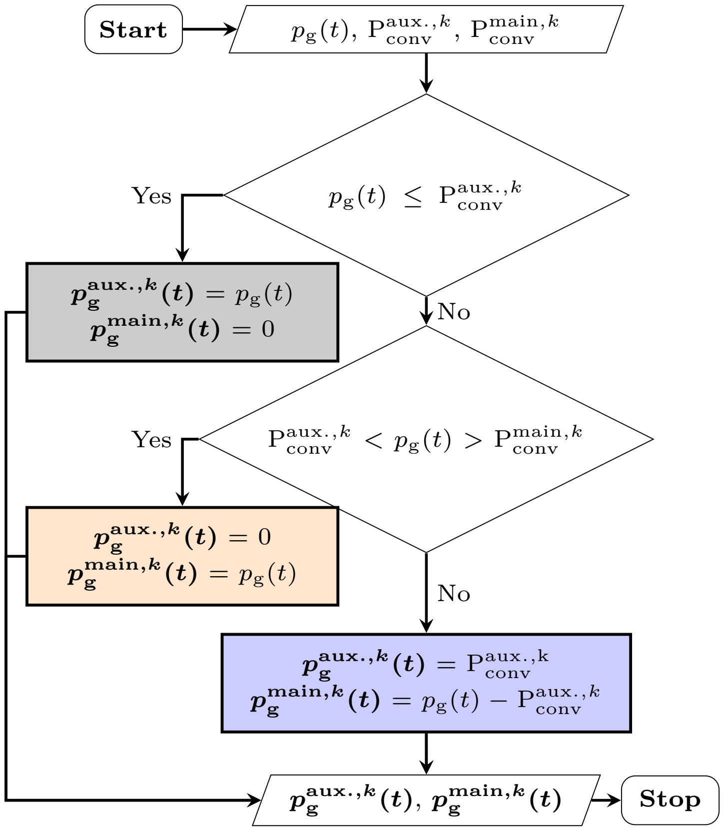

Figure 4.4: Load distribution flow chart for GC modular design.

where χ^k is the modelled modular design and with P_{conv}^{grid} from (4.9). In Fig. 4.4, p_g is the GC power, with $p_g^{aux.,k}$ and $p_g^{main,k}$ for the auxiliary and main converters, respectively.

The PLS performance is compared to an optimised load distribution using a Genetic Algorithm (GA) loss minimisation. The GA's objective function

(4.12a) and constraints are expressed as

$$\min_{t \in T} \quad \sum^{T} p^{\mathrm{loss}}_{\mathrm{aux.}}(t) + p^{\mathrm{loss}}_{\mathrm{main}}(t) \tag{4.12a}$$

$$\text{s.t.} \quad p^{\mathrm{aux.}}_{\mathrm{g}}(t) + p^{\mathrm{main}}_{\mathrm{g}}(t) \equiv p_{\mathrm{g}}(t), \tag{4.12b}$$

$$0 \leq p^{\mathrm{aux.}}_{\mathrm{g}}(t) \leq \mathrm{P}^{\mathrm{aux.}}_{\mathrm{conv}}, \tag{4.12c}$$

$$0 \leq p^{\mathrm{main}}_{\mathrm{g}}(t) \leq \mathrm{P}^{\mathrm{main}}_{\mathrm{conv}} \tag{4.12d}$$

where (4.12b) ensures load-sharing and (4.12c) and (4.12d) the PECs' power constraints. Figure 4.5 shows the efficiency characteristics for grid import using the PLS and GA (both for $\chi = 15\%$) and the reference case with a single-converter operation. The PLS offer significant efficiency improvements at partial loading compared to the reference operation and performs similarly to the GA.

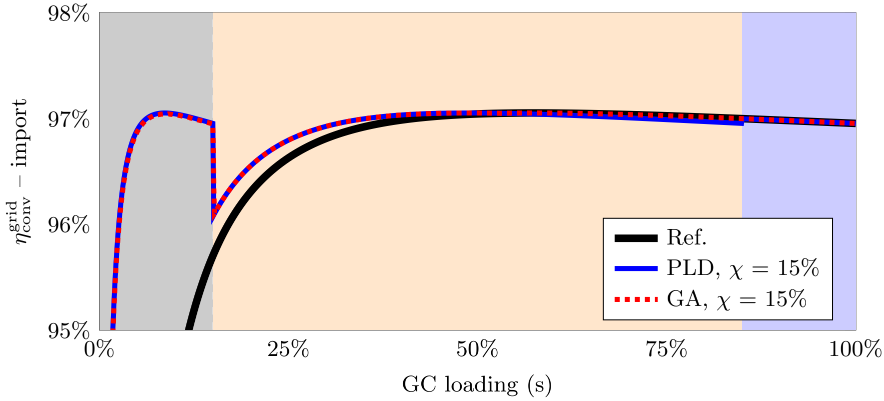

Figure 4.5: Efficiency characteristics for grid import with the PLS and GA (both for $\chi = 15\%$), and single converter operation (Ref.). The colour-coding follows the execution from Fig. 4.4.

To examine the effect of the combined operation of the battery DOO and modular converter design, the DOO is applied to the sole operation of the auxiliary converter (the grey area in Fig. 4.5), and the β condition restricts the partial-load operation of the auxiliary converter. The analysis include scenarios, $\mathbb{S}$, with varying β and χ operations as

$$\mathbb{S} = \begin{bmatrix} \sigma_{\beta 1 \chi 1} & \cdots & \sigma_{\beta 1 \chi n} \\ \vdots & \ddots & \vdots \\ \sigma_{\beta n \chi 1} & \cdots & \sigma_{\beta n \chi n} \end{bmatrix} \tag{4.13}$$

$$\forall \beta = 1, \ldots, 20\% \quad \forall \chi = 2, \ldots, 50\%.$$

Table 4.4 summarises the rated powers of the PECs in Papers III–V and the unpublished work for the office buildings. For all cases, the battery's converter is rated at 80% of the energy capacity ($\mathrm{E_{batt}}$). In Papers III and IV, the rated power of the GC is defined from a pre-modelling calculation of the maximum annual load power (p_{load}) to ensure peak power coverage. Similarly, for the office case analysis, the rated power considers the peak PV export. For the PV converter in Paper IV, the rated power is scaled with $r_{\mathrm{DC/AC}}$ (1.25), thus reducing the peak power output and enhancing the efficiency of the converter by shifting the operating points to higher loading. Related work for a Swedish context [143] showed that the annual PV yield is marginally affected by reducing peak output. For the other cases—Papers III and V, and the office—the PV converter is rated based on the array's peak power.

Table 4.4: Rated powers of the PECs for the studied cases.

$\mathrm{P_{rated}}$	**Paper III**	**Paper IV**	**Paper V**	**Office (unpub.)**
$\mathrm{P_{conv}^{grid}}$	$\max\limits_{t\in T}[p_{\mathrm{load}}(\mathrm{t})]$	$\max\limits_{t\in T}[p_{\mathrm{load}}(\mathrm{t})]$	(4.9)	$\max\limits_{t\in T}[p_{\mathrm{load}}(\mathrm{t});p_{\mathrm{pv}}(\mathrm{t})]$
$\mathrm{P_{batt}}$	$0.8\mathrm{E_{batt}}$	$0.8\mathrm{E_{batt}}$	$0.8\mathrm{E_{batt}}$	$0.8\mathrm{E_{batt}}$
$\mathrm{P_{pv}}$	$\mathrm{P_{pv}^{rated}}$	$\frac{\mathrm{P_{pv}^{rated}}}{r_{\mathrm{DC/AC}}}$	$\mathrm{P_{pv}^{rated}}$	$\mathrm{P_{pv}^{rated}}$

Techno-Economic System Performance Indexes

In addition to loss savings, the topologies are evaluated for PV utilisation (κ_{pv}), which defines the useful PV energy, considering the losses of the PV converter and battery storage (including battery cell losses). When battery charging is solely done via PV surplus, κ_{pv} is calculated as

$$\kappa_{\mathrm{pv}}^{j} = 1 - \int^{T} \left(\frac{p_{\mathrm{pv}}^{\mathrm{loss},j}(t) + p_{\mathrm{cell}}^{\mathrm{loss}}(t) + p_{\mathrm{bc}}^{\mathrm{loss},j}(t)}{p_{\mathrm{pv}}^{\mathrm{gross}}(t)} \right) \mathrm{d}t \quad j = \mathrm{AC} \vee \mathrm{DC} \tag{4.14}$$

where $p_{\mathrm{bc}}^{\mathrm{loss},j}$ are the losses of the battery converter (4.3), $p_{\mathrm{cell}}^{\mathrm{loss}}$ the battery cell losses (2.9), $p_{\mathrm{pv}}^{\mathrm{loss},j}$ the losses of the PV converter (4.5), and $p_{\mathrm{pv}}^{\mathrm{gross}}$ the gross PV yield from (4.4). The numerator denotes the PV-associated losses. Another metric, defined in [11] as the system efficiency (κ_{system}) relates the losses to the load demand as

$$\kappa_{\mathrm{system}}^{j} = 1 - \frac{\mathrm{E}_{\mathrm{loss}}^{j}}{\mathrm{E}_{\mathrm{load}}} \quad j = \mathrm{AC} \vee \mathrm{DC} \tag{4.15}$$

where $\mathrm{E}_{\mathrm{load}}$ is the load demand, which is equal for all modelled topologies and cases. The aggregated losses ($\mathrm{E}_{\mathrm{loss}}^{j}$) is calculated using (2.9), (2.24), (4.3), and (4.5)–(4.7) as

$$\mathrm{E}_{\mathrm{loss}}^{j} = \int^{\mathrm{T}} \begin{pmatrix} p_{\mathrm{cond}}^{\mathrm{loss},j}(t) + p_{\mathrm{rect}}^{\mathrm{loss},j}(t) + p_{\mathrm{bc}}^{\mathrm{loss},j}(t) + \\ + p_{\mathrm{cell}}^{\mathrm{loss}}(t) + p_{\mathrm{pv}}^{\mathrm{loss},j}(t) \end{pmatrix} \mathrm{d}t \quad j = \mathrm{AC} \vee \mathrm{DC}. \tag{4.16}$$

The economic performance is assessed for the LCC using (2.18), the net electricity bill from (2.16), and the monetised battery degradation from (2.20). The annual net operating cost (OC) is calculated as

$$\mathrm{OC} = \sum^{T} \mathbb{C}_{\mathrm{net}}(t) + \mathbb{C}_{\mathrm{deg}}. \tag{4.17}$$

Due to the investment cost uncertainties [144], the economic assessment is performed to quantify the added cost to break even. By setting the LCC in (2.18) equal for all scenarios, the difference in LOC gives the cap for the added cost. The comparison assumes that all cases have equal maintenance, replacement costs, and residual values.

4.2 Results and Discussion – AC vs DC Building Distribution

This section shows AC and DC distribution results in single-family and office buildings. The results examine total losses divided per source, the effect of PV and battery storage, geographical location, and the techno-economic effect of the proposed DC operational enhancement methods.

Single-family Residential Building

These results are based on Paper III, using the case-setup of RISE's Research Villa outlined in Section 3.1.

The annual losses of the four topologies (Fig. 4.6) without PV and battery storage results in three observations:

1. The GC losses significantly differ when modelled with constant and load-dependent efficiency characteristics; see cases DC_1 and DC_2. Assuming constant efficiency thus overestimates the GC's performance. The results suggest that loss savings are achieved for the DC topology without PV or battery storage with constant PEC efficiencies. In relative numbers, the losses of the GC—using a constant efficiency—(DC_2) are 34% lower (in absolute terms, an underestimation of 63 kWh) compared to (DC_1). Using (4.15), the system efficiency values for AC and DC_{1-3} are 95.3, 94.3, 95.8, and 93.7%, respectively.
2. A DC sub-voltage level (DC_3) adds 7.3% (29.0 kWh/a) to the total losses at 20 VDC. These losses transfer to the load-side conversion (DC/DC) losses, which are 3% higher for DC_3 than in the other cases. The cable conduction losses amount to 2.4% and 1.5% of the total losses in the AC and DC_1 cases, respectively.
3. Without PV and battery, the DC topology does not present a favourable option for loss reduction (excluding case DC_2 with the reasoning performed in 1).

Based on these observations, if not mentioned otherwise, the continuing analysis only includes the AC case and the DC topology with load-dependent converter efficiency (DC_1).

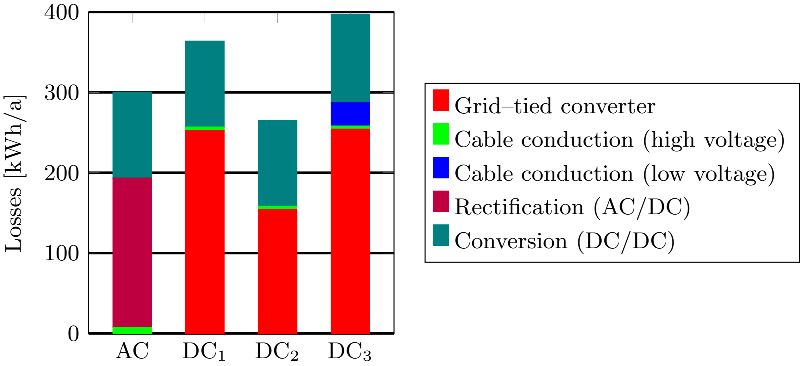

Figure 4.6: Annual system losses in the single-family Research Villa in Borås for the modelled cases without PV and battery storage.

The comparison presented in Table 4.5 is for a system with a 3.7 kWp PV array, a 7.5 kWh battery storage and the dispatch from Fig. D.1. The generated PV energy is higher in the DC case since it is fed directly to the DC link, with reduced conversion losses. Including PV and battery, the DC topology reduces the losses by 15.8%. Figure 4.7 shows a loss breakdown per source for the two cases. The lowered losses through the GC are due to the reduced grid interaction (see comparison with DC_1 in Fig. 4.6) with energy generated (PV) and stored (battery) locally. Comparing the rectification losses for AC operation with the GC in the DC case—having the same purpose[5]—shows a 5.3% relative loss reduction with DC operation. The losses of the PV array and

Table 4.5: System performance with AC and DC_1 for 3.7 kWp PV and 7.5 kWh battery storage.

	AC	**DC_1**	**Difference [%]**
System losses, E_{loss} [kWh]	583	490	−15.8
PV energy [kWh]	3113	3161	1.5
κ_{pv} [%]	91.3	93.7	2.6
κ_{system}[%]	90.8	92.3	1.7

---

[5] In addition to grid import rectification (AC/DC), the GC also inverts the grid export (DC/AC).

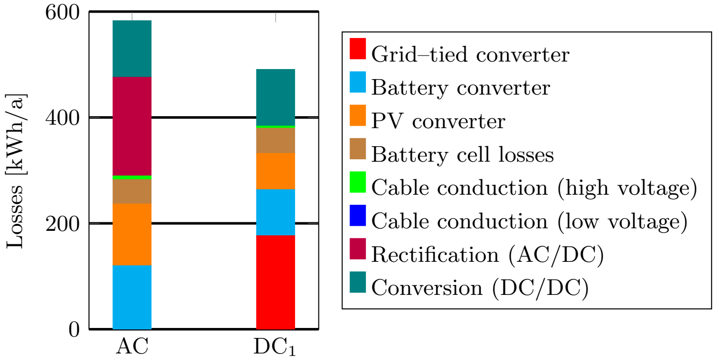

Figure 4.7: System losses with 3.7 kWp PV and 7.5 kWh battery storage. Low-voltage cable conduction was zero for both topologies but is included in the legend for consistency with the other figures.

battery are lower for the DC case due to more efficient conversion (−41.4% and −27.3%, respectively), which affects κ_{pv}; see Table 4.5. For this case, the PV-associated losses of the PV converter, battery converter, and battery cells are 28.6% lower with the DC topology, resulting in a κ_{pv} gain of 2.6%. The κ_{system} are 90.8 and 92.3% for the AC and DC topologies, respectively, thus a relative gain of 1.7%.

To determine under what circumstances DC is a favourable option for loss reductions, Fig. 4.8a shows a heat map of the loss difference in AC and DC operations sorted by daily hour (1–24) and month (1–12), where positive values indicate loss savings with DC operation. At times, with PV generation, DC operation results in lower losses, which correlates well with the results in Fig. 4.8b. In the presence of battery storage and with the battery control using Fig. D.1, the loss savings expand to later in the day when charging from PV surplus (Fig. 4.8c) and discharges to cover the load (see Fig. 4.8d). Using Spearman's rank coefficient from (2.40), the loss savings showed the highest correlation (+0.59) with PV generation.

Figure 4.9 shows an expanded analysis of AC and DC$_1$ by varying the sizes of the PV array and battery storage. Compared with the case without PV and battery (Fig. 4.6), the inclusion of PV ('1 PV') reduces the loss difference from +22% to +6.7%. A doubling of the PV ('2 PV') results in marginal improvements relative to AC (+5.3%/a). Doubling the PV adds +18.3%

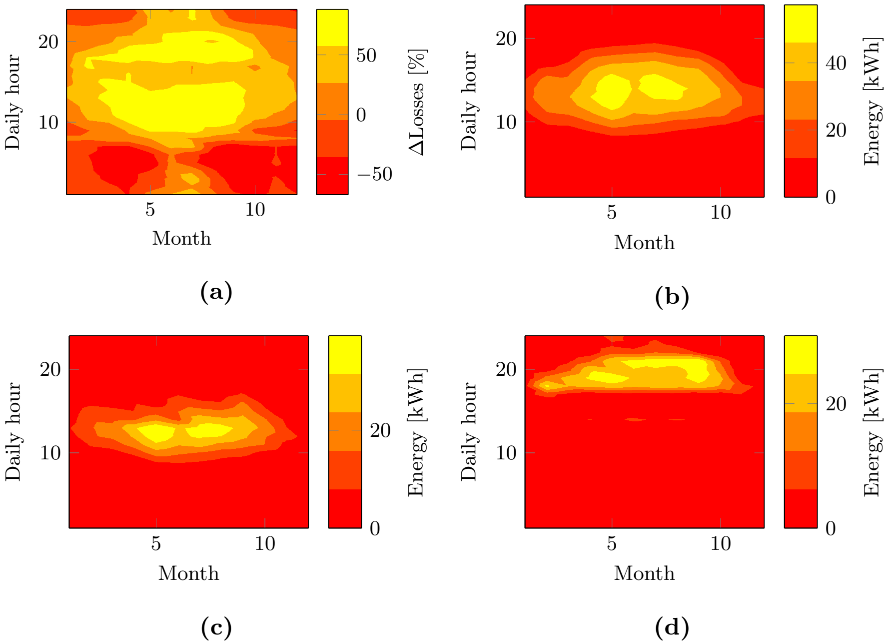

Figure 4.8: Heat map per daily hour and month in 2016 showing: (**a**) loss differences in AC and DC operations (positive values indicate savings with DC), (**b**) accumulated PV generation, and (**c, d**) accumulated battery charge and discharge, respectively.

to the grid-tied converter losses due to increased export. DC first achieves savings with both PV and battery ('1 PV/10 kWh' and '2 PV/7.5 kWh'), as it reduces the interaction with the grid and thus affects the GC.

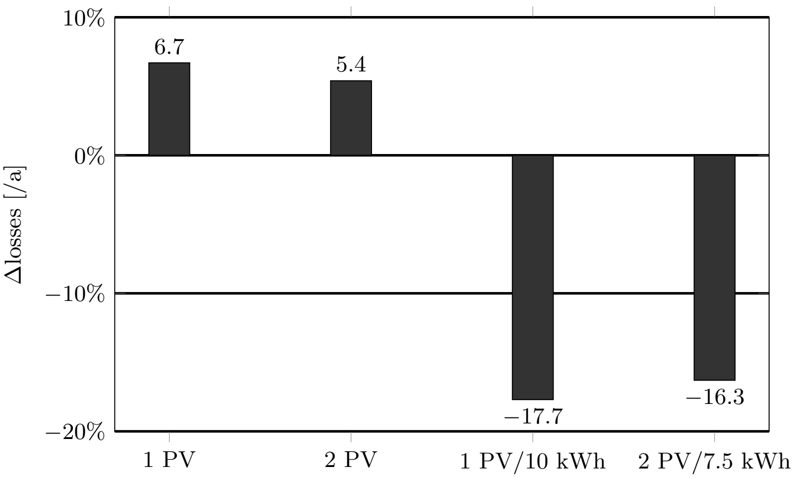

Figure 4.9: Relative changes in losses for DC operation for various PV and battery system configurations. The Δ comparison is relative to the AC performance; thus, positive values indicate higher losses for DC operation.

Effect of Geographical Location

These results are based on Paper IV, using the case-setup of the simulated single-family residential building outlined in Section 3.2.

Figure 4.10a and Fig. 4.10b show a breakdown of the losses from AC and DC operation in Borås for two PV and battery systems; 3.6 kWp/0 kWh and 3.6 kWp/7.5 kWh, respectively. The GC is the main loss contributor for the DC cases, and including battery storage reduces these losses. Comparing the two DC cases with varying (DC_1) and constant (DC_2) GC efficiency, the latter underestimates the losses by 14.7% and 19.0% with and without the battery, respectively. Compared to AC, the κ_{system} gains are 1.2% and 2.7% for DC_1 and 2.3% and 3.6% for DC_2 with and without a battery, respectively. As aforementioned, using a constant efficiency (DC_2) is a questionable approach and, again, proven to underestimate the GC's losses. Table B.1 shows a numerical comparison of the results for Borås. The PV and battery losses are significantly lower for DC operation and directly reflected in κ_{pv}). Includ-

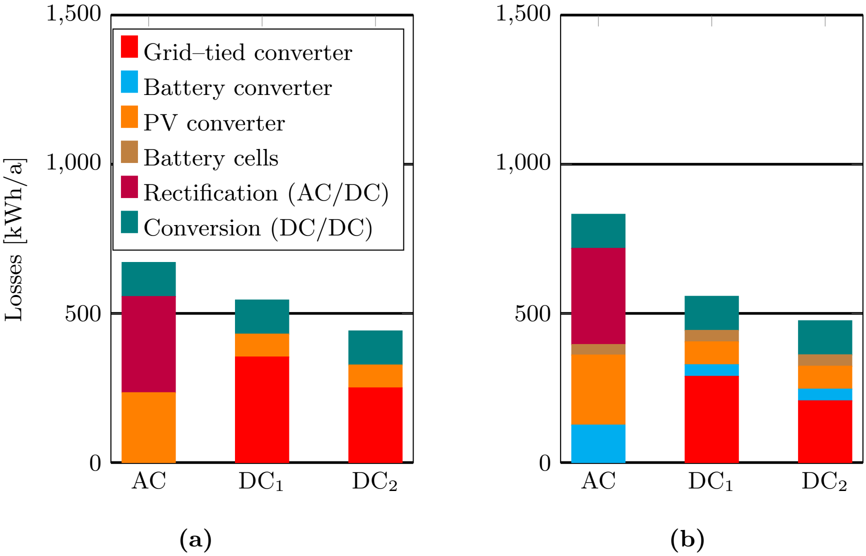

Figure 4.10: Losses for the two PV and battery systems in Borås **(a)** 3.6/0 kWp/kWh and **(b)** 3.6/7.5 kWp/kWh.

ing the battery increases the κ_{pv} gain for DC operation from 4.3% to 6.9%, compared to AC.

The results for Phoenix are shown in Table B.2, and Figs. 4.11a and 4.11b. The DC topology shows better performance for κ_{system} (+2.4–4.9%) and κ_{pv} (+4.0–6.4%), with loss savings of −43.6% and −28.5% with and without battery storage, respectively. For comparison, Fig. 4.11 includes DC_2 and shows an underestimation of the GC losses by up to 29%, stressing the importance of dynamic efficiency modelling to accurately represent the performance.

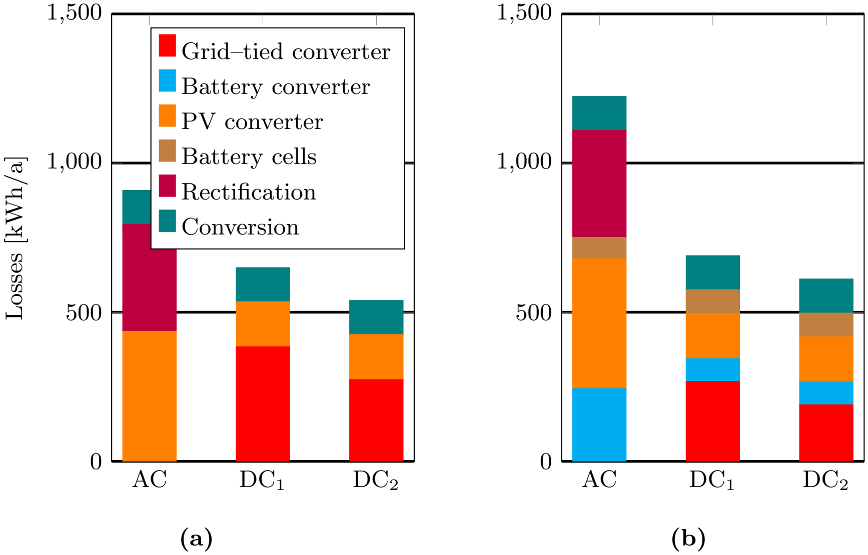

Figure 4.11: Losses for Phoenix, USA, and two PV and battery systems: **(a)** 3.6/0 kWp/kWh and **(b)** 3.6/7.5 kWp/kWh.

A sensitivity analysis is made by varying the PV array and battery sizes; see Fig. 4.12. A comparison of κ_{system}, κ_{pv}, and losses are made for PV sizes 3.7, 5 and 10 kWp, and for battery sizes 0–10 kWh. The relative increase in PV utilisation (**top**) is higher in Borås (4.3–7.4%) than in Phoenix (3.9–6.8%). The gains increase with battery size and are the highest for the smaller PV array (3.7 kWp). The gain in system efficiency (**middle**) is inversely related to the PV size (more significant for larger PV) and higher in Phoenix (2.3–8.8%) than Borås (1.3–5.9%) for the same system configuration. For Phoenix,

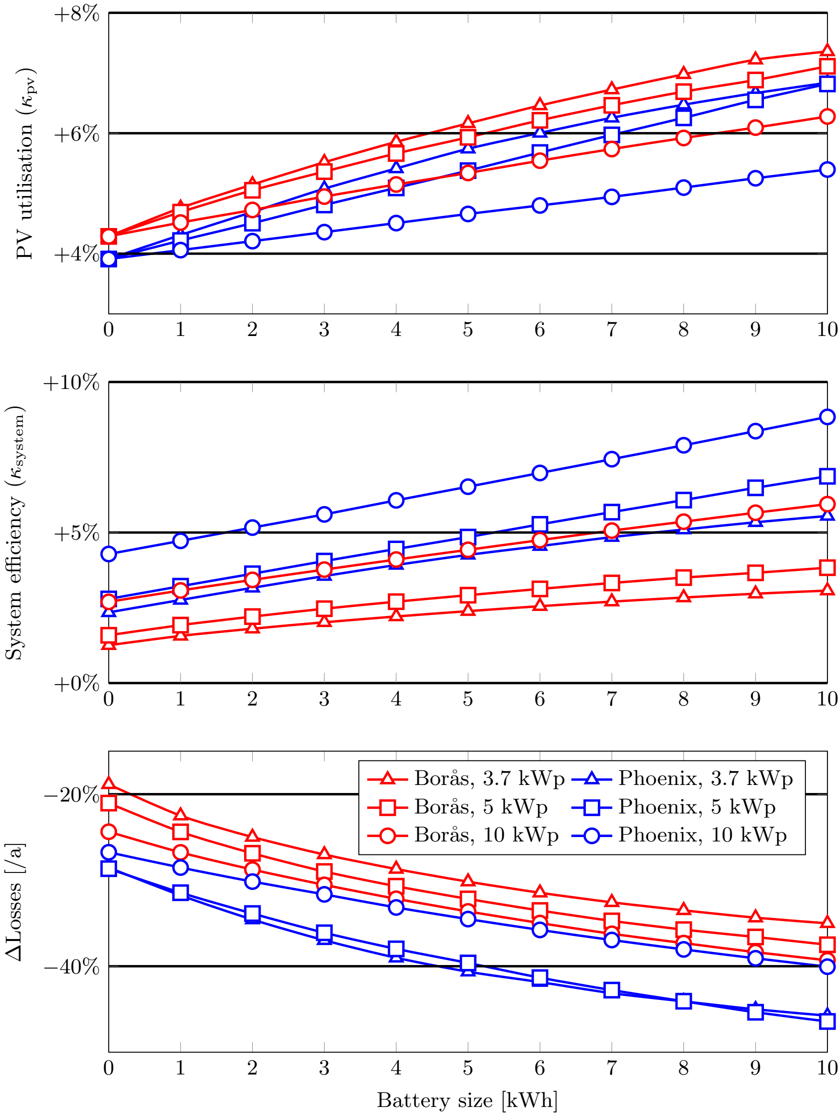

Figure 4.12: Effect on DC performance gains on: PV utilisation (**top**), system efficiency (**middle**), and annual system losses (**bottom**), for varying battery sizes at the two locations.

there is an almost linear increase in performance with battery size, and the incremental increase is less for Borås. The loss savings are more significant in Phoenix (−27% to −46%) than Borås (−19% to −39%) and increases with PV size for Borås, unlike Phoenix where the two smaller sizes generate similar savings and reduced savings for 10 kWp. To explain this, Fig. 4.13 shows the GC losses at the two locations for varying PV sizes and a 10 kWh battery. An increased PV size marginalises the import losses in both cases; see Fig. 4.13a and Fig. 4.13b. However, the effect is more significant on the export losses (Fig. 4.13c and Fig. 4.13d), where a larger PV size generates more export to the grid and thus increase the GC's losses; especially prominent for Phoenix.

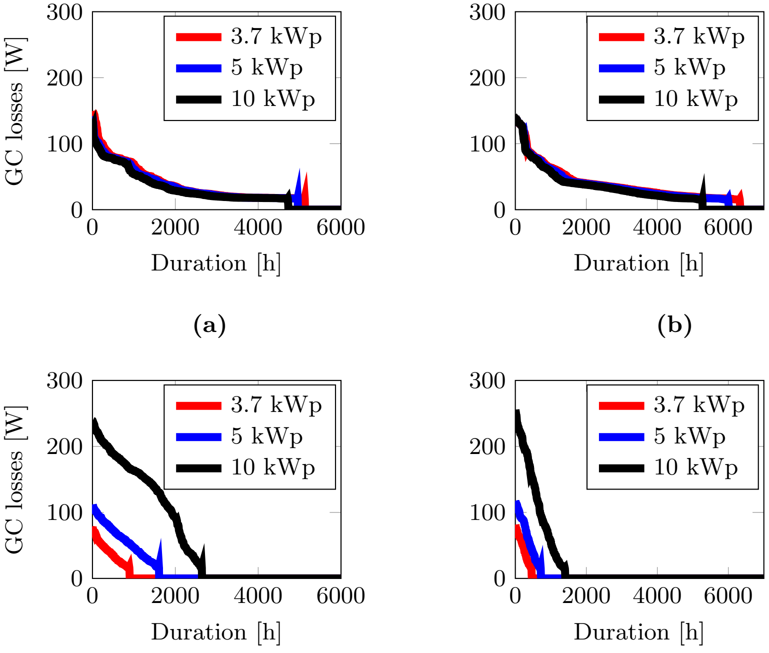

(a)

(b)

(c)

(d)

Figure 4.13: Duration diagram of the bi-directional grid-tied converter losses for: **(a)** Phoenix import, **(b)** Borås import, **(c)** Phoenix export and **(d)** Borås export. All with a 10 kWh battery and varying PV size.

Reduced GC Partial-Load Operation

As concluded in [Papers III and IV], the GC is the primary loss source in DC building distribution. Two methods of operation are suggested to reduce the GC losses by eliminating partial-load operation. These results are based on Paper V, and the use-case of RISE Research Villa outlined in Section 3.1. The enhancement methods (PLS and battery DOO) are firstly compared to a DC reference case, denoted DC* (ψ = 16 A in (4.9)), and the best performing cases are compared to conventional AC distribution for system losses. The methods are also evaluated for their annual battery degradation. An economic assessment quantifies the added investment cost for the DC cases to break even compared to AC.

The annual system losses, per source, are shown in Fig. 4.14a for DC* (Ref.) and battery DOO. For DC*, most losses come from grid import (57%), with marginal (6%) export losses. Noticeably, DOO reduces the GC losses for all β by constraining the grid interaction above $\mathrm{P}^{h}_{\mathrm{lim}}$. Consequently, the battery operation increases substantially for $\beta \geq 5\%$, resulting in net loss savings only for $\beta \leq 5\%$. The net increase in losses for $\beta = 10\%$ and 20% comes from the significant increase in battery throughput (+114% for $\beta = 20\%$ compared to $\beta = 1\%$). Figure 4.14b shows the losses for DC* and modular GC designs. The PLS reduces the GC losses relative to DC* for all designs. Since the battery operation is the same, the difference in battery-associated losses is insignificant. Relative to DC*, annual savings from the PLS are 5–27%, with optimal savings for χ = 15–20%.

As seen in Fig. 4.14, most losses for DC* originate from grid import, with 79% from operation ≤10% of the GC's rated power. Using the loss-distribution from grid import, $\mathrm{P}(e^{\mathrm{imp}}_{\mathrm{loss}})$, and the combined efficiency characteristics, a weighted efficiency is calculated as

$$\eta^{w,\chi}_{\mathrm{imp}} = \sum^{\mathrm{J}} \mathrm{P}\left(e^{\mathrm{imp}}_{\mathrm{loss}}\right)^{j} \overline{\eta^{j,\chi}_{\mathrm{imp}}} \tag{4.18}$$

where $\overline{\eta^{j,\chi}_{\mathrm{imp}}}$ is the average efficiency in the j:th bin for modular ratio, χ. Figure 4.15 shows the weighted grid import efficiency for the PLS and the DC reference (DC*, χ = 0%). The weighted efficiencies confirm that χ = 15–20% gives the most significant loss reductions for grid import (and total losses). It also confirms that these are global optimums.

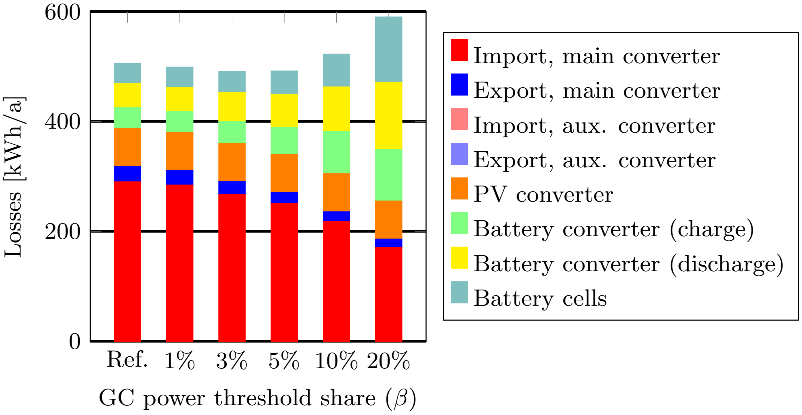

(a)

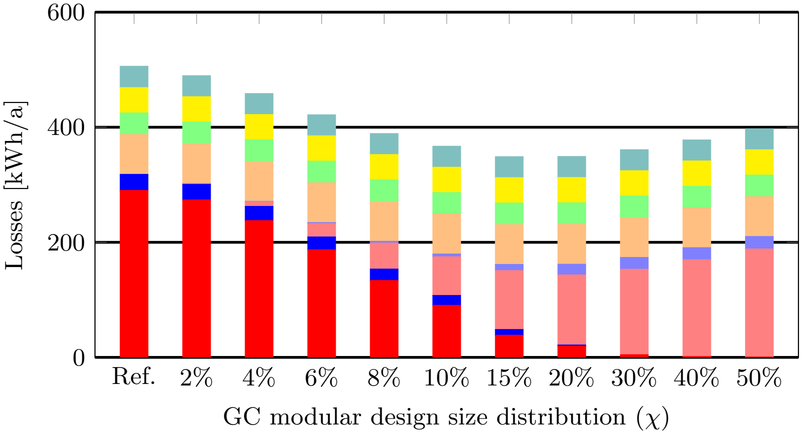

(b)

Figure 4.14: Annual system losses from DC distribution per loss sources compared to DC* (Ref.) for (a) battery DOO, and (b) modular GC design using the PLS.

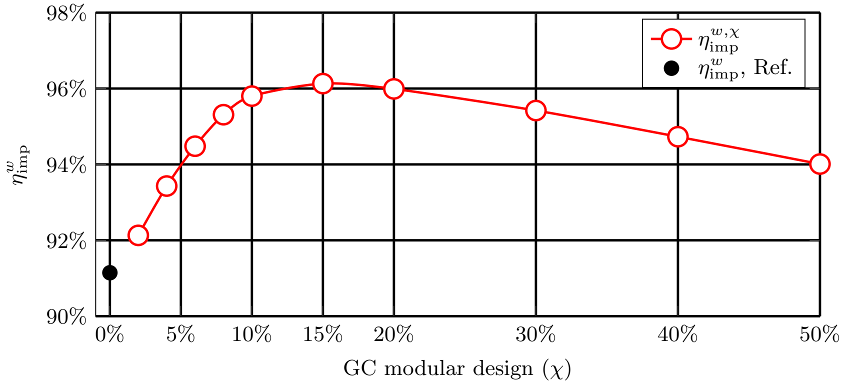

Figure 4.15: Weighted grid import efficiency $\forall\chi$ and the DC reference ($\chi = 0\%$).

Effect on Battery Ageing from Battery DOO

Using (2.14) and (2.15) enables a quantification of the effect on battery degradation from DOO with 100% DoD, compared to the reference battery operation from Fig. D.1. Figure 4.16 shows the modelled battery degradation for DC* and battery DOO. For DC*, the annual battery degradation is 5% of

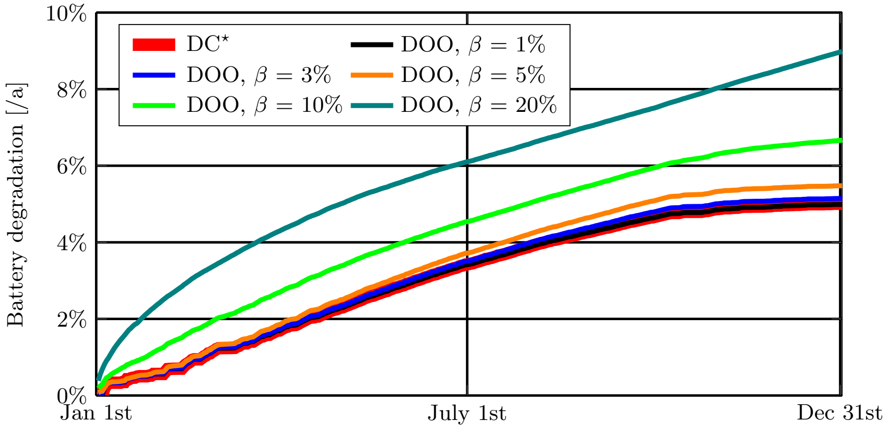

Figure 4.16: Battery degradation for DC* and battery DOO ($\beta = 1$–20%).

the nominal capacity. A marginal difference for DOO with $\beta \in$ 1–5% (<0.5 percentage points) is observed. However, a significant difference occurs for $\beta \in$ 10–20%, with up to four percentage points for $\beta = 20\%$. Since the DOO use DoD = 100%, the battery operates more frequently at the SOC extremities than the reference dispatch in DC*. The most significant difference is observed at SOC<15% where DC* limits discharge to 15% ($\mathrm{SOC_{min}}$), while DOO allows for complete battery depletion. Considering the findings in [145] that both cycling and calendar ageing are less prominent at lower SOC levels, and the empirical degradation in Fig. 4.16, the effect of the DOO on battery ageing is negligible for $\beta \in$ 1–5%.

Combined Modular and Battery DOO

To examine the combined effect from the two DC enhancement methods, Fig. 4.17 shows the variation in loss savings from scenarios, $\mathbb{S}$, in (4.13) relative to modular operation ($\forall\chi$) with $\beta = 0\%$. Despite reducing the losses from the

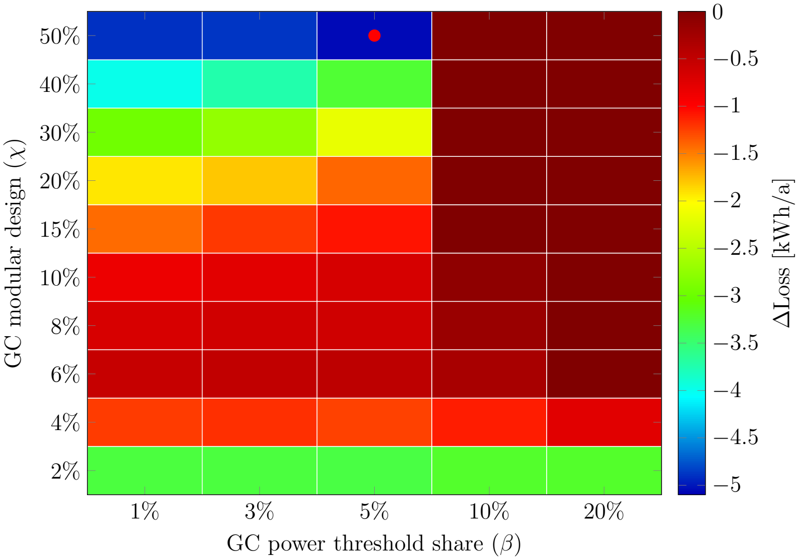

Figure 4.17: Loss savings from scenarios $\mathbb{S}$ relative modular operation ($\beta = 0\%$). Peak relative savings (●) at $\beta = 5\%$ and $\chi = 50\%$. NB! The upper limit of ΔLoss is restrained at 0 for better visualisation.

auxiliary converter, the net savings are marginal. Increased battery-associated losses (converter and cells) supersede the converter loss savings, especially for higher β. At most, an additional -5.1 kWh/a is observed for $\beta = 5\%$ and $\chi = 50\%$ (denoted $\sigma_{\beta 5 \chi 50}$). Compared with the best-performing design in Fig. 4.14b ($\chi = 15\%$); $\sigma_{\beta 5 \chi 50}$ results in a mere -1.6 kWh/a loss saving.

Figure 4.18 shows the battery degradation for scenarios, $\mathbb{S}$, and $\beta = 0\%$ (solid line). For $\mathbb{S}$, the β constraint is defined from the auxiliary converter[6], meaning that the degradation increases with both χ and β, but are less prominent than in Fig. 4.16 where β is defined from the rated GC power; see (4.8). Noteworthy is that $\sigma_{\beta 3 \chi 20}$ not only gives amongst the lowest losses (see Fig. 4.17), but the degradation is also in the lower span of the $\mathbb{S}$ scenarios.

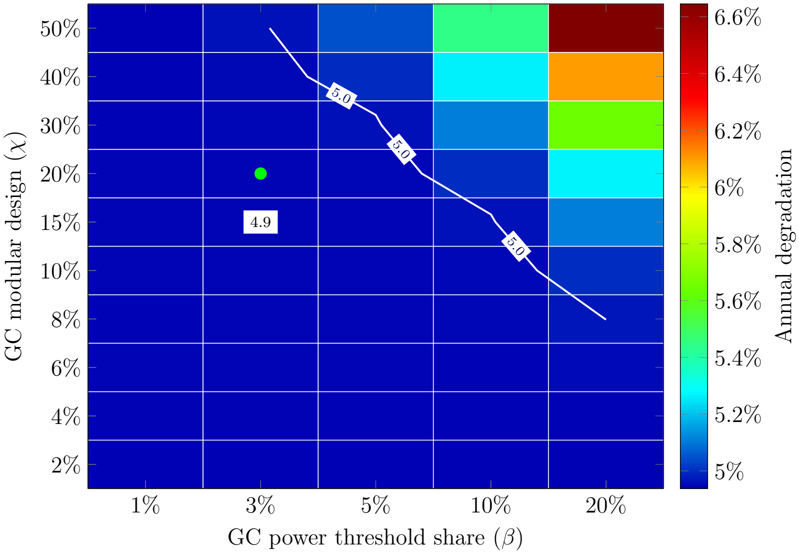

Figure 4.18: Annual battery degradation (q_{loss}) from scenarios, $\mathbb{S}$, and relative to $\beta = 0\%$ (solid line). Marker (●): $\sigma_{\beta 3 \chi 20}$.

---

[6] $P^{h}_{\text{lim}}(k) = \beta \times P^{\text{aux.},k}_{\text{conv}}$

Loss Comparison – AC vs DC

Compared to AC distribution, DC* does not generate savings (+7.7% increase in annual losses), not even with the inclusion of PV and battery storage; see Fig. 4.19. To examine the effect of the GC size, DC* is modelled with a Smaller (S) and Bigger (B) GC. The GC size is determined from (4.9) for $\psi = 10$ A (6.9 kW) and 20 A (13.9 kW) as (DC$^\mathrm{S}$) and (DC$^\mathrm{B}$), respectively. A bigger GC (DC$^\mathrm{B}$) worsens the performance (+19.6%). However, a smaller GC (DC$^\mathrm{S}$) reduces the losses (−10.0%) relative to AC. Reducing the nominal power of the GC shifts the operating points to higher loading and increases the efficiency. Thus, the converters' design is paramount for the performance when considering load-dependent characteristics, and it has proven especially crucial in this comparative study with frequent partial-load GC operation.

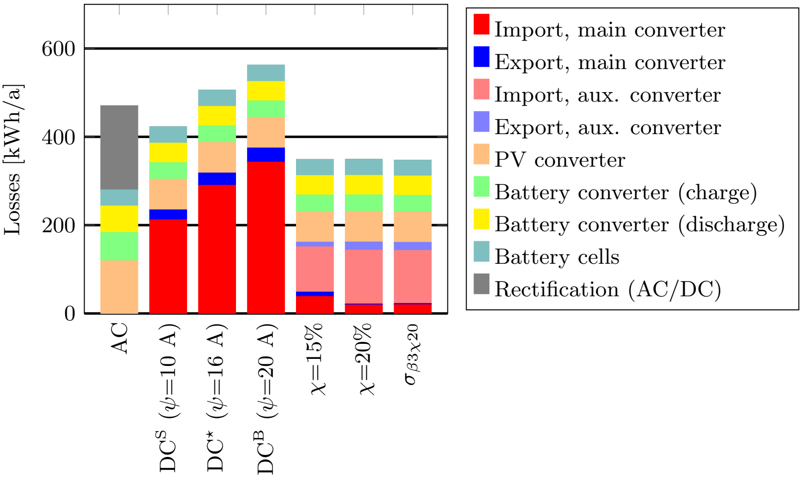

Figure 4.19: Annual system losses per source for AC distribution, DC with varying GC size ($\psi \in 10$–20 A), the PLS with $\chi = 15$ and 20%, and combined PLS and DOO for $\sigma_{\beta 3\chi 20}$.

As for modular design and the PLS, $\chi = 15$ and 20% result in 25.7% annual savings compared to AC distribution. The PV and battery converters have −92 kWh lower losses with DC distribution, while the cells' losses in Fig. 4.19 remain equal and independent of the topology. Suppose the import and export losses from the DC distribution are summed and compared

Table 4.6: LOC with varying electricity price, for $N = 10$ years and $r = 5\%$. $\mathbb{C}_{\mathrm{deg}}$ in (2.20) is calculated with $\mathbb{C}_0^{\mathrm{batt}} = 260$ \$/kWh.

	$\mathbb{C}_{\mathrm{el}}$ [\$/kWh]	$\mathbb{C}_{\mathrm{net}}$ [\$]	$\mathbb{C}_{\mathrm{deg}}$ [\$]	$\sum\mathbb{C}$ [\$]	$\Delta\mathbb{C}^{\mathrm{a}}$ [\$]
AC	0.1	2,873	748	3,621	–
	$\vdots$	$\vdots$		$\vdots$	$\vdots$
	0.5	14,363		15,111	–
DC* ($\psi = 16$ A)	0.1	2,901	754	3,655	34
	$\vdots$	$\vdots$		$\vdots$	$\vdots$
	0.5	14,507		15,261	150
$\chi = 15\%$	0.1	2,793	748	3,541	−80
	$\vdots$	$\vdots$		$\vdots$	$\vdots$
	0.5	13,964		14,712	−399

[a] Relative AC for the same electricity price ($\mathbb{C}_{\mathrm{el}}$).

with the rectification losses of the AC distribution. In that case, the DC reference cases ($\forall\psi$) have higher losses, while the modular operation gives lower losses (−29 kWh/a). As aforementioned, the best-performing $\mathbb{S}$ scenario ($\sigma_{\beta 3\chi 20}$) marginally reduce the aggregated losses. Compared with $\chi = 20\%$, loss-reductions occur for the auxiliary converter and the battery (converter and cells).

Life-Cycle Cost Comparison

Table 4.6 shows the LOC for varying electricity prices ($\mathbb{C}_{\mathrm{el}}$)[7]. The net billing ($\mathbb{C}_{\mathrm{net}}$) dominates the LOC. Relative to AC, DC* does not give any cost-savings. However, a modular GC design with $\chi = 15\%$ presents savings in the range of \$80–399 for the modelled electricity prices.

Office Building

The case setup of the office building outlined in Section 3.3 is used to analyse further the effect of supply (PV) and demand (load) correlation on the DC potential. This analysis examines the hypothesis of increased DC savings

---

[7] The price of bought ($\mathbb{C}_{\mathrm{buy}}$) and revenue from sold electricity ($\mathbb{C}_{\mathrm{sell}}$) are equal in (2.16).

Table 4.7: Grid-tied converter (GC) sizing [kW] for varying PV to load shares in Gothenburg, Denver and Phoenix.

	PV to load share, r_{PV}							
	0%	Ref.[a]	25%	50%	75%	100%	125%	150%
Gothenburg	130[b]	130[b]	130[b]	161	241	322	402	483
Denver	123[b]	123[b]	123[b]	123[b]	143	191	238	285
Phoenix	148[b]	148[b]	148[b]	148[b]	148[b]	168	210	252

[a] Reference PV to load shares from Table 3.4.

[b] GC size set by the peak load demand.

from a stronger correlation between PV and load demand. Furthermore, it examines the effect of the GC design presented in [Paper V]. A parametric sweep is done with varying PV and battery sizes, where the PV is varied as a ratio of annual load demand ($r_{\mathrm{PV}} = 0$–150%). The modelled battery size is derived from the Relative Battery Capacity (RBC) index and a method applied for residential buildings in Sweden [91] as a function of PV array nominal power as

$$\mathrm{RBC} = \frac{\mathrm{E_{batt}}}{\mathrm{E_{PV}}} \tag{4.19}$$

where $\mathrm{E_{batt}}$ is the battery's energy capacity and $\mathrm{E_{PV}}$ the annual PV yield. RBC is modelled for 0–1.5 kWh/kWp for the parametric sweep.

Figure 4.20 shows the effect on DC savings from reference operation ($\chi = 0\%$), relative AC, with varying PV and battery sizes. The whiteout areas represent cases with no DC savings ($\geq$0%), and the dashed line is the reference PV size from Table 3.4. For all three locations, no savings occur without PV (0%)[8]. For Gothenburg, savings occur for $r_{\mathrm{PV}} = 25$–75% without storage. A further expansion of the PV array increases the GC sizing—set by the maximum value of load demand and PV output per Table 4.4—and the export losses. An increase in GC size also results in more frequent partial-load operations, having higher relative losses. To achieve a 150% PV to load share in Gothenburg, the required array size must be 483 kWp, compared to 285 and 252 kWp for Denver and Phoenix, respectively; see Table 4.7. Not only does the PV sizing affect the GC, but an increase in size reduces the self-consumption [104], which

---

[8] Since the battery dispatch is done to maximise self-consumption (see Fig. D.1), no effect is observed for varying RBS with $r_{\mathrm{PV}} = 0\%$.

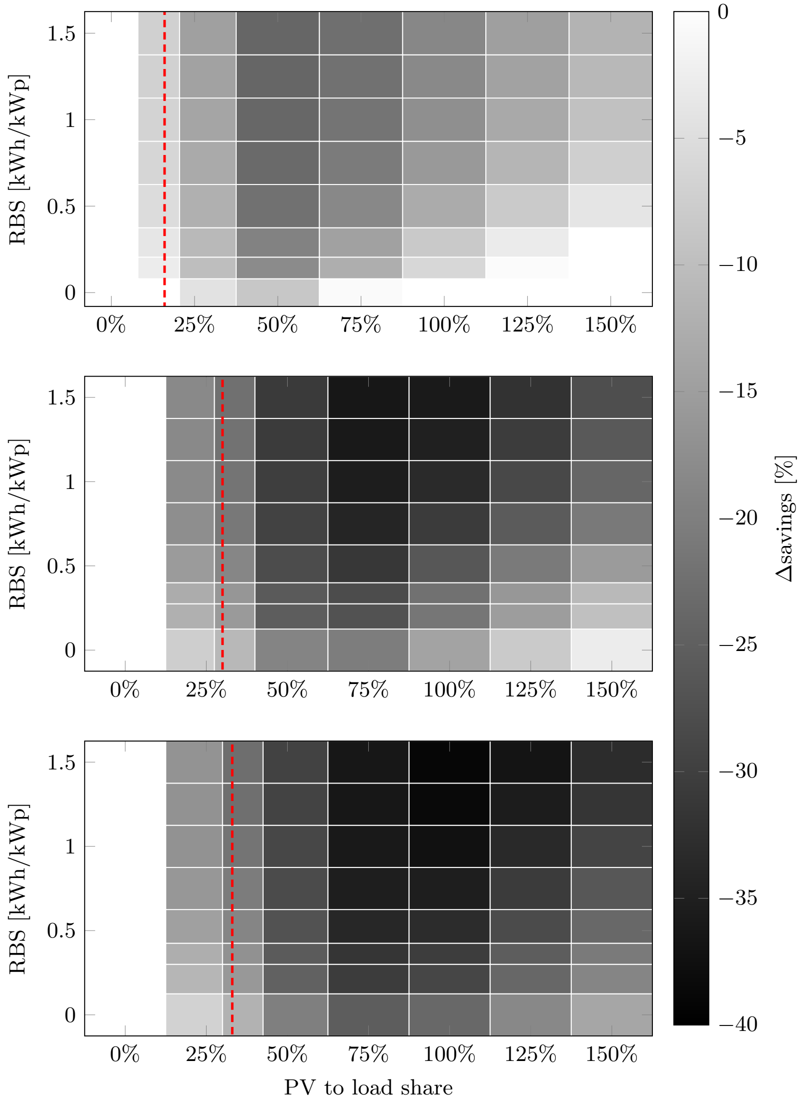

Figure 4.20: Normalised annual losses with DC distribution for varying PV and battery sizes for: Gothenburg (**top**), Denver (**middle**), and Phoenix (**bottom**). The dashed lines are the reference PV sizes from Table 3.4.

in this context results in higher grid export losses. In absolute terms, more significant savings occur for larger DC sources (Fig. B.1), mainly because of the superior performances of the PV and battery converters. The maximum loss savings from Fig. 4.20 and Fig. B.1 are: Gothenburg −24% (5.6 MWh), Denver −36% (9.5 MWh), and Phoenix −39% (12.8 MWh), and relative the load demands (Table 3.4) the savings are 1.8, 3.2, and 3.9%, respectively.

Effect from Self-sufficiency on DC savings

As concluded in previous works, the DC savings potential depends on the PV and load correlation [144], [146], and interaction with the external grid [Papers III–V]. A system's self-sufficiency—derived from (2.23)—quantifies to what extent the load demand is covered from de-centralised generation and, in this context, how much of the demand is covered by PV generation.

The loss savings from DC operation as a function of self-sufficiency for the modelled PV and battery combinations on the office building in Gothenburg is shown in Fig. 4.21. Because of the modelled battery dispatch, the self-sufficiency increases with battery size, and an increase in self-sufficiency means that more of the load demand is supplied from the PV—either directly or from the battery—and thus, less interaction with the grid. Less grid interaction also

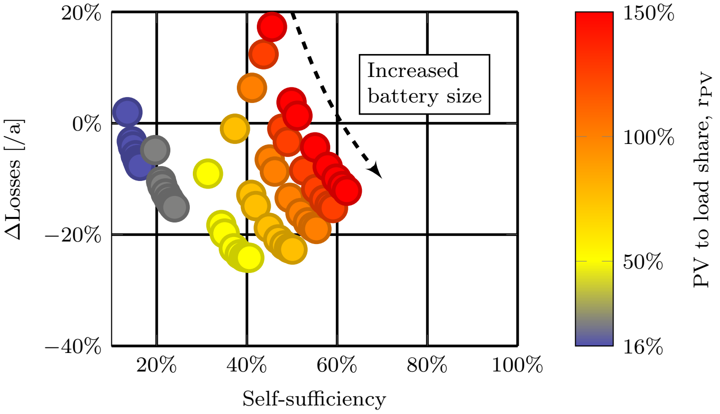

Figure 4.21: Relative loss savings with DC operation as a function of self-sufficiency for the modelled PV and battery combinations (excl. $r_{PV} = 0$) on the office building in Gothenburg.

results in more significant DC savings (for the same $\mathrm{r_{PV}}$). A comparison of the two left-most trends—having the same GC size—highlights the effect of self-sufficiency on savings. Without storage (top markers), the reference PV size ($\mathrm{r_{PV}} = 16\%$) shows no savings, while for $\mathrm{r_{PV}} = 25\%$, DC operation results in annual savings. The most significant relative savings occur at $\mathrm{r_{PV}} = 50\%$ and RBS = 1.5. For PV arrays beyond that, the effect from the GC sizing becomes more significant, resulting in more frequent partial-load operations with higher relative losses and increased PV export losses. Noteworthy is the effect of battery storage on self-sufficiency and savings, where the performance of the smaller arrays is less affected by the storage, while for the larger, the storage sizing can be a decisive factor in achieving DC savings. The trends in Fig. 4.21 are similar for Denver and Phoenix, with the difference that the most significant savings occur for larger $\mathrm{r_{PV}}$; 75 and 100% for Denver and Phoenix, respectively. Furthermore, due to the combination of a higher PV and load correlation and higher solar irradiance—affecting the GC sizing for the same $\mathrm{r_{PV}}$—both the self-sufficiency and savings with DC operation increase for Denver and Phoenix.

Effect from GC Modular Design

To reduce the effect of the GC sizing, the modular design concept from [Paper V] is applied to a case with $r_{\mathrm{PV}} = 100\%$ (net-zero building operation) for all three locations. Figure. 4.22 shows the DC performance relative AC for varying χ and RBS[9]. Now, all scenarios–except $\chi = 0\%$[10] and RBS = 0 for Gothenburg–show superior DC performance regarding annual losses. The most significant effect from the GC design is seen for Gothenburg and RBS = 0, where $\chi = 8$–20% reduces the losses by more than 20% (−5 MWh); see Fig. B.2 and Fig. B.3.

---

[9] The absolute savings are shown in Fig. B.4.

[10] A modular GC design with $\chi = 0\%$ equals one (1) main converter; see Fig. 4.20.

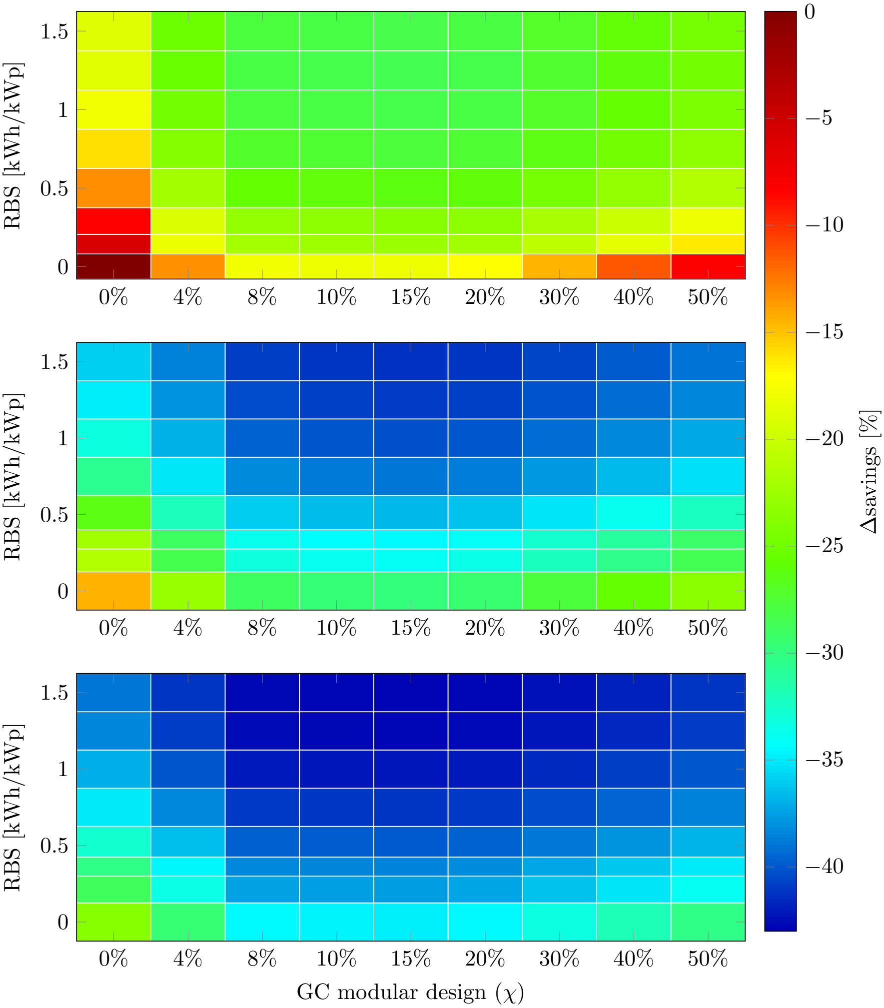

Figure 4.22: Loss savings from modular DC operation versus AC with varying GC design (χ) and battery size for Gothenburg (**top**), Denver (**middle**), and Phoenix (**bottom**).

4.3 Conclusions – AC vs DC Building Distribution

This section concludes the AC and DC building distribution findings in single-family and office buildings. It includes the effect of building location and the proposed enhancement methods for DC distribution.

Single-family Residential Building

Comparing DC_1 and DC_2 reveals a significant loss discrepancy when using constant and load-dependent efficiencies. For this use case, the loss discrepancy is 34% without PV and battery. Analysing the converter loading showed that most interactions occur at partial-load operation with poor efficiency, thus highlighting the importance of accounting for load-dependent efficiency. Therefore, using load-dependent efficiencies is essential when modelling realistic scenarios with a wide operating (power) range.

With load-dependent PEC efficiencies, the losses are reduced by 15.8% with DC operation and PV and battery included. Furthermore, the DC topology increases the PV utilisation by 2.6%, from a 28.6% reduction in the PV-associated losses. The analysis of hourly and seasonal variations in DC savings showed that Spearman's rank coefficient showed the highest correlation (+0.59) between DC savings and available PV generation.

The extended analysis showed that more than adding PV is needed to achieve savings with DC distribution for the studied case. The DC performance marginally improves when doubling the PV size, from +6.7% to +5.4%. However, when adding a battery, DC operation achieves substantial savings (up to 17.7% reduction) as the GC's effect is reduced.

Above all, the results show the relevance of modelling the PEC characteristics with load dependence to account for the efficiency characteristics. Using constant efficiencies is proven inaccurate for the studied case, with frequent partial-load converter operations and, thus, high relative losses.

Effect of Geographical Location

The performance of DC distribution depends on the grid interaction and the correlation between supply and demand. Unlike the findings in [Paper III], the results in [Paper IV] presents DC savings without battery storage; −28.5% (Phoenix) and −19.0% (Borås). This discrepancy comes from how the loss modelling of the PV and battery converters, where [Paper IV] uses constant efficiencies and [Paper III] load-dependant; see Table 4.3. Again, this highlights the discrepancy and the necessity of accounting for the converter efficiency characteristics.

The relative difference between the two locations remains with storage, with more significant savings in Phoenix (−43.6%) compared to Borås (−33.1%). The expanded analysis with varying PV and battery sizes confirms these results and shows more significant savings and higher system efficiency in Phoenix for the same PV and battery configuration. In Borås, the savings increase with the size of the PV array—for the same battery size—while in Phoenix, similar savings are found for the 3.7 and 5 kWp, with reduced savings for 10 kWp. Analyzing the GC losses shows that the PV size has a marginal effect on the import losses, while the effect on the export is more prominent. In Phoenix, the 10 kWp array shows a significant loss increase compared to the others and thus affects the savings potential. The results highlight the effect of converter sizing on the potential benefits of DC distribution and state that careful consideration should be made when designing the system.

Reduced GC Partial-Load Operation – Single-family Building

The proposed DOO reduces the GC losses by eliminating the operation at partial loading while offering SC enhancement. Consequently, the battery throughput and associated losses increase, resulting in varying net loss savings. Net savings are found for $\beta = 1$–5% (up to 16 kWh/a), and the empirical battery degradation shows that the relative effect on annual degradation is marginal ($\leq$0.5 percentage points) compared to the reference battery operation. For $\beta = 10$–20%, the net losses increase compared to DC* despite the reduction in GC losses due to the significant increase in battery-associated losses. Considering the significant battery degradation for $\beta \geq 10\%$ (+1–4 percentage points relative to the reference operation), this operation is not preferred for the studied case.

The proposed Master-Slave GC design achieves savings of up to 157 kWh/a (−31% of the annual losses for DC*). An optimal modular configuration is found for $\chi = 15$–20% and supported from the weighted grid import efficiency characteristics, η^{w}_{imp}. Combining modular and battery DOO results in marginal additional savings; −5.1 kWh/a for $\sigma_{\beta 5 \chi 50}$ relative $\beta = 0\%$, and −1.6 kWh/a for $\sigma_{\beta 3 \chi 20}$ compared with the best-performing case ($\chi = 15\%$).

In general, savings from combined operation occur at low χ and high β from reduced losses of the auxiliary converter. At larger β, the battery-associated losses supersede the GC savings while increasing annual battery degradation.

The DC loss savings relative to AC reflect the reduced LOC, with maximum savings for DC ranging between \$80 and \$399 for a 10-year lifetime and a 5% discount rate. Considering that these savings shall cover the added costs for cabling, converters and compatible appliances, a retrofit to DC distribution is not feasible from an economic perspective in this studied case.

Contrary to previous findings, the results indicate that more than simply incorporating PV and the battery is needed to accomplish loss savings with DC operation. The findings underscore the significance of converter sizing for DC viability, revealing an annual loss reduction of 83 kWh (−16%/a) for DC^{S} compared to $\mathrm{DC}^{\star}$. Nonetheless, restricting the nominal power of grid converters also limits peak power load demands.

Office Building DC Distribution

The results from the parametric sweep of PV and battery sizes show that none of the three office buildings present DC savings without PV. With PV, DC operation in Denver and Phoenix results in annual loss savings for all combinations ($r_{\mathrm{PV}}>0$), with up to 40% (−13 MWh/a) reductions; −3.2 and −3.9% relative the total energy demands for Denver and Phoenix, respectively. For Gothenburg, fewer PV and battery combinations result in loss savings with DC operation, and the necessity of battery storage is more evident, especially for larger PV arrays. As the GC size depends on the PV power, the savings reduce after a specific PV size, with peak loss savings at $r_{\mathrm{PV}} = 50\%$ for Gothenburg (−24%/a), 75% in Denver, and 100% in Phoenix. Thus, the GC sizing shall be designed to reduce frequent partial-load operation, and having too much PV affects both the sizing and the export losses.

For the modelled net-zero offices ($r_{\mathrm{PV}} = 100\%$), the modular GC design has the most significant effect on the performance in Gothenburg and without battery, reducing the relative DC losses by 22% (−5 MWh/a). The optimal modular design configuration is around $\chi = 10$–15%, similar to the findings for the single-family building [Paper V]. Furthermore, all modular GC design combinations ($\chi \in 4$–50%, and RBS = 0–1.5) result in annual loss savings compared to AC.

CHAPTER 5

Battery Loss Modelling: Effect on Annual Performance

This chapter is based on Paper I and examines the effect of battery loss modelling on the building's performance, using the case in Section 3.1. Three battery models are compared, including the often found [16], [17], [23] approximation of a constant round trip efficiency. The other two models use the *Rint* battery model (Fig. 2.2) with either a constant or current-dependant internal resistance. Laboratory measurements on a single cell are performed to establish the OCV and resistance characteristics. The proposed *Rint* models are verified against the measured output voltage for conformity. The analysis includes a combination of PV and load profiles—16 cases in total—to assess the effect of varying operating conditions.

5.1 Methodology

Battery Cell Characterisation

To accurately represent the battery's characteristics, tests were done on a single cell to establish the internal cell voltage as a function of SOC. From this, it was then possible to determine the internal resistance variation as a

Table 5.1: Technical specifications of the $LiFePO_4$ battery cell used for testing and modelling.

Parameter	Value
Chemistry	$LiFePO_4$
Nominal capacity, Q_{nom}^{cell}	12 Ah
Nominal voltage, U_{nom}^{cell}	3.2 V
Charge/discharge cut-off voltage	3.65/2 V
Internal resistance, R_0	3 mΩ

function of current using (2.8). Table 5.1 shows the technical specifications for the $LiFePO_4$ battery cell used in the laboratory tests.

Open-Circuit Voltage and Resistance Determination

To establish the relation between battery SOC and voltage, u_{cell}, charging and discharging were done at 0.12 A (0.01 C). The lower C-rate was chosen per previous works' recommendation [87], [147], [148] to reduce the dynamics excited in the cells. The test was done for the complete SOC interval (0–100%) at room temperature using a Gamry REF 3000 and a PEC ACT 0550. Further measurements were conducted in the range 0.36–18 A (0.03–1.5 C) to determine the resistance at higher currents to cover the operating range in a residential application. The results were then fed into (2.8) to establish the internal resistance dependency as a function of the battery current.

Figure 5.1 shows the charge and discharge measurement results and the battery's SOC limits used in the system modelling (15–90%). The selected SOC range gives the battery converter a stable voltage output. The cell has a difference between the OCV $f(\text{SOC})$ for charge and discharge, caused by a significant hysteresis effect, which is confirmed in other studies on LiFePO4 [89], [90]. To account for this difference, a linear approximation of the OCV, as the average value from charge and discharge [87] (u_{ocv}^{lin}) is given as[1]

$$u_{OCV}^{lin}(SOC) = a \times SOC + b \quad \forall SOC \in 15 - 90\%. \tag{5.1}$$

Using (2.8), and the average value for SOC ∈ 15–90% for different C-rates,

---

[1] With a = 0.00133 and b = 3.234.

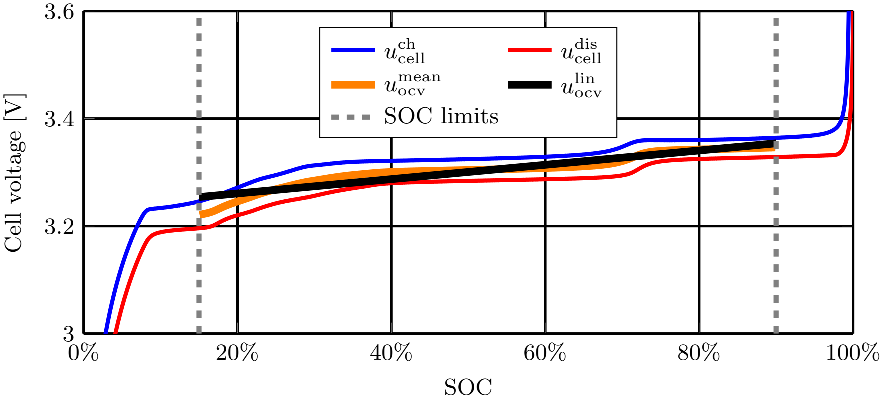

Figure 5.1: Battery cell voltages (u_{cell}) for charge and discharge as a function of SOC at 0.12 A (0.01 C) and an OCV approximation from the mean value ($u_{\text{ocv}}^{\text{mean}}$) and a linearisation of the mean approximation ($u_{\text{ocv}}^{\text{lin}}$).

gives the relation between the internal resistance (r) and current (i_{cell}) as presented in Table 5.2. The measured resistance can be expressed with a curve fit as a function of current as

$$r_{\text{cell}}^{\text{fit}}(i_{\text{cell}}) = \frac{p_1 i_{\text{cell}}^2 + p_2 i_{\text{cell}} + p_3}{i_{\text{cell}} + q_1} \tag{5.2}$$

where the numerical values (p_1–p_3 and q_1) are shown in Table C.3. The measurements and curve fit are also shown in Fig. 5.2 with R_0 from Table 5.1. There is an explicit current dependency on the resistance, especially for low C-rates. It is also evident that the value given in the data sheet (3 mΩ from Table 5.1) does not accurately represent the internal resistance and is significantly erroneous at low C-rates. Even at a C-rate of 1.5, the internal resistance value is more than three times the value given in the data sheet. Results from a high-frequency Electrochemical Impedance Spectroscopy (EIS) sweep showed that the resistance in the range of 1–10 kHz was around 2 mΩ [47], i.e., even lower than the data sheet value even for low currents. Accordingly, the effective resistance is much lower for an application with high-frequency content. However, for a building application and assuming full polarisation in the cells, the data sheet value becomes far too low, as can be noted in Fig. 5.2. Figure 5.2 also shows the cell losses using $r(i_{\text{cell}})$ and R_0, where it is

Table 5.2: Modelled relation between the battery's current and internal resistance, $r^{\text{cell}}_{\text{measured}}(i_{\text{cell}})$.

Current, i_{cell} [A]	**C-rate [Ah^{-1}]**	$r^{\text{cell}}_{\text{measured}}$ (i_{cell}) **[mΩ]**
0.12	0.01	185.4
0.36	0.03	78.3
1.2	0.10	36.1
2.0	0.17	29.0
3.0	0.25	23.6
6.0	0.50	19.1
12.0	1.00	14.0
18.0	1.50	11.0

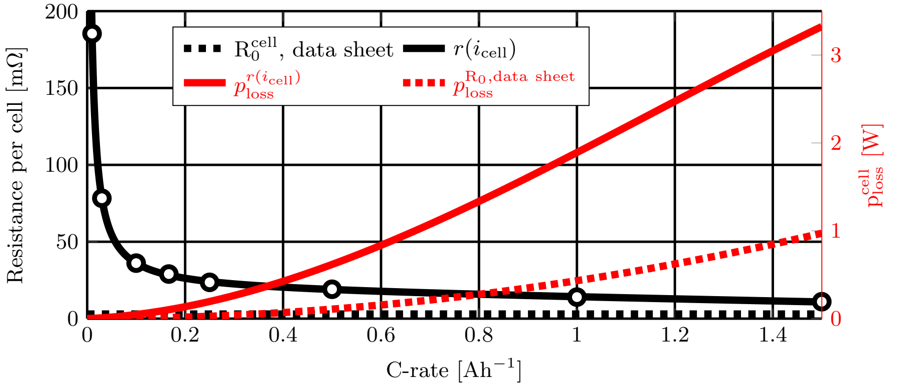

Figure 5.2: Measured (points) and curve fitted cell resistance (black line) as a function of current, $r(i_{\text{cell}})$ and the internal resistance R_0 (dashed black line) from Table 5.1. The cell losses using $r(i_{\text{cell}})$ and internal resistance, R_0 (red lines).

evident that the current is the driving force for the losses, and when ignoring the resistance's current-dependency, the losses are underestimated.

Battery Model Verification

To quantify the accuracy of the *Rint* models, the measured cell current (i_{cell}) is used to calculate the cell voltage and then compared with the measured voltage ($u_{\text{cell}}^{\star}$). Five battery models are evaluated:

- $u_{\text{ocv}}^{\text{lin}} + \text{R}_0$—linear approximation of the OCV as a function of SOC (see Fig. 5.1), and the internal battery resistance (R_0) from the data sheet, see Table 5.1.

- $u_{\text{ocv}}^{\text{lin}} + r(i_{\text{cell}})$—linear OCV approximation and current–dependant resistance, see Table 5.2.

- $u_{\text{ocv}}^{\text{mean}} + \text{R}_0$—OCV approximation of the mean value of charge and discharge (see Fig. 5.1) and R_0.

- $u_{\text{ocv}}^{\text{mean}} + r(i_{\text{cell}})$—mean OCV approximation and current-dependant resistance.

- $u_{\text{ocv}}^{\text{mean}} + r(i_{\text{cell}}; \text{SOC})$—mean OCV approximation and acknowledging the resistance's SOC [149] and current dependency. The SOC dependency is found for the modelled SOC range using (2.8) and calculated for each current.

Figure 5.3 shows the measured ($u_{\text{cell}}^{\star}$) and modelled voltages. Figure 5.3a, shows the results for the whole measurement period and the mean OCV approximation ($u_{\text{ocv}}^{\text{mean}}$), and in Fig. 5.3b, a close-up is shown for $i_{\text{cell}} = 0.36$ A. Using R_0 underestimates the voltage during charge and overestimates it during discharge. Using $u_{\text{ocv}}^{\text{mean}}$ from Fig. 5.1 gives an accurate representation of the curve shape, but for R_0, the modelled voltage has an offset from the measured values. This offset confirms that the data sheet value for R_0 is inaccurate for modelling the voltage profile using a single-resistance model. For $r(i_{\text{cell}})$, the values align better with the measurements. Similarly, in Fig. 5.3c—using the linear OCV approximation—the single-resistance model using R_0 gives an offset to the measured voltage.

The Root-Mean-Square Error (RMSE) in Fig. 5.4 quantifies the modelled voltage discrepancy. As aforementioned, the negligence of the resistance's current dependency results in the most significant discrepancies from the measurements. For the linear ($u_{\text{ocv}}^{\text{lin}}$) and mean ($u_{\text{ocv}}^{\text{mean}}$) approximations, the RMSEs are 38.3 and 37.3 mV, respectively using R_0. The resistance modelling has a much more significant effect on the discrepancy than the OCV approximation. Including the SOC dependency only marginally improves the modelled accuracy (1.4 mV), comparing the last two bars.

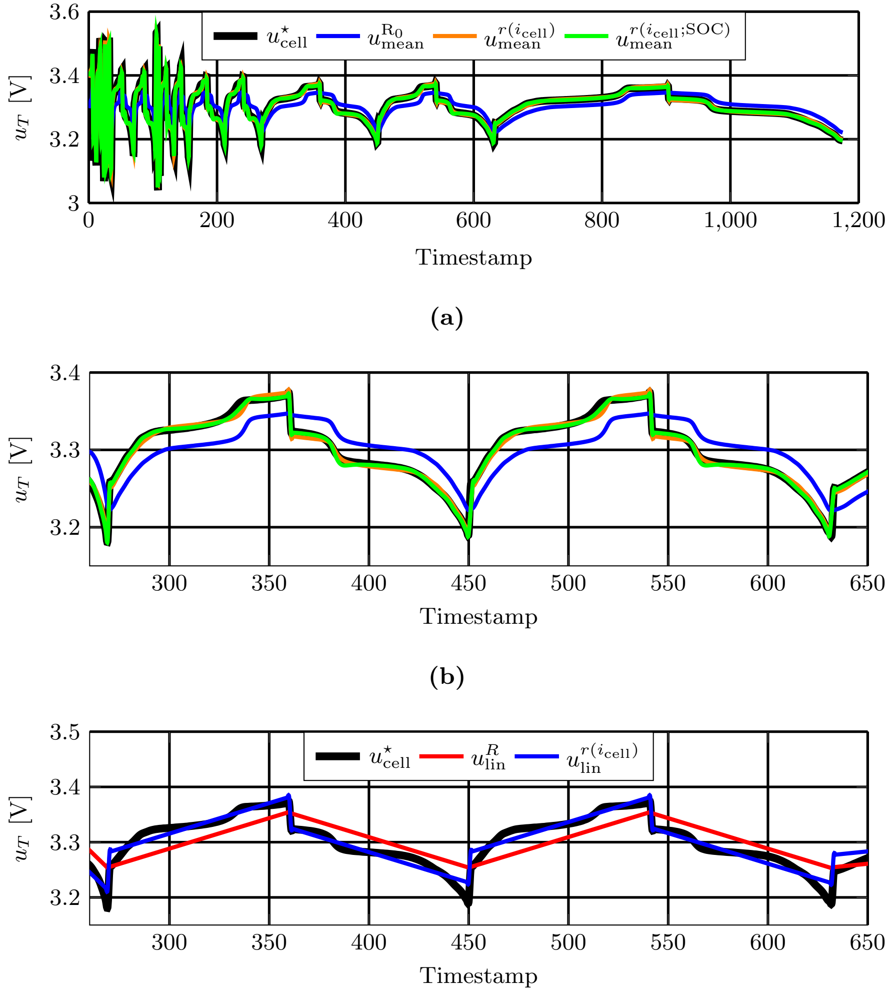

(a)

(b)

(c)

Figure 5.3: Measured ($u^{\star}_{\text{cell}}$), thick black line, and modelled cell voltages for the measurement period **(a)** and a close-up **(b)** for $i_{\text{cell}} = 0.36$ A, both using the mean OCV approximation, and **(c)** a close-up using the linear OCV approximation.

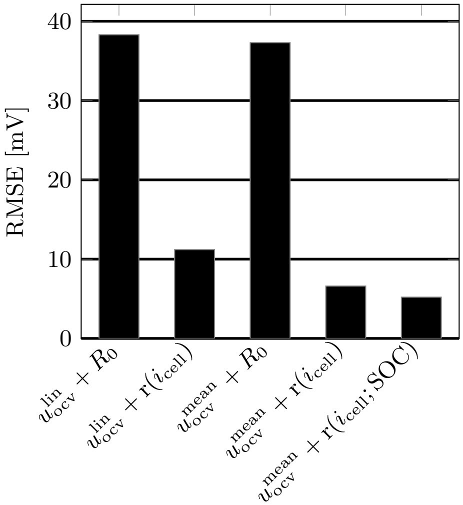

Figure 5.4: Root-mean-square error (RMSE) from measured cell voltage for the compared models.

Battery Converter Characterisation

The connection between the PV array and the battery can be made via AC or DC coupling, where the common point of connection in the former case is AC and DC in the latter, both configurations offering different advantageous [150], [151]. The battery converter can also have a single or two-stage topology, where for a single-stage converter, the battery is connected directly to the converter's DC link, whereas, in a two-stage topology, a DC/DC converter regulates the voltage to boost the DC/AC conversion performance [152]. The converter's characteristic is taken from the results in Section 3.6 for the bi-directional AC/DC converter.

Case Analysis and System Modelling

The derived battery models are applied to the use case of RISE Research Villa; see Section 3.1, and evaluated for an entire year's operation.

Several PV and load sizes were derived from the reference case to extend the case analysis. If the reference PV array size (3.68 kWp) is denoted 1 PV and equals 50% of the annual energy demand ($r_{\mathrm{PV}} = 50\%$), the other array sizes are 2 and 4 PV. Furthermore, two load cases are included; 'low' (1 Load) and 'high' (2 Load). To summarise, the analysis includes the following scenarios:

A: 1 PV/1 Load; $r_{\mathrm{PV}} = 50\%$

B: 2 PV/1 Load; $r_{\mathrm{PV}} = 100\%$

C: 2 PV/2 Load; $r_{\mathrm{PV}} = 50\%$

D: 4 PV/2 Load; $r_{\mathrm{PV}} = 100\%$

where 'B' equals a net-zero energy building, Scenario 'C' has the same r_{PV} as the reference case but with an increase power from PV (charging) and load demand (discharging). Scenario 'D' combines the net-zero case with an up-scaled PV and load scenario.

The required number of series-connected cells ($\mathrm{n_{cell}}$) is calculated using (2.5) and by matching the nominal battery voltage ($\mathrm{U_{nom}^{batt}}$) with the PEC's nominal voltage ($\mathrm{U_{nom}^{conv.}}$) from Table C.1. Using (2.4) with $\mathrm{m_{strings}} = 1$–2 and the "big cell" approximation [153] gives two battery sizes; 9.1 and 18.2 kWh. The maximum power ($\mathrm{P_{conv}^{max}}$) for charge and discharge is restrained by the PEC. Here, two PEC sizes are used: 3.6 kW and 7.2 kW. The former is the PV array size in the reference case, and the latter doubles to match the '2 PV' case.

The battery operates with the dispatch algorithm adopted from [154], and Algorithm 1 describes its operation. Here, η_{tot} represents the combined efficiency for the battery cell and converter or the constant round trip efficiency. A threshold power limit ('threshold' at 1% of the rated power) prevents the initial loss peak from the converter; see Fig. C.1. The battery pack voltage, $u_{\mathrm{batt}}(t)$ is adjusted for in the next time step using the internal resistance, $\mathbb{R}$ as either $\mathrm{R_0}$ or $r(i_{\mathrm{cell}})$[2]. Lastly, the battery's SOC level is adjusted using (2.6) for the next time step.

Acknowledging the PEC's load-dependency for the *Rint* models; (2.7) and (2.9) can be generically expressed as

$$e_{\mathrm{loss}}(t) = \int_{t_1}^{t_2} \left(\mathbb{R} i_{\mathrm{cell}}^2(t) \mathrm{n_{cell}} \mathrm{m_{strings}} + (1 - \eta_{\mathrm{conv}}(s))\, p_{\mathrm{batt}}(t)\right) \mathrm{d}t \tag{5.3}$$

where η_{conv} is the converter efficiency from Fig. C.1.

---

[2] This is only done for the *Rint* models having a voltage–current dependency.

Algorithm 1: Battery dispatch

```
if $pv(t) < load(t)$ then
    if available SOC and $p_{dis} \geq$ threshold then
        $p_{\mathrm{batt}}(\mathrm{t}) = \max[\mathrm{SOC}_{\mathrm{min}} - SOC(\mathrm{t}),\ pv(\mathrm{t}) - load(\mathrm{t}),\ -\mathrm{P}_{\mathrm{conv}}^{\mathrm{max}}]/\eta_{\mathrm{tot}}$;
        $p_{\mathrm{grid}}(\mathrm{t}) = p_{\mathrm{batt}}(\mathrm{t}) + load(\mathrm{t}) - pv(\mathrm{t})$;
    else
        $p_{\mathrm{grid}}(\mathrm{t}) = load(\mathrm{t}) - pv(\mathrm{t})$
    end
else
    if available SOC and $p_{ch.} \geq$ threshold then
        $p_{\mathrm{batt}}(\mathrm{t}) = \max[\mathrm{SOC}_{\mathrm{max}} - SOC(\mathrm{t}),\ pv(\mathrm{t}) - load(\mathrm{t}),\ \mathrm{P}_{\mathrm{conv}}^{\mathrm{max}}]\eta_{\mathrm{tot}}$;
        $pv_{\mathrm{exp}}(\mathrm{t}) = pv(\mathrm{t}) - load(\mathrm{t}) - p_{\mathrm{batt}}(\mathrm{t})$;
    else
        $pv_{\mathrm{exp}}(\mathrm{t}) = pv(\mathrm{t}) - load(\mathrm{t})$;
    end
end
$i_{\mathrm{batt}}(t) = p_{\mathrm{batt}}(t)/u_{\mathrm{batt}}(t)$;
$u_{\mathrm{batt}}(\mathrm{t}+\Delta\mathrm{t}) = u_{\mathrm{OCV}}(t) + \mathbb{R}i_{\mathrm{batt}}(\mathrm{t})$;
$SOC(\mathrm{t}+\Delta\mathrm{t}) = SOC(t) + \int i_{\mathrm{batt}}(t)dt/Q_{\mathrm{batt}}^{\mathrm{rated}}$;
```

Figure 5.5 shows the share of converter and cell losses for the 9.1 kWh battery modelled as a *Rint* model using $r(i_{\mathrm{cell}})$, and for the power constraints $\mathrm{P}_{\mathrm{max}}^{\mathrm{conv}} = 3.6$ and 7.2 kW. The coloured areas show the split over the converter loading for $\mathrm{P}_{\mathrm{max}}^{\mathrm{conv}} = 3.6$ kW and the dashed line for $\mathrm{P}_{\mathrm{max}}^{\mathrm{conv}} = 7.2$ kW. At lower loading, the losses are dominated by the converter's performance. However, as the loading increases, the cell losses become more prominent and are driven by the increased current and improved performance of the converters at higher powers; see Fig. C.1. At full loading, the loss ratio becomes 60/40, thus highlighting the necessity to account for the cell losses to have an accurate loss representation.

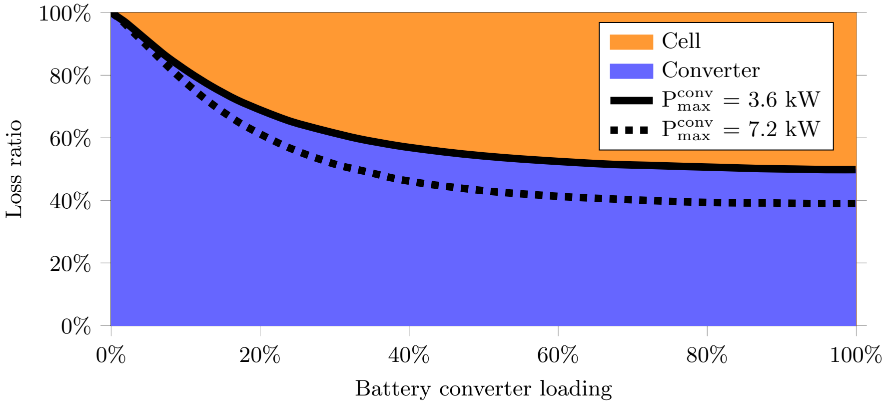

Figure 5.5: Loss split between converter and cell losses using $P_{max}^{conv} = 3.6$ and 7.2 kW and with a varying resistance, $r(i_{cell})$, over the battery system's loading range.

5.2 Results and Discussion – Battery Loss Modelling

The round trip efficiency results include the losses from the PEC and cells. In this comparison, the round trip efficiency is set to 90%, which is typically used in related works, e.g., [18], [20], [27], [155]. The *Rint* models are modelled with constant and current-dependant resistance and the PEC efficiency characteristic from Fig. C.1.

The model verification shows marginal improvements (Fig. 5.4) using the mean values from charge and discharge for the OCV approximation (u_{cell}^{mean}) compared to the linear (u_{ocv}^{lin}). Thus, the latter is used in the system performance evaluation.

Cell Current and Resistance

The distribution of cell currents from annual operation of the reference case (1 PV/1 Load) are shown in Fig. 5.6a with $P_{max}^{conv} = 7.2$ kW. Higher peak values are consequently observed for the smaller battery (9.1 kWh), as the assumption of cell uniformity distributes the current equally in the strings (for $m_{strings}>1$) as per (2.2). Numerically, the average currents are 1.0 A and

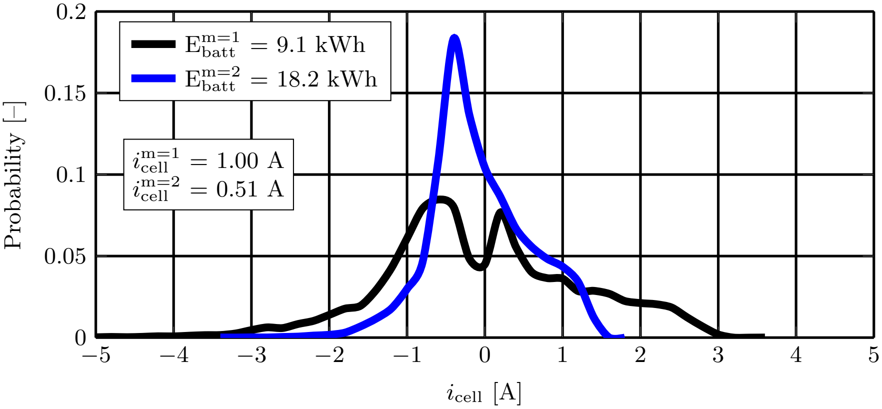

(a)

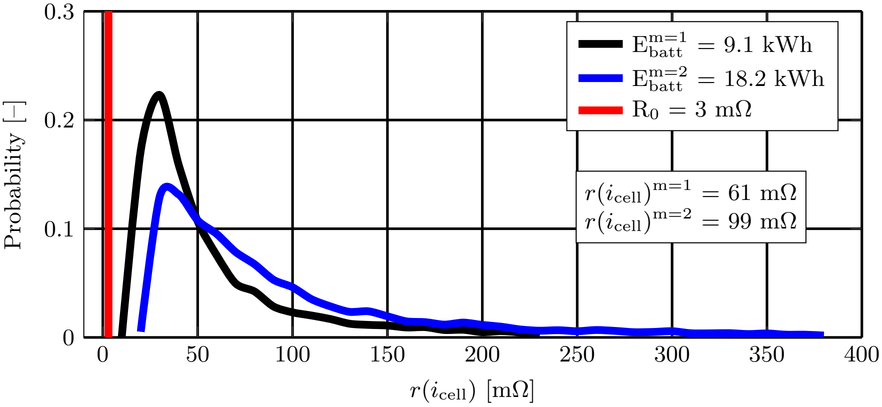

(b)

Figure 5.6: Distribution of **(a)**: battery cell currents, i_{cell} and **(b)**: cell resistance, $r(i_{\mathrm{cell}})$ and data sheet resistance, R_0. Included are also the average cell currents ($i_{\mathrm{cell}}^{\mathrm{m=n}}$) and resulting resistances ($r(i_{\mathrm{cell}})^{\mathrm{m=n}}$).

0.51 A for the smaller and larger size, respectively. This difference in current is reflected in the resistance distribution (Fig. 5.6b), where the average resistance is >50% higher for the larger battery. The resistance distribution shows that a single value does not accurately represent the battery's characteristics as it fails to capture the variations. Comparing the annual averages $(r(i_{\text{cell}})^{\text{m=n}})$ with the data sheet value, R_0, shows that the latter greatly underestimates the resistance throughout. Thus, using a single (constant) resistance is inaccurate when modelling battery losses.

Annual Battery System Losses

The annual battery system losses are shown in Fig. 5.7 for $\text{E}_{\text{batt}} = 9.1$ kWh (Fig. 5.7a and Fig 5.7b) and $\text{E}_{\text{batt}} = 18.2$ kWh (Fig. 5.7c and Fig. 5.7d). For the *Rint* models, the losses are separated between the converter and cells, with most losses originating from the converter. For neither of the 16 modelled scenarios is the *Rint* model with R_0 accurate to estimate the losses, with a relative discrepancy of −20.5 to −38.6% (35–112 kWh/a) compared to the proposed benchmark model with a current-dependant resistance variation. Together with the findings in Section 5.2, it is fair to conclude that when using the *Rint* model, the resistance's current dependency must be acknowledged to estimate the battery's performance accurately. Using $\eta_{\text{RT}}^{90\%}$ gives a proportional relation between losses and battery throughput and a marginal effect from the converter size when ignoring the load-dependent characteristics. Relative to the benchmark model, the loss discrepancies vary for the modelled scenarios: −5% to 17% for the smaller and 3–29% for the larger battery.

Battery Cell Loss Share

As shown in Fig. 5.7, the cell's loss share is significant, and the relative influence varies with the modelled cases (A–D) and battery size. Figure 5.8 shows the current-dependant resistance model's ratios per battery and converter sizes. Larger battery powers—going from case A to D—shift the operation to higher loading. This shift results in an enhanced effect from the cells, as seen in Fig. 5.5. When comparing the two sizes for the same case and converter size, it is clear that the larger battery has a lower loss share from the cells. Analysing the converter loading's probability distribution shows similar conditions and thus excludes the effect from the converter. The variation in cell current—from the difference in parallel strings—instead explains the difference (see Fig. 5.6a). For the smaller battery (9.1 kWh), all cells are modelled in one string ($\text{m}_{\text{strings}} = 1$), while for the larger battery, two strings are

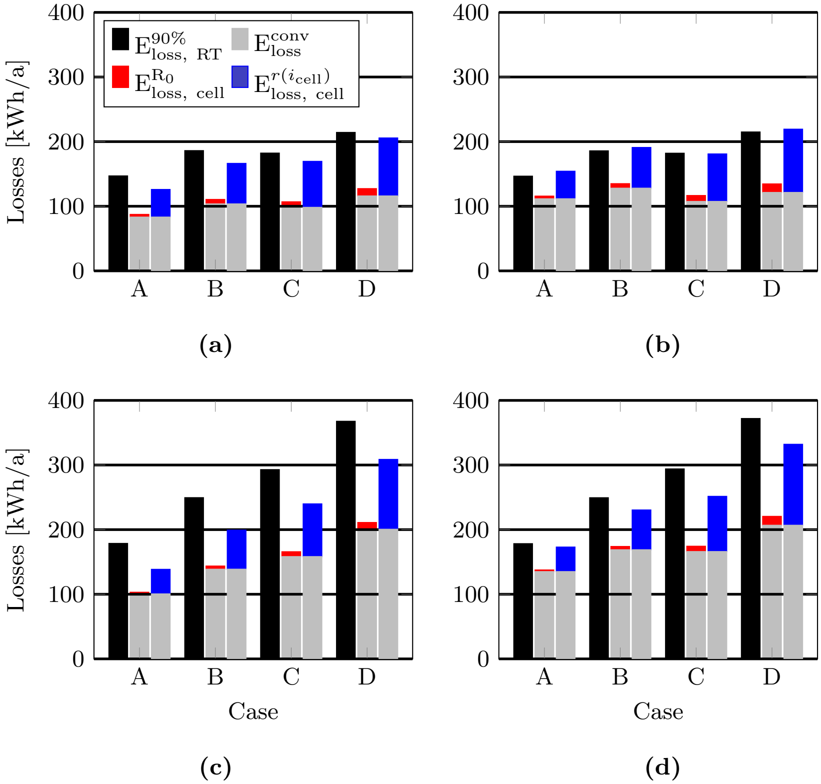

(a) **(b)**

(c) **(d)**

Figure 5.7: Annual battery system losses for the three models divided per loss origin (for the *Rint* models) and for the studied scenarios. Figure: **(a)** $E_{\mathrm{batt}} = 9.1$ kWh and $P^{\mathrm{conv}}_{\mathrm{max}} = 3.6$ kW, **(b)** $E_{\mathrm{batt}} = 9.1$ kWh and $P^{\mathrm{conv}}_{\mathrm{max}} = 7.2$ kW, **(c)** $E_{\mathrm{batt}} = 18.2$ kWh and $P^{\mathrm{conv}}_{\mathrm{max}} = 3.6$ kW, and **(d)** $E_{\mathrm{batt}} = 18.2$ kWh and $P^{\mathrm{conv}}_{\mathrm{max}} = 7.2$ kW.

modelled in parallel. These parallel strings divide the battery current equally during operation and thus halve the cell current (i_{cell}) as per (2.2). As the current drives the cell losses (see (2.9)), the larger battery has lower losses for the same power. From the annual average converter loading and loss shares, the results are fitted to the loss ratios from Fig. 5.5, as seen in Fig. 5.9. The added lines for the larger battery confirm that the battery with two parallel

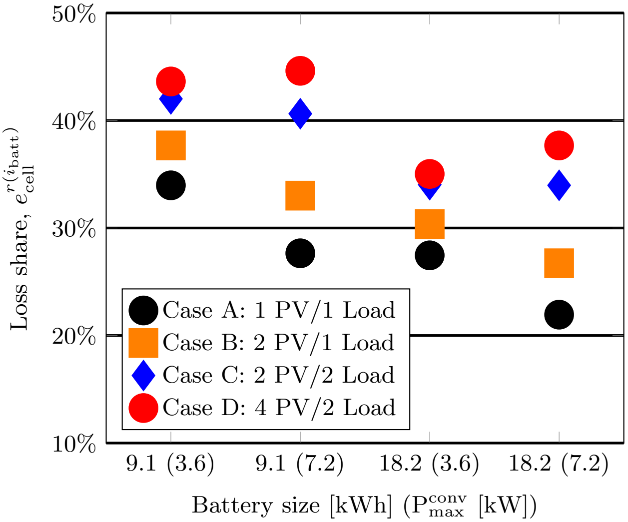

Figure 5.8: Variation in battery cell loss share per battery configuration for case A–D, using the current-dependant internal resistance model.

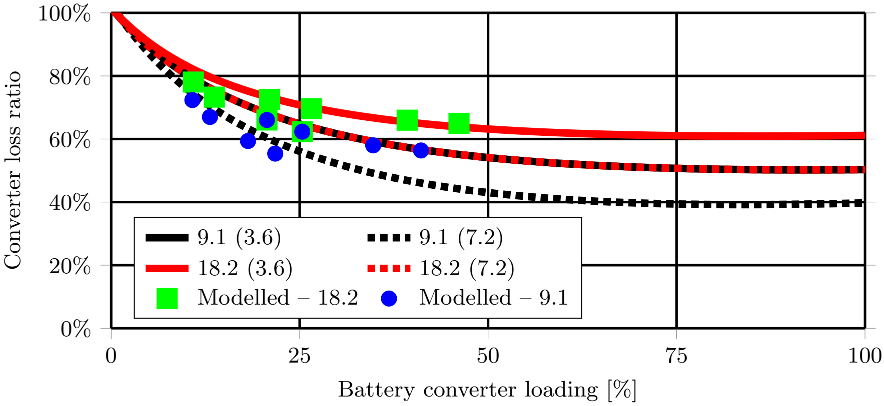

Figure 5.9: Converter loss ratios (lines) and the modelled values using the annual mean converter loading and loss ratios.

strings has lower relative cell losses for the same power. The results show that the battery losses cannot be ignored and that the loss-shares exceed 40% for the proposed *Rint* benchmark model with its current-dependant resistance.

5.3 Conclusions – Battery Loss Modelling

This work performs a comparative study of the technical performance of a PV and battery system using three battery models: two *Rint* models and one using a (constant) round trip efficiency. One of the *Rint* models uses experimentally obtained values of the battery cell's resistance as a function of current and the battery converter's efficiency characteristics. The results highlight the importance of having an adequate battery system model when evaluating performance under varying operating conditions and that cell losses must be included for accurate loss modelling.

Measurements on a $LiFeP0_4$ battery cell show a substantial variation in internal resistance as a function of current, and the data sheet value does not give an accurate representation at any point of operation. The proposed *Rint* model with a linear OCV variation of SOC and current-dependant internal resistance is proven accurate for modelling the cell's voltage characteristics. The battery PEC efficiency characteristics also support the necessity of accounting for the load variations as the power dependency is evident.

Results show that neither a round trip efficiency nor the data sheet resistance model accurately estimates the battery system's losses. The *Rint* model using R_0 fails to give accurate results for all studied scenarios. Despite considering the quadratic loss dependency, a single (fixed) resistance is insufficient, and the annual loss discrepancy is—at worst—38.6% for the studied scenarios. As for the round trip efficiency, the discrepancy depends on the modelled case and battery system size. Without pre-modelling knowledge, choosing an adequate round trip efficiency is thus tricky.

The results also prove that cell losses cannot be ignored and that its effect enhances with increased converter loading. For the studied scenarios, the cells' contribution range between 22–45%.

CHAPTER 6

Airport Micro Grid Modelling – PV and Battery to Aid Transport Electrification

This chapter is based on Paper II and evaluates the techno-economic role of PV and battery storage for Visby Airport with the use-case outlined in Section 3.5. The airport is modelled as a micro grid in a forward-looking scenario with increased energy and power demands from electric aviation (EA) and electric vehicles (EVs). The evaluation includes four battery dispatch operations—one of which is a novel algorithm—and their effect on grid interaction (energy demand and peak powers), system self-consumption and battery degradation. Figure 6.1 outlines the modelling procedure, including the energy infrastructure power flows, input data, scenario analysis and result generation.

6.1 Methodology

Electric Aviation and Vehicle Charging Demands

A simulation model [156] is used to quantify the power demand from EA charging. The demand assumes 16 daily flights for six domestic short-haul

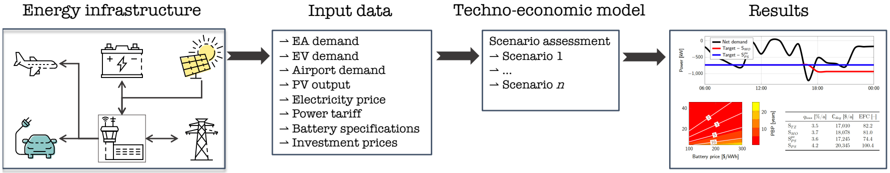

Figure 6.1: Modelling procedure outline.

flights (200 km), capable of transporting 300+ passengers in each direction using a 19-seat aircraft. The EA use independent fast-charging with a SOC-dependent power [156], [157] as

$$p_{\text{ch}}^{\text{EA}}(\text{SOC}) = \begin{cases} 2\ \text{C}, & \text{if } 40\% \geq \text{SOC}(t) > 0\% \\ 1\ \text{C}, & \text{if } 80\% \geq \text{SOC}(t) > 40\% \\ 0.5\ \text{C}, & \text{otherwise} \end{cases}$$

The EV charging demand is based on the flight schedule, with the number of EVs arriving before each departure, N_{EV}, calculated as

$$\text{N}_{\text{EV}} = \left(\frac{\text{N}_{\text{seat}}^{\text{ac}} \text{CF}_{\text{ac}} \text{S}_{\text{pax}}^{\text{veh}}}{\text{N}_{\text{pax}}^{\text{veh}}} \right) \text{S}_e \tag{6.1}$$

where $\text{N}_{\text{seat}}^{\text{ac}}$ is the seating capacity per aircraft, CF_{ac} the cabin factor, $\text{S}_{\text{pax}}^{\text{veh}}$ the share of passengers arriving by car, $\text{N}_{\text{pax}}^{\text{veh}}$ the number of passengers per car, and S_e the share of electric vehicles in the car fleet. For each departure, N_{EV} is sampled from probability density functions for arrival time (in minutes before the flight departure), parking duration, and battery SOC at arrival [Paper II].

Solar Photovoltaic Design and Modelling

Three locations for PV deployment were identified (Fig. 6.2), considering glare risks to air traffic and aviation system [158] and glint from sun reflection, disturbance of radio communication system and other instruments, and physical obstacles at the airport. Location 1 is a ground-mounted system near the airport building and communication tower. Location 2 is the parking space, with roof-mounted PV panels, located relatively close to the Airport Traf-

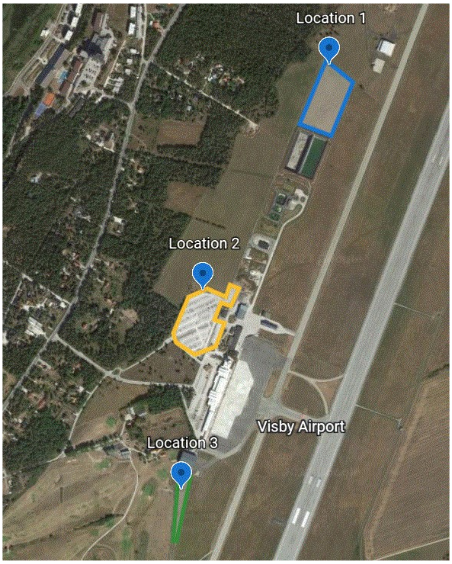

Figure 6.2: Potential locations for PV arrays at Visby Airport.

fic Control Tower with a potential risk of electromagnetic interference to the communication system [159], [160]. Location 3 is a ground-mounted array system southwest of the main airport building.

The array sizes are determined from the available space to maximise the annual yield, and the output is modelled using a Typical Meteorological Year (TMY), 10 km grid, Meteonorm weather and the HelioScope PV simulation software [161]. In locations 1 and 3, the panels have a fixed tilt angle of 35°, due south (azimuth angle of 180°) and an inter-row spacing of 4 meters. In location 2, the solar panels are on the parking roof with a tilt angle of 5°. For most cases, the azimuth angles are based on the parking orientation (156°). Table 6.1 shows the spatial planning and performance.

Using (2.22), Fig. 6.3 shows the SC and SS for the three PV arrays (PVn) and the aggregated generation (PVtot). The results include four load scenarios: 'All loads' (BAU+EA+EV), BAU, EA, and EV. The load demand consumes all generation from PV3 (Fig. 6.3a) in the BAU scenario—and consequently also for 'All loads'—meaning that this array alone is relatively small in comparison to the load demand and further proven by a SS below 10%

Table 6.1: Solar array designs and specifications for the modelled locations.

Spatial planning	**PV1**	**PV2**	**PV3**
Array area [m^2]	12,732	6,968	2,880
Number of modules	2,632	3,168	556
Inter-row spacing [m]	4	– (rooftop)	4
Tilt angle[a] [°]	35	5	35
Azimuth angle(s)[a] [°]	180	156, 110 and 21[b]	180
Performance			
Total array power [kW]	974	1,172	206
Annual yield [MWh]	1,083	1,125	230
Specific yield [kWh/kWp]	1,112	960	1,116
Performance ratio [%]	82.7	85.3	83.0
Shading loss [%]	4.3	0.1	4.0

[a] Tilt and azimuth angles are fixed.

[b] Tilt angle distribution: 38 kW at 21°, 164 kW at 110° and 970 kW at 156°.

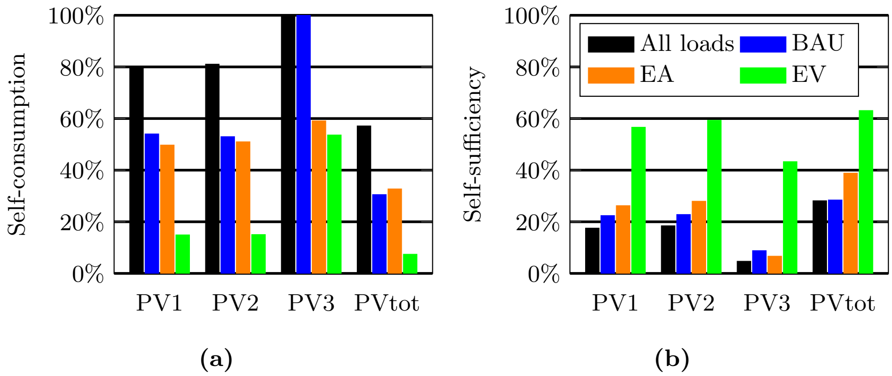

Figure 6.3: PV self-consumption **(a)** and self-sufficiency **(b)** for the PV arrays and load scenarios.

(Fig. 6.3b). Locations 1 and 2 have comparable yields (see Table 6.1), and despite the variation in azimuth angles, the effect on SC and SS is marginal. In this work, PV1 is chosen considering the similar effect on the technical performance as location 2 and the realisation challenges of location 2.

Battery Dispatch Operations

Maximise Self-Consumption

The 'Target Zero' (TZ) algorithm for maximising SC is adopted from [154]; see Fig. D.1. The maximum charge and discharge powers, $\mathrm{P}_{\mathrm{batt}}$, are constrained by the battery's power electronic converter and set to 80% (0.8 C) of the energy capacity. This operation maximises the self-consumed PV and limits grid energy import. The SOC range ($\mathrm{SOC}_{\mathrm{min}}$–$\mathrm{SOC}_{\mathrm{max}}$ is modelled at 90-15% (DOD = 75%). The battery efficiency (η_{batt}) includes the battery converter and cells [Paper I]. The battery voltage (u_{batt}), is adjusted for the next time step using (2.1). Lastly, the battery SOC level, $\mathrm{SOC}(t + \Delta t)$, is adjusted for the next time step.

Peak Shaving

The peak shaving dispatch is done via a rule-based control strategy outlined in Fig. D.2 and limits grid import to a target value set by the monthly peak import. The control uses the available power cap—defined from the difference between the instantaneous net demand and target value—to charge from the grid ($p_{\mathrm{net}}(t)$) to ensure sufficient SOC. Compared to the TZ algorithm, the peak shaving algorithm uses an expanded DoD (85%) by lowering the minimum SOC limit to 5% ($\mathrm{SOC}_{\mathrm{lb}}$). Peak shaving $p_{\mathrm{sh}}(t)$ occurs whenever the instantaneous net demand exceeds the monthly target. After each time step, the target value is compared to the grid import; if the import exceeds the target, a new target value is set. The power tariff is based on monthly performance and reset to zero at the start of the month. The algorithm is modelled with ($\mathrm{S}_{\mathrm{PS}}^{\mathrm{pv}}$) and without PV generation (S_{PS}). The flowchart operation without PV is shown in Fig. D.3.

Multi-Objective Dispatch

The proposed Multi-Objective (MO) dispatch combines maximised SC and peak shaving in a rule-based operation. The operation is described in Fig. D.4. The κ term ensures that:

- grid power is not used to charge the battery entirely (C_3), and
- grid-charged energy is not used for discharge to cover the load demand (C_4).

The MO include a seasonal variation of the minimum SOC level, $soc^{\mathrm{sv}}_{\mathrm{min}}(t)$, outlined in Fig. D.5. Here, $soc^{\mathrm{sv}}_{\mathrm{min}}(t)$ is constrained by $\mathrm{SOC}_{\mathrm{lb}}$ and $\mathrm{SOC}_{\mathrm{max}}$ from Fig. D.4: $\mathrm{SOC}_{\mathrm{lb}} \leq soc^{\mathrm{sv}}_{\mathrm{min}}(t) \leq \mathrm{SOC}_{\mathrm{max}}$. Similar with the peak shaving in Fig. D.2 and D.3, the DoD is set between $\mathrm{SOC}_{\mathrm{lb}}$ and $\mathrm{SOC}_{\mathrm{max}}$. The SOC variation in Fig. D.5 is dictated by the PV export ($pv_{\mathrm{exp}}(t)$) from the previous 24h (dt). If PV is exported, $soc^{\mathrm{sv}}_{\mathrm{min}}(t)$ reduces by δ_{soc}, and if no export is done, $soc^{\mathrm{sv}}_{\mathrm{min}}(t)$ increases by δ_{soc}. This work uses a δ_{soc} of 5%. The minimum SOC level thus has a clear seasonal variation depending on the preceding day's operation and the presence of PV export.

Airport Energy Scenarios

Four main scenarios are modelled and evaluated, with one scenario divided into four sub-scenarios. The scenarios, S_x, are:

- $\mathbf{S_{BAU}}$—represents today's situation and uses the measured load demand from Section 3.5.
- $\mathrm{S}_{\mathrm{BAU}}$ with added EA and EV demands. This case quantifies the added grid stress and energy demand from EA and EV and denotes the reference in the forward-looking scenario; $\mathbf{S_{ref}}$.
- $\mathbf{S_{pv}}$—added PV generation to the reference case, $\mathrm{S}_{\mathrm{ref}}$.
- Added BESS to $\mathrm{S}_{\mathrm{ref}}$ with four battery control algorithms:
  - $\mathbf{S_{TZ}}$—S_{pv} with battery dispatch to maximise self–consumption; see Fig. D.1.
  - $\mathbf{S_{MO}}$—S_{pv} with MO battery dispatch; see Fig. D.4.
  - $\mathbf{S^{pv}_{PS}}$—peak shaving with PV generation; see Fig. D.2.
  - $\mathbf{S_{PS}}$—peak shaving without PV; see Fig. D.3.

The results from the battery scenarios quantify, on the one hand, the effect of BESS and, on the other hand, the effect of the chosen battery dispatch algorithm. Table 6.2 summarises the scenarios.

Battery Sizing and Design

As concluded in previous works, e.g., [91], [105], the effect of increased battery size on the SC diminishes at a certain point, resulting in poor utilisation for

Table 6.2: Scenario matrix for the airport energy infrastructure techno-economic modelling.

	$\mathbf{S}_{\mathrm{BAU}}$	$\mathbf{S}_{\mathrm{ref}}$	$\mathbf{S}_{\mathrm{pv}}$	$\mathbf{S}_{\mathrm{TZ}}$	$\mathbf{S}_{\mathrm{MO}}$	$\mathbf{S}_{\mathrm{PS}}^{\mathrm{pv}}$	$\mathbf{S}_{\mathrm{PS}}$
Reference load demand	✓	✓	✓	✓	✓	✓	✓
Electric Aviation		✓	✓	✓	✓	✓	✓
Electric Vehicle		✓	✓	✓	✓	✓	✓
Solar photovoltaic			✓	✓	✓	✓	
Battery storage				✓[a]	✓[b]	✓[c]	✓[d]

[a] Battery control: Fig. D.1.

[b] Battery control: Fig. D.4–D.5.

[c] Battery control: Fig. D.2.

[d] Battery control: Fig. D.3.

larger sizes. Figure 6.4 shows the SC for S_{TZ} as a function of battery size ($\mathrm{E}_{\mathrm{batt}}$)/RBS. Marginal improvements in SC are observed for RBS>2. Thus,

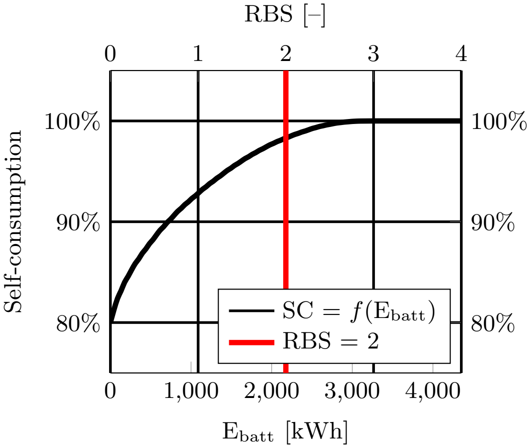

Figure 6.4: Self-consumption as a function of battery size ($\mathrm{E}_{\mathrm{batt}}$)/RBS for S_{TZ}. The vertical line shows the modelled size in this work (2.2 MWh/RBS = 2).

to optimise the BESS for SC and maintaining good utilisation, an RBS = 2 is used in (4.19), resulting in an energy capacity, $\mathrm{E}_{\mathrm{batt}}$, of 2.2 MWh.

The nominal battery voltage (U_{nom}^{batt}) is set to 800 VDC, and the battery are given in Table 6.3 together with the parameterised values [98] for the cycle degradation in (2.14).

Table 6.3: Technical specifications of the modelled battery pack [47] and the numerical values for battery degradation [98].

Parameter	Value	
Q_{cell}	12 Ah	[47]
U_{nom}^{cell}	3.2 V	[47]
U_{nom}^{batt}	800 V	
R	3 mΩ	R per n_{cell} in (2.1)
n_{cell}	250	See (2.5)
$m_{strings}$	227	See (2.3)
B	30,300	
$-E_a$	−31,500	
R_g	8.314	[98]
T	298	
z	0.552	

Economic Evaluation

The investment's economic feasibility is assessed for its PBP considering the annual net electricity bill, the savings from peak power tariffs charges and the monetised battery degradation.

Using the 2018 Nordic electricity spot price ($\mathbb{C}_{NS}$) the hourly price for bought electricity is calculated as

$$\mathbb{C}_{buy}(t) = (\mathbb{C}_{NS}(t) + \mathbb{C}_{tax} + \mathbb{C}_{var} + \mathbb{C}_{cert} + \mathbb{C}_{sur}) \tag{6.2}$$

where $\mathbb{C}_{var}$ is the variable grid charge, $\mathbb{C}_{cert}$ the price of bought electricity certificates, $\mathbb{C}_{sur}$ electricity surcharge, all with a VAT of 25%. The revenue from sold electricity is set equal to the hourly spot price, $\mathbb{C}_{NS}(t)$, as

$$\mathbb{C}_{sell}(t) = \mathbb{C}_{NS}(t) \tag{6.3}$$

where $\mathbb{C}_{NS}(t)$ are retrieved from Nord Pool [162]. Figure 6.5 shows the annual

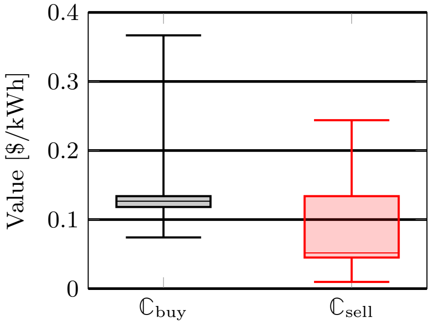

Figure 6.5: Hourly variation of bought ($\mathbb{C}_{\text{buy}}$) and sold ($\mathbb{C}_{\text{sold}}$) electricity in SE3, Sweden from 2018.

hourly variation in bought ($\mathbb{C}_{\text{buy}}$) and sold ($\mathbb{C}_{\text{sell}}$) electricity in 2018 for SE3 in Sweden. The net electricity bill is calculated using (2.16).

In this work, the cash flow from peak power tariff charges is defined relative S_{ref} as

$$\mathbb{C}_{\text{peak}} = \left[\sum_{m=1}^{M} \max(p^m_{\text{S}_{\text{ref}}}) - \sum_{m=1}^{M} \max(p^m_{\text{Sx}})\right] \mathbb{C}_{\text{t}} \tag{6.4}$$

where $\max(p^m_{\text{Sx}})$ is the monthly peak power imports for month m and scenario S_x, and $\mathbb{C}_t$ the peak power tariff ($/kW).

Considering the cash flows (CFs) from the net electricity bill (2.16) and peak power tariff (6.4), the PBP from (2.17) is in this work calculated as,

$$\text{PBP} = \frac{\text{I}_0}{\sum \mathbb{C}_{\text{peak}} + \Delta\mathbb{C}_{\text{net}}(t)} \tag{6.5}$$

where $\Delta\mathbb{C}_{\text{net}}(t)$ is the difference in electricity bill from the reference case (S_{ref}), with positive values for net savings for case S_x. Here, the initial investment, I_{C}, is the sum of the PV array and battery (when relevant) and calculated as

$$\text{I}_{\text{C}}^{\text{PV}} = \text{s}_{\text{pv}} \times \mathbb{C}_{\text{pv}} \tag{6.6}$$

$$\text{I}_{\text{C}}^{\text{batt}} = \text{s}_{\text{batt}} \times \mathbb{C}_{\text{batt}} \tag{6.7}$$

where s_{pv} and s_{batt} are the PV and battery sizes, respectively, and $\mathbb{C}_{\text{pv}}$ and

Table 6.4: Result summary of the power flow analyses for the studied cases.

	$\mathbf{S}_{\mathrm{BAU}}$	$\mathbf{S}_{\mathrm{ref}}$	$\mathbf{S}_{\mathrm{pv}}$	$\mathbf{S}_{\mathrm{TZ}}$	$\mathbf{S}_{\mathrm{MO}}$	$\mathbf{S}_{\mathrm{PS}}^{\mathrm{pv}}$	$\mathbf{S}_{\mathrm{PS}}$
$\mathrm{E}_{\mathrm{load}}$ [MWh/a]	2,629	4,979	4,979	4,979	4,979	4,979	4,979
$\mathrm{E}_{\mathrm{import}}$ [MWh/a]	2,629	4,979	4,108	3,929	4,019	4,107	5,003
Peak import [kW]	749	1766	1707	1707	1192	1192	1233
PV SC [%]	–	–	80.0	98.3	88.6	80.4	–

$\mathbb{C}_{\mathrm{batt}}$ the relative prices (in \$/kW and \$/kWh). The nominal PV and battery prices are set to 0.635 \$/W [163] and 223 \$/kWh [164], respectively.

6.2 Results and Discussion – Airport Microgrid Modelling

Table 6.4 summarises the studied cases' power flow analysis results. The addition of EA and EV ($\mathrm{S}_{\mathrm{ref}}$) almost doubles (+89.4%) the energy demand ($\mathrm{E}_{\mathrm{load}}$) from today's ($\mathrm{S}_{\mathrm{BAU}}$) situation and with an annual peak power increase of more than 1 MW. Without the addition of PV, the increased demand is directly reflected in the import ($\mathrm{E}_{\mathrm{import}}$). Adding PV ($\mathrm{S}_{\mathrm{pv}}$) partly covers the increased import (17.5%) but barely affects the peak demand. Scenario S_{PS} relies solely on battery charging from the grid and thus increases the energy import (+0.5%) but shaves the peak demand (−533 kW). The inclusion of storage and dispatch to maximise SC (S_{TZ}–S_{MO}) partly cover the increased demand (21.5 and 19.4%, respectively). S_{TZ} does little to the peak demand, while S_{MO} gives a significant reduction (−574 kW). $\mathrm{S}_{\mathrm{PS}}^{\mathrm{pv}}$ operation for sole peak shaving barely affects the SC relative to S_{pv} but reduces the peak demand.

Figure 6.6 shows the monthly peak power imports for the scenarios (excluding $\mathrm{S}_{\mathrm{BAU}}$). The addition of PV ($\mathrm{S}_{\mathrm{pv}}$) shave peaks in April–September but is merely a consequence of the coincidence of peak demand and PV generation. The coincidental peak shaving also applies when adding battery storage operating with an SC objective (S_{TZ}). For the peak shaving algorithms (S_{MO}–S_{PS}), the operations result in significantly lower peaks throughout the year. Relative to $\mathrm{S}_{\mathrm{ref}}$, the annually aggregated monthly peak shaving for S_{TZ}–S_{PS} are 0.50, 0.52, 6.20, 6.24, and 6.61 MW/a, respectively.

The proposed MO dispatch performs well compared to $\mathrm{S}_{\mathrm{PS}}^{\mathrm{pv}}$ and S_{PS} except

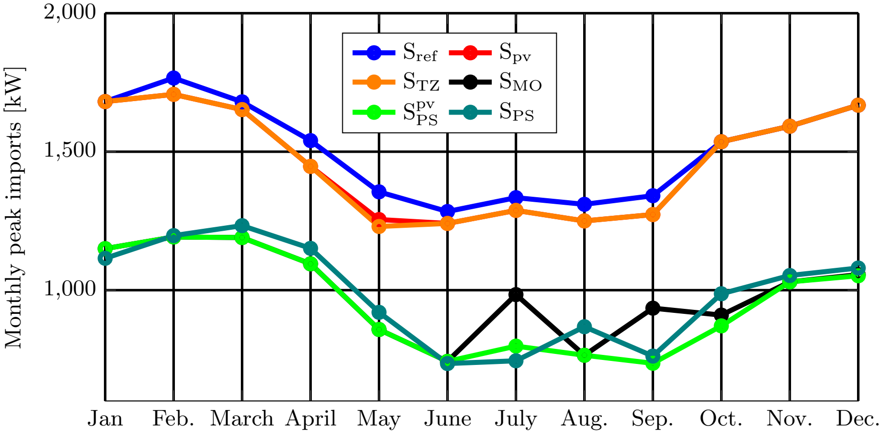

Figure 6.6: Monthly peak power imports per scenario S_{ref}–S_{Dn}

for July and September. The discrepancy in September is explained in Fig. 6.7 showing a comparison between S_{MO} and S_{PS}^{pv} from September 22nd. Figure 6.7a shows the net demand (PV – Load) and the power targets, Fig. 6.7b the charge (positive) and peak shavings (negative), and Fig. 6.7c the battery SOCs. Both manage to shave the initial peak at 10 AM (Fig. 6.7a) and afterwards use the grid to charge until the minimum SOC level (Fig. 6.7c). At 5 PM, another peak occurs and is fully shaved by S_{PS}^{pv} but only partially for S_{MO} (-300 kW), generating a new target value for the latter. The difference in SOC explains the discrepancy in performance (Fig. 6.7c), where S_{PS}^{pv} strives to keep it at maximum (90%) throughout. In contrast, the seasonal variation outlined in Fig. D.5 dictates the minimum level for S_{MO}. As PV export was present in the preceding days, the minimum SOC is low to allow for PV storage. At 6 PM, the grid is again used to charge the batteries, and the difference in the cap—defined by the difference between target and net demand—allows S_{MO} to charge with a higher power; see Fig. 6.7b.

Effect of Battery Dispatch Algorithm on Battery Ageing

Using (2.14) and (2.15), the battery cycle degradation is calculated and shown in Fig. 6.8. As the degradation is a function of energy throughput as per (2.14), the degradation from S_{TZ} is marginal in the period late October to mid-

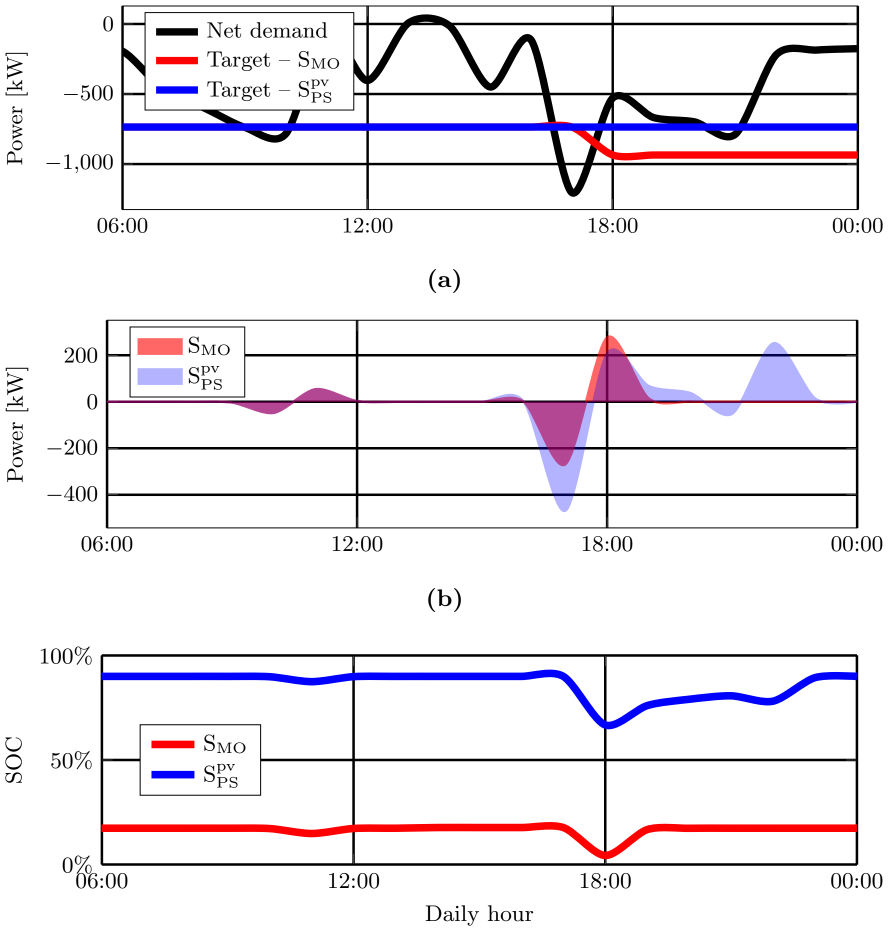

(a)

(b)

(c)

Figure 6.7: Working principle of S_{MO} and S_{PS}^{pv} from September 22nd showing: **(a)** net demand (PV − Load) and power targets, **(b)** battery charge (positive) and peak shaving (negative), and **(c)** battery SOCs.

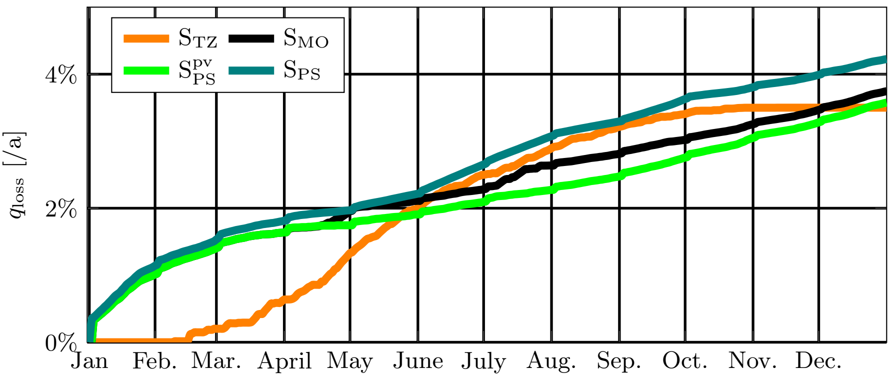

Figure 6.8: Battery cycle degradation per control algorithm.

Table 6.5: Annual BESS degradation, monetised degradation cost and equivalent full cycles (EFCs) for the dispatch algorithms.

	q_{loss} **[%/a]**	$\mathbb{C}_{deg}$ **[\$/a]**	**EFC** [–]
S_{TZ}	3.5	17,010	82.2
S_{MO}	3.7	18,078	81.0
S_{PS}^{pv}	3.6	17,245	74.4
S_{PS}	4.2	20,345	100.4

February, as this control relies on PV surplus for charging. Table 6.5 show the annual degradation (q_{loss}), monetised degradation cost ($\mathbb{C}_{deg}$), and the number of equivalent full cycles (EFCs) for each battery dispatch algorithm. Analysing the trend between EFCs and degradation demonstrates the effect of DoD on degradation. Despite having the second most EFCs, S_{TZ} operation (DoD = 75%) results in the lowest degradation.

Economic Assessment of PV and Battery Investment

Using (6.2)–(6.7) enables an economic assessment of the feasibility of PV and battery investments. As aforementioned, the positive cash flow is calculated relative to S_{ref}. Figure 6.9 shows the PBP for S_{pv}–S_{PS}. For the nominal economic assumptions, the following results are observed:

- For all cases, the reduction in energy import is the primary source of positive cash flow and determined from the hourly electricity pricing and self-consumed PV energy.

- The scenario without battery storage, $\mathrm{S_{pv}}$, has the lowest PBP of 4.8 years, with 98.2% of the savings from SC.

- For the battery scenarios with PV ($\mathrm{S_{TZ}}$–$\mathrm{S_{PS}^{pv}}$), the proposed rule-based multi-objective dispatch ($\mathrm{S_{MO}}$) has the lowest PBP. For the battery cases, the relative monetary savings share from peak shaving are 1.7, 17.8, and 19.6%, respectively.

- As $\mathrm{S_{PS}}$ relies on grid charging of the battery, the electricity bill is higher than for $\mathrm{S_{ref}}$ (+3,404 \$/a), and with monetary savings from peak shaving of 28,704 \$/a. Considering that the degradation cost from Table 6.5 is comparable with the net savings (25,300 \$/a), the investment is questionable from an economic point-of-view.

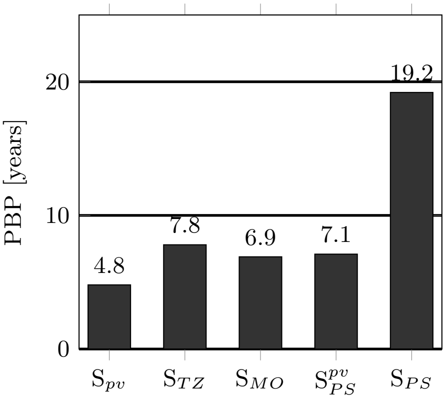

Figure 6.9: Payback period (PBP) for the nominal economic assumptions.

A sensitivity analysis of the PBP is made by varying the battery price, $\mathrm{I_C^{batt}} \in$ 100–300 \$/kWh, and peak tariff, $\mathbb{C}_t \in$ 4.6–46 \$/kW. Figure 6.10 shows the PBP for the nominal battery size, the battery price ranges, and peak power tariffs. For $\mathrm{S_{TZ}}$ (Fig. 6.10a), the battery price has a more significant effect on the PBP than the peak power tariff, seen from the steep PBP slope. This

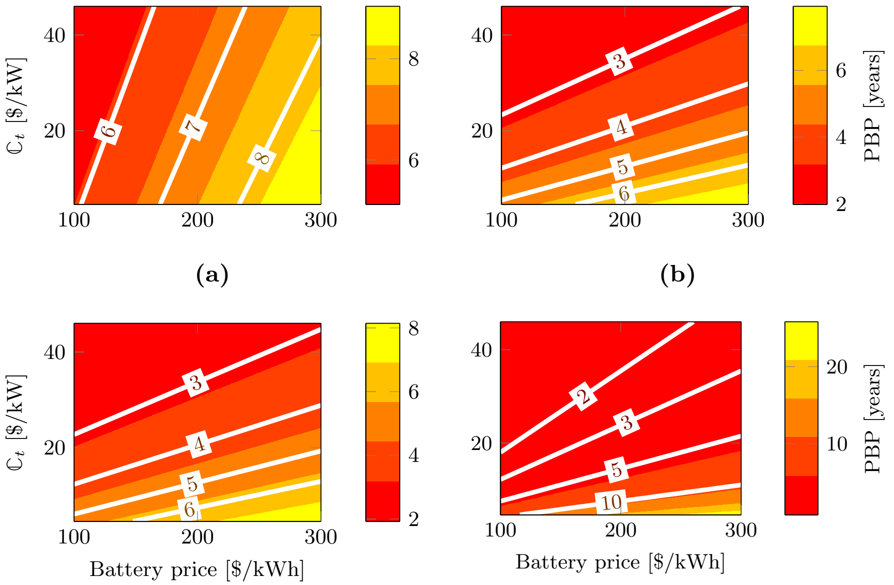

(a) **(b)** **(c)** **(d)**

Figure 6.10: PBP for: **(a)** $\mathrm{S_{TZ}}$, **(b)** $\mathrm{S_{MO}}$, **(c)** $\mathrm{S^{pv}_{PS}}$, and **(d)** $\mathrm{S_{PS}}$, with varying battery prices ($\mathrm{I^{batt}_{C}}$) and peak power tariffs ($\mathbb{C}_t$).

relation comes from the fact above that most of the positive cash flow (98.3%) comes from reduced energy imports. As $\mathrm{S_{MO}}$ and $\mathrm{S^{pv}_{PS}}$ (Fig. 6.10b and 6.10c, respectively) have a larger relative share of peak shaving monetary savings (17.8 and 19.6%, respectively), these two are more sensitive to the peak power tariff as seen from the flatter PBP slope. Without PV, the positive cash flow for $\mathrm{S_{PS}}$ relies entirely on the peak power tariff. With the nominal economic assumptions, the PBP for $\mathrm{S_{PS}}$ is the highest among the battery scenarios; see Fig. 6.9. However, as seen in Fig. 6.10d, the PBP is very sensitive to the peak power tariff. For example, doubling $\mathbb{C}_t$ more than halves the PBP.

6.3 Conclusions – Airport Microgrid Modelling

This work includes a holistic analysis of the airport's energy system in a forward-looking scenario with increased energy and power demands from EA and EV. The analysis examines the roles of PV and BESS from an airport micro grid perspective. The effect of BESS with varying operational objectives is compared and quantified, including the effect on battery degradation.

Adding EA and EV charging increases energy demand and–perhaps more critically–peak power needs. This work demonstrates and quantifies these effects for Visby Airport and the potential gains from on-site PV generation and BESS. Specifically, it examines the PV SC, peak power shaving abilities, and economic feasibility of the studied scenarios.

Substituting the short-haul flights with EA increases the annual load demand by 89.4% and the annual peak power demand by 1 MW. With only PV, the grid demand reduces by 871 MWh. The peak reduction, however, is modest and a consequence of the coincidence of PV output and peak power demand. Including BESS further reduce the grid demand from increased SC, up to 18.3 percentage points for $\mathrm{S_{TZ}}$ compared to scenario $\mathrm{S_{pv}}$. The SC depends on the battery dispatch. For the MO dispatch ($\mathrm{S_{MO}}$), the SC is 88.6%, that is, 9.7 percentage points lower than $\mathrm{S_{TZ}}$. However, $\mathrm{S_{MO}}$ also includes peak-shaving, and the peak reduction is 6.2 MW/a. The MO's peak shaving ability is competitive to sole peak shaving operation with PV; $\mathrm{S_{PS}^{pv}}$ with 6.24 MW/a. The scenario with only the battery operating for peak shaving ($\mathrm{S_{PS}}$) shows that the annual peak reduction is 6.61 MW.

An economic evaluation of the PBP for the PV and battery investments demonstrates the sensitivity of battery price and peak power tariff. For $\mathrm{S_{TZ}}$, financially relying on the reduced demand of bought electricity (through SC), the battery price affects the PBP more. The peak tariff significantly influences the PBP for the other battery operations, especially for $\mathrm{S_{PS}}$, which solely relies on peak shaving.

The proposed rule-based multi-objective battery dispatch ($\mathrm{S_{MO}}$) performs well, considering both SC enhancement and peak shaving. Relative to $\mathrm{S_{pv}}$, it enhances the SC with 8.6 percentage points and sufficiently shaves the power peaks. Given the nominal economic assumptions, this operation has the lowest PBP (6.9 years) among the battery scenarios. The MO operation also reduces the battery's idle period, resulting in an annual degradation (3.7%/a) in the same order of magnitude as the others (3.5–4.2%/a).

CHAPTER 7

PV and Battery System Field Evaluation

Several examples of PR evaluations of PV systems are available in the literature, using any of the three variants introduced in Section 2; see (2.30), (2.33), and (2.35). In [165], a utility-scale PV system is evaluated during eight years of operation for its PR without considering the temperature correction. The works in [166]–[168] acknowledge the temperature-dependency and perform quantified comparisons of the three PR variants to highlight the necessity to account for the temperature-correction. In [166], 22 mono-crystalline PV systems around Italy are evaluated for the PR. Three of the 22 systems are Building–Integrated PV (BIPV), and the other 19 are Building–Applied PV (BAPV). The results confirm that the seasonal bias is less prominent when accounting for temperature-corrections. Avoiding seasonal PR bias is also confirmed in [167] via a simulation comparison of PRs for six locations and PV systems. Despite the previous efforts, an aspect missing in the literature is the empirical evaluation of PRs in a Northern climate and for various cell technologies and installation variants (BAPV and BIPV).

This section is based on Papers VI and VII and evaluates the annual performance of seven PV systems, comparing measured and expected outputs using the PR and the effect of operating module temperature. Eight systems are also examined for annual SC and SS using measured data from operations in Borås, Sweden.

7.1 Methodology

System Designs and Test Site Layout

The systems reflect the residential market in Sweden and cover the variance in buyers' choices regarding PV cell technology and level of roof integration: BIPV (five systems) or BAPV (three systems). The systems also differ in PV technology, i.e., thin film/crystalline, and the type of optimisation, i.e., module or string. During the test, all systems were oriented due south (180 azimuth) with a 45° tilt angle to the horizontal. The latter represents a suitable angle at the site's latitude to maximise the annual yield [126]. Table 7.1 shows the specifications of the systems. The temperature coefficient (δ) refers to the effect on power output. System F was equipped with battery storage and operated against a residential load profile taken from measurements on a Swedish single-family house, with an annual energy demand of 16.9 MWh and a peak power demand of 6 kW.

Table 7.1: Technical specifications of the eight systems used for the performance evaluation.

	System identification							
	A	B	C	D	E	F	G	H
Peak power [Wp]	3080	2975	3900	4080	3245	6200	4800	3289
BI(PV)/BA(PV)	BI/BA	BI	BA	BI	BI	BA	BA	BI
Cell technology[a]	CIGS	CdTe	c-Si	c-Si	c-Si	c-Si	c-Si	CIGS
E_{batt} [kWh]	–	–	–	–	–	5.7	–	–
δ^{b} [%/K]	−0.33	−0.21	−0.37	−0.41	−0.42	–[c]	−0.37	−0.33

[a] c-Si = mono-crystalline silicon.

[b] Refers to the effect on the power output.

[c] Not included in the array analysis [Paper VI].

Data Acquisition

Energy output and irradiance measurements were recorded with a 30-second temporal resolution and ambient and module temperatures with a 60-second

Table 7.2: Measured data quantities.

Data	Measurement	Comment
e^i	System yield	AC quantity after the PV inverter.
t_m^i	Module temperature	1–3 temperature sensors per system on the back side of the module(s).
e_load	Load demand	
e_F	Energy flows	Specifically for system 'F'.
POA	Irradiance	Global in-plane solar irradiance.

resolution. Table 7.2 summarises the measured quantities. The temporal resolution was selected based on related studies of the effect of the temporal resolution on the usage profile and peak powers [105], [169]. In the evaluation, the data was averaged to 10-minute values to match the requirement of Class B data acquisition [113]. Before the evaluation, all data was pre-processed to remove outliers and treated for missing data [170] per available methods [113], [171], [172].

Battery Dispatch – System F

System F's battery dispatch is done to maximise self-consumption, with charging from PV surplus (PV>Load) and discharging during PV deficit (PV<Load). The battery's SOC is kept within 7–97% with a power constraint of 4.6 kW. In Fig. 7.1, the layout of System F is outlined, including measurement points (Wh), load and grid interaction. Generated PV energy, with no charging from the grid, is calculated as

$$p_\mathrm{F}(t) = p_\mathrm{inv}^\mathrm{exp}(t) - p_\mathrm{inv}^\mathrm{imp}(t) \tag{7.1}$$

where $p_\mathrm{inv}^\mathrm{exp}(t)$ and $p_\mathrm{inv}^\mathrm{imp}(t)$ are the power exported and imported to/from the inverter, respectively. In the presence of a battery, the PV output will not follow the conventional output curve since surplus energy is stored in the battery. Using (7.1), the battery and inverter losses are considered. With the definition of PV output from (7.1), the share of self-consumed energy is calculated as

$$\vartheta_\mathrm{SC}^\mathrm{F} = 1 - \int \frac{p_\mathrm{grid}^\mathrm{exp}(t)}{p_\mathrm{F}(t)} dt \tag{7.2}$$

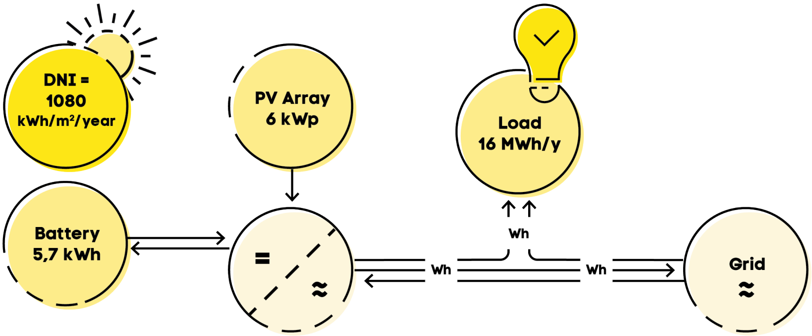

Figure 7.1: System 'F' layout including DC coupled battery storage and measurement points (Wh).

where the ratio $p_{\text{grid}}^{\text{exp}}$ over p_{F} gives the share of generated PV energy exported to the grid. Similarly, the SS is defined by substituting the denominator with the load demand.

As concluded in [104], a decisive factor for the system's self-consumption is the relative size of the PV array to the energy demand, where an increase in size decreases the self-consumption. To quantify the additional gain in SC and SS from the battery storage, the performance of System F is compared to a re-scaled output of System G—having the same cell technology—using their power ratios (see Table 7.1) as

$$p_{\text{G}}^{\text{mod}}(t) = p_{\text{G}}(t)\frac{\text{P}_{\text{rated}}^{\text{F}}}{\text{P}_{\text{rated}}^{\text{G}}} \tag{7.3}$$

where $p_{\text{G}}(t)$ is the output for System G, and $\text{P}_{\text{rated}}^{\text{F}}$ and $\text{P}_{\text{rated}}^{\text{G}}$ the rated powers for Systems F and G, respectively.

7.2 Results and Discussion – Field Evaluation

PV Array Evaluation – Effect of Module Operating Temperature

The systems[1] are evaluated for their PR using the definitions from (2.30), (2.33), and (2.35). The measured power outputs are compensated for the elevated temperature operation, and the annual yields are compared to the measurements to quantify the effect of the module's temperature dependency.

The weekly variation in PR for System A is shown in Fig. 7.2 using (2.30), (2.33), and (2.35). A significant variation is observed during the winter period, despite the effort of reducing the seasonal variations with (2.33) and (2.35). Without the temperature compensation, PR using (2.30) is lower than the others for the periods with high irradiance and higher in the winter. However, the absolute differences between the PRs are within ±0.05 annually. As for the two temperature–compensated PRs, the results from System A show that $\mathrm{PR_{STC}}$ is always higher than $\mathrm{PR_{corr}}$. The reason for this is that the annual weighted module temperature, $\mathrm{T}_m^{\mathrm{avg,A}}$ from (2.36), is 30.8°C and thus less than 25°C as used in (2.34). Table 7.3 shows the weighted module temperatures from (2.37) for all systems, with all exceeding the STC reference temperature

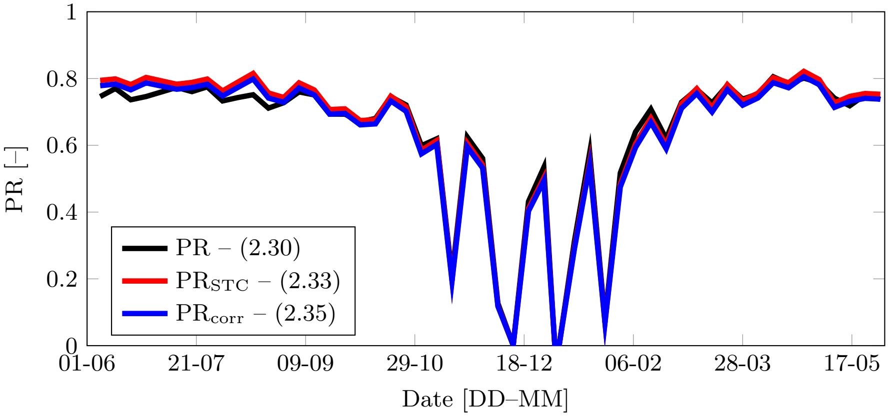

Figure 7.2: Weekly variation in PR for system 'A' using (2.30), (2.33), and (2.35).

---

[1] System F is excluded from the PV array evaluation.

Table 7.3: Calculated irradiance–weighted average annual module temperatures.

	System identification						
	A	B	C	D	E	G	H
$T_m^{avg,i}$	30.6	34.5	26.9	31.0	30.3	26.6	38.3

(25°C). The BIPV systems (B, D, E, and H in Table 7.1) have higher average temperatures than the BAPV systems (C and G) and the hybrid (System A) in-between.

The weekly variation in PR using (2.30), (2.33), and (2.35) for systems B–H (excluding F) are shown in Fig. 7.3. The relative comparison between the PRs follows the trends of System A, with PR being lower during the warmer peri-

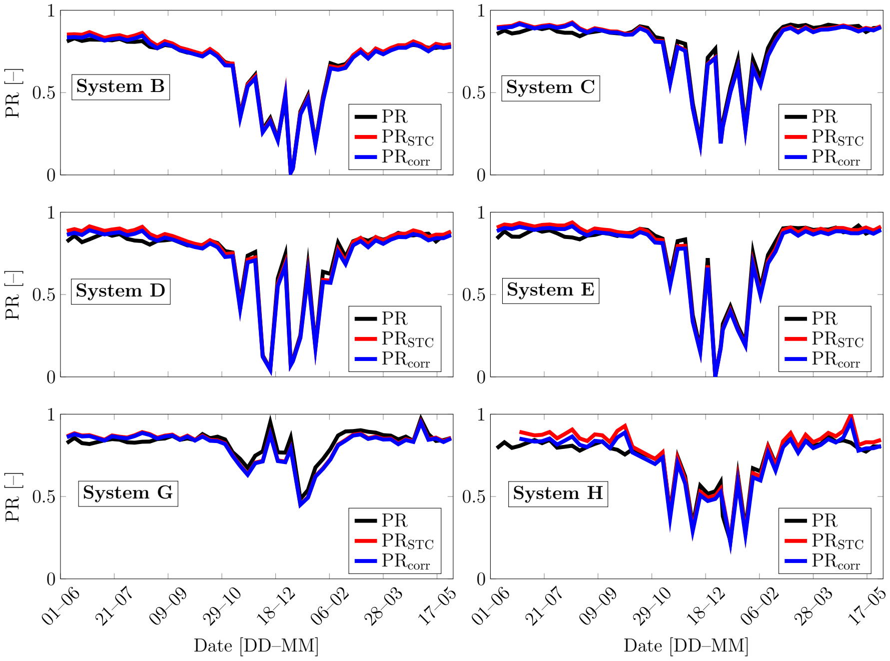

Figure 7.3: Weekly variation in PR for systems B–E and G–H using (2.30), (2.33), and (2.35).

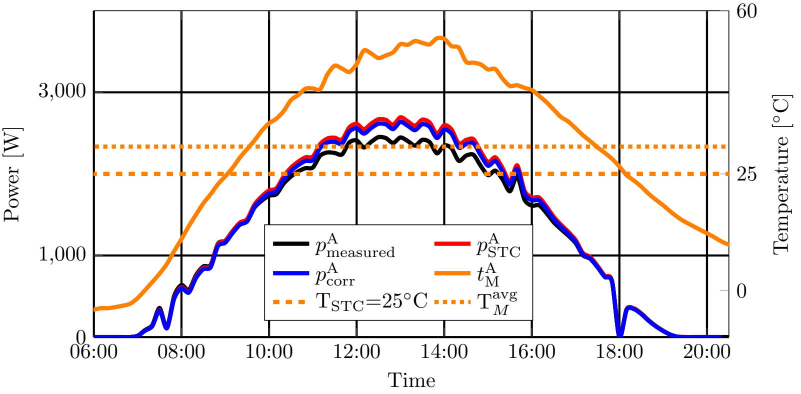

Figure 7.4: Measured and temperature–corrected power outputs for System A.

ods and higher during the winter. A few exceptions are noted, though; one is during December for System B, where the temperature-corrected PRs ($\mathrm{PR}_{\mathrm{STC}}$ and $\mathrm{PR}_{\mathrm{corr}}$) are higher than the non-corrected (PR), caused by missing module temperature data, resulting in an overestimation of the temperature-corrected values. Noticeable are the results for System's C and G where $\mathrm{PR}_{\mathrm{STC}}$ and $\mathrm{PR}_{\mathrm{corr}}$ remain lower than PR after the winter period. The temperature recordings explain the seasonal discrepancy; see Paper VI for further explanations and the recorded module temperature as a function of irradiance[2]. System H's temperature-corrected PRs significantly overestimate the performance during warmer periods caused by the physical location on top of an attic. For System H, the attic temperature affects the measured temperature, resulting in an overestimation of the module temperature and a time shift in the temperature curve due to the building's inertia.

A comparison of the measured and temperature corrected powers from (2.38) and (2.39) is shown in Fig. 7.4 for an arbitrary day's operation with clear-sky. The measured module temperature, $\mathrm{t}^{\mathrm{A}}_{\mathrm{m}}$, is also shown together with the $\mathrm{T}_{\mathrm{STC}}$ (25°C) and the annual irradiance–average temperature, $\mathrm{T}^{\mathrm{avg}}_{\mathrm{m}}$. The measured power is higher in the morning when $\mathrm{t}^{\mathrm{A}}_{\mathrm{m}}$ is lower than the reference temperatures used in (2.34) and (2.36). Around 9 a.m., the module temper-

---

[2] The module temperature is also affected by the ambient temperature and wind speed, but here the analysis is done only on the irradiance level since it is the factor used in the PR equations.

ature exceeds 25°C and $p_{\mathrm{A}}^{\mathrm{STC}}$ becomes higher than $p^{A}_{\mathrm{measured}}$. Similar, when $t^{\mathrm{A}}_{\mathrm{m}} > \mathrm{T}^{\mathrm{avg}}_{\mathrm{m}}$, $p_{\mathrm{A}}^{\mathrm{corr.}}$ exceeds $p^{\mathrm{A}}_{\mathrm{measured}}$. Since $\mathrm{T}^{\mathrm{avg}}_{m} > 25$°C for System A, the STC compensated power using (2.38) will always be higher than the corresponding value from (2.39).

From the temperature–corrected powers using (2.38) and (2.39), the annual energy's are compared with the measurements in Fig. 7.5. The STC compensated energies are the highest due to the previous reasoning of $\mathrm{T}^{\mathrm{avg}}_{m} > 25$ and within 3.2% of the measured (except for System H); see Fig. 7.5b. The large

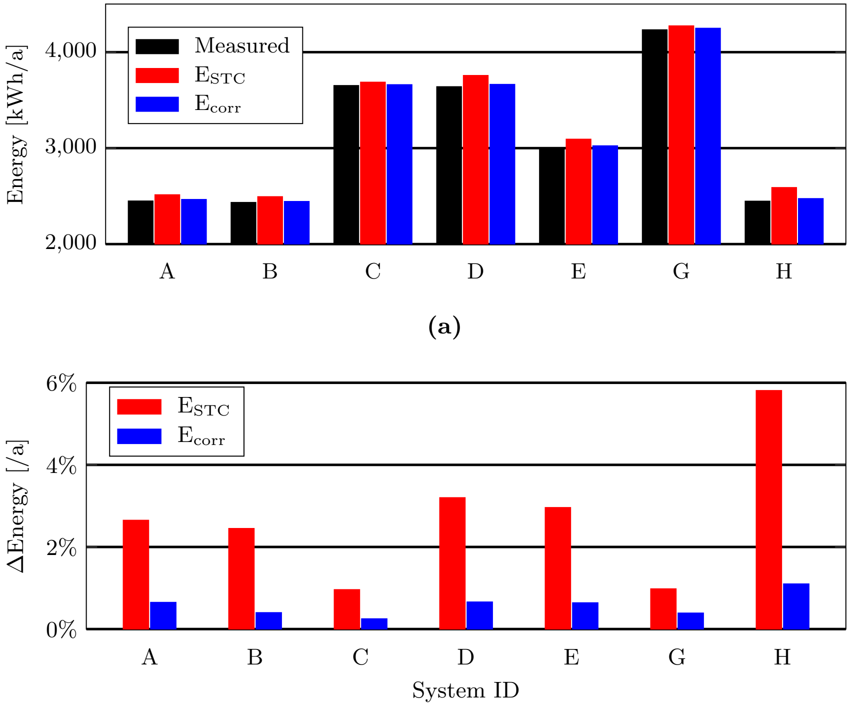

(a)

(b)

Figure 7.5: Annual system performances showing: (**a**) temperature–corrected and measured annual energies and (**b**) deviation relative to the measurements.

discrepancy for System H suggests that the measured module temperature overestimates the actual experienced value. Using the irradiance–averaged temperature correction, the difference is <1% to the measurements. As for E^{i}_{STC}, where the power is corrected to the STC temperature, the temperature compensated output is 1.0–3.2% higher, meaning that the losses due to the elevated temperature are in the same magnitude.

Self-consumption and Self-sufficiency – Performance Correlations and Effect of Battery Storage

As presented in [104], there is a negative correlation between SC and array size. Figure 7.6 shows the resulting yearly SC as a function of array power for the systems without a battery. A prerequisite for the hypothesis in [104] is that the performance of each system is similar. Here, results confirm the negative trend despite the variation in cell technology and the extent of roof integration (BIPV or BAPV).

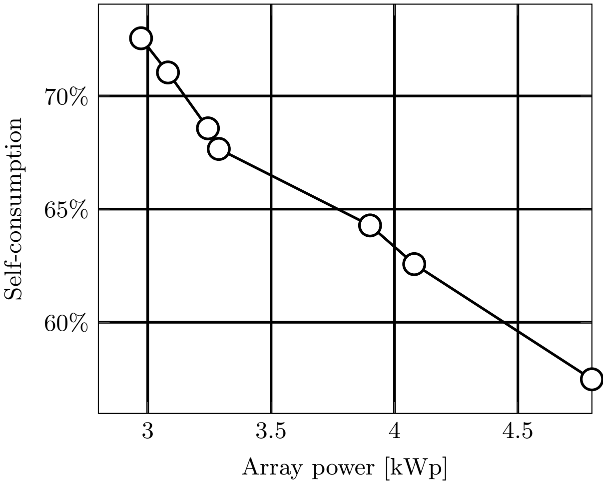

Figure 7.6: Self-consumption as a function of array size for the residential building energy demand.

In Fig. 7.7, the SS as a function of both array power and annual energy output is presented for the systems without batteries. In [104], a positive correlation is observed between SS and array power, which is not confirmed by these results. An explanation for this is that SS uses the absolute self-consumed PV yield normalised by the load demand, unlike the SC that uses the PV yield in the denominator; see (2.22). Comparing the SS with the energy output is more relevant to capturing the effect of the difference in cell technologies and roof integration. The output better reflects the system's performance and presents a more relevant index for this correlation. So, when comparing the SS with energy output, a positive correlation is identified.

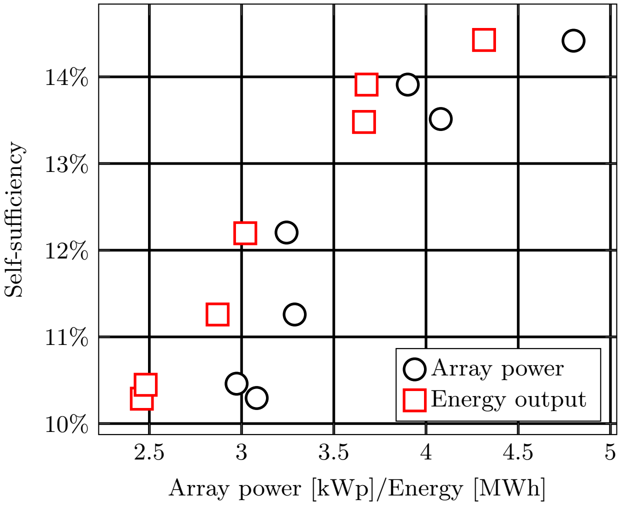

Figure 7.7: Self-sufficiency as a function of array power and energy output for the systems without battery storage.

The resulting SC for the modified output profile from (7.3) is presented together with the calculated SC for System F in Fig. 7.8. The added gains (line and box plot of annual spread) are also included from the inclusion of battery storage, ΔSC. There are no observed gains during the winter period where both systems give 100% SC, and this is due to the low PV outputs relative to the energy demand. Instead, the gain from the battery is observed during periods with PV surplus, with a peak SC gain of 30 percentage points. In absolute terms, the battery increases the self-consumption annually by 738 kWh.

In Fig. 7.9, the effect from the battery is shown for SS using the same

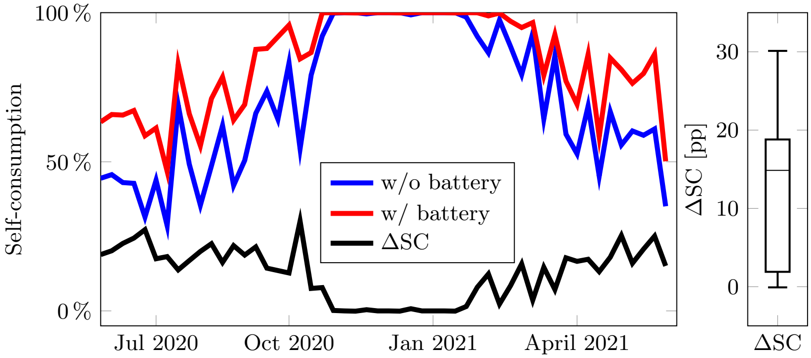

Figure 7.8: Weekly self-consumption with and without battery storage (**left**) and difference (**right**) in percentage points (pp).

methodology with the modified output profile. Peak gains with battery reach above 40 percentage points during the summer. The battery also has a negative effect during the winter—this is also noted for the SC—from standby energy during periods with limited PV surplus. This standby energy is counted as a negative output from the system as per (7.1). Annually, the system without storage has a SC of 50%, while the battery equivalent is at 70%.

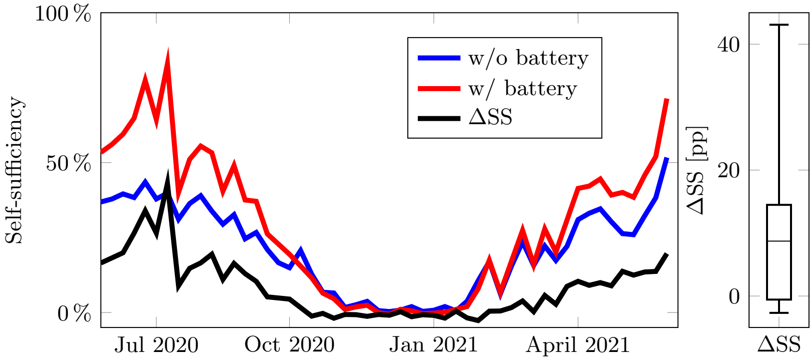

Figure 7.9: Weekly self-sufficiency with and without battery storage (**left**) and difference (**right**) in percentage points (pp).

7.3 Conclusions – Field Evaluation

PV Array Evaluation

Seven systems with varying cell technology and roof–integration were examined for their PR and the effect of module operating temperature. Results show a significant seasonal variation despite the evaluation method, concluding that the low radiation during the winter period makes PR estimations highly uncertain.

The annual effect of elevated module temperature operation on the energy yield shows that the losses are 1% for the BAPV-mounted c-Si technologies. The BIPV mounting of the same technology—with the modules having a higher temperature dependency—adds 2 percentage points to the losses.

Results show that the temperature correction using the annual irradiance–average module temperature coincides well with the yearly PR and annual energy yield measurements.

Self-consumption and Self-sufficiency

The effect of battery storage on SC and SS is examined for eight systems operated with a single-family residential building load profile in Swedish. The results test the hypotheses presented in [104] and examine the correlations between SC, SS, and array size. Results confirm the negative correlation between SC and size despite the variation in system designs. However, there is no clear correlation between SS and size. A correlation is, however, found for SS and annual yield, considering the difference in system design, as the yield better reflects the performance when comparing various designs.

A comparison of two PV arrays shows gains up to 30 and 40 percentage points in SC and SS, respectively, with battery storage. In absolute terms, the battery adds 738 kWh/a in self-consumed PV energy. The weekly performance shows that the effect of the battery, for the chosen battery dispatch algorithm, is negative during the winter. The negative effect on SC in the winter is caused by standby usage, which negatively affects SC and SS. The results highlight the drawback of single-objective battery operation for SC maximisation in a Nordic Climate, resulting in extensive idle periods and negatively affecting battery utilisation and degradation. A suggestion for future works—supported by the findings from this work—is multi-objective battery operation.

CHAPTER 8

SUMMARY OF INCLUDED PAPERS

8.1 Paper I

Patrik Ollas, Torbjörn Thiringer, Mattias Persson, Caroline Markusson
Battery loss prediction using various loss models: A case study for a residential building
Published in Journal of Energy Storage,
vol. 70, no. 15, Oct. 2023.
10.1016/j.est.2023.108048.

This work compares and quantifies the annual losses for three battery system loss representations in a case study for a residential building with solar photovoltaic (PV). Two loss representations consider the varying operating conditions and use the measured performance of battery power electronic converters (PECs) but differ in using either a constant or current-dependent internal battery cell resistance. The third representation is load-independent and uses a (fixed) round trip efficiency. The work uses sub-hourly measurements of the load and PV profiles and includes the results from varying PV and battery size combinations. The results reveal an inadequacy of using a constant battery internal resistance and quantify the annual loss discrepancy to –38.6%, compared to a case with current-dependent internal resistance. The results also show the flaw of modelling the battery system's efficiency with a fixed round trip efficiency, with loss discrepancy variation between –5 to 17% depending on the scenario. Furthermore, the necessity of accounting for the cell's loss is highlighted, and its dependence on converter loading is quantified.

8.2 Paper II

> **Patrik Ollas**, Sara Ghaem Sigarchian, Hampus Alfredsson, Jennifer Leijon, Jessica Santos Döhler, Christoffer Aalhuizen, Torbjörn Thiringer, Karin Thomas
> Evaluating the role of solar photovoltaic and battery storage in supporting electric aviation and vehicle infrastructure at Visby Airport
> *Published in Applied Energy*,
> vol. 352, 2023.
> 10.1016/j.apenergy.2023.121946.

Following the societal electrification trend, airports face an inevitable transition of increased electric demand, driven by electric vehicles (EVs) and the potential rise of electric aviation (EA). For aviation, short-haul flights are first in line for fuel exchange to electrified transportation. This work studies the airport of Visby, Sweden and the effect on the electrical power system from EA and EV charging. It uses the measured airport load demand from one year's operation and simulated EA and EV charging profiles. Solar photovoltaic (PV) and electrical battery energy storage systems (BESS) are modelled to analyse the potential techno-economical gains. The BESS charge and discharge control are modelled in four ways, including a novel multi-objective (MO) dispatch to combine self-consumption (SC) enhancement and peak power shaving. Each model scenario is compared for peak power shaving ability, SC rate and pay-back-period (PBP). The BESS controls are also evaluated for annual degradation and associated cost. The results show that the novel MO dispatch performs well for peak shaving and SC, effectively reducing the BESS's idle periods. The MO dispatch also results in the battery controls' lowest PBP (6.9 years) using the nominal economic parameters. Furthermore, a sensitivity analysis for the PBP shows that the peak power tariff significantly influences the PBP for BESS investment.

8.3 Paper III

Patrik Ollas, Torbjörn Thiringer, Caroline Markusson
Energy Loss Savings Using Direct Current Distribution in a Residential Building with Solar Photovoltaic and Battery Storage
Published in MDPI Energies (2023),
vol. 16, no. 3, pp. 1131.
10.3390/en16031131.

This work presents a comparison of alternating current (AC) and direct current (DC) distribution systems for a residential building equipped with solar photovoltaic (PV) generation and battery storage. Using measured PV and load data from a residential building in Sweden, the study evaluated the annual losses, PV utilization, and energy savings of the two topologies. The analysis considered the load-dependent efficiency characteristics of power electronic converters (PECs) and battery storage to account for variations in operating conditions. The results show that DC distribution, coupled with PV generation and battery storage, offered significant loss savings due to lower conversion losses than the AC case. Assuming fixed efficiency for conversion gave a 34% yearly loss discrepancy compared with the case of implementing load-dependent losses. The results also highlight the effect on annual system losses of adding PV and battery storage of varying sizes. A yearly loss reduction of 15.8% was achieved with DC operation for the studied residential building when adding PV and battery storage. Additionally, the analysis of daily and seasonal variations in performance revealed under what circumstances DC could outperform AC and how the magnitude of the savings could vary with time.

8.4 Paper IV

Patrik Ollas, Torbjörn Thiringer, Huijuan Chen, Caroline Markusson
Increased photovoltaic utilisation from direct current distribution: Quantification of geographical location impact
Published in Progress in Photovoltaics: Research and Applications,

vol. 29, no. 7, pp. 846–856, July 2021.
10.1002/pip.3407.

In this paper, the performance of a direct current (DC) distribution system is modelled for a single-family residential building and compared with a conventional alternating current (AC) system to quantify the potential energy savings and gains in photovoltaic (PV) utilisation. The modelling is made for two different climates to quantify the impact of the geographical location. Results show that the system losses are reduced by 19–46% and the PV utilisation increased by 3.9–7.4% when using a DC distribution system compared to an AC equivalent, resulting in system efficiency gains in the range of 1.3–8.8%. Furthermore, it is shown that the geographical location has some effect on the system's performance and PV utilisation, but most importantly, the grid interaction is paramount for the performance of the DC topology.

8.5 Paper V

Patrik Ollas, Torbjörn Thiringer, Mattias Persson
Enhanced DC building distribution performance using a modular grid-tied converter design
Submitted manuscript.

With the market expansion of solar photovoltaic (PV) and stationary battery systems, DC distribution has gained momentum, potentially reducing internal building conversion losses. This article presents a demonstration and quantification of energy loss savings in a DC-powered home using a modular converter for the grid connection. Two methods, utilising software and hardware configurations, are showcased to improve DC distribution: (i) a novel rule-based battery dual-objective operation (DOO) and (ii) a modular Master–Slave design of the grid-tied converter (GC). Both methods use the GC's load-dependent efficiency characteristic, eliminating partial-load GC operation and enhancing energy efficiency. The work uses measured PV and load demand to evaluate the techno-economic performance of the methods compared to AC and DC reference cases. Furthermore, the techno-economic implications of battery degradation are analysed. The results show that the DOO eliminates GC partial-load operation at the cost of increased battery usage, resulting in marginal net savings. In contrast, the modular converter design significantly reduces losses: -157 kWh/a (-31%) and -121 kWh/a (-26%), respectively, relative to the DC and AC references. The Lifetime Operating Cost (LOC) comparison shows savings from DC in the range of \$80 to \$399 compared to AC.

8.6 Paper VI

Patrik Ollas, Jon Persson and Peter Kovacs
Technical Performance Evaluation of BIPV and BAPV Systems
38th European Photovoltaic Solar Energy Conference and Exhibition, 2021
10.4229/EUPVSEC20212021-5DO.3.5.

This work evaluates seven residential solar photovoltaic systems for their technical performance under a full year's operation in Sweden. The system technologies are selected to reflect available products on the Swedish market and include three building-attached (BAPV) and five building-integrated (BIPV) systems. The evaluation is done for the Performance Ratio (PR) and temperature-corrected PR, and the results highlight the seasonal variation and effect of the modules' temperature dependency. The annual losses due to operation at elevated temperatures are also quantified for each system, using a temperature-compensated power output, and the results show that the losses are 1–3.2% on the measured yield, depending on the PV technology and extent of roof integration (BIPV or BAPV).

8.7 Paper VII

Patrik Ollas, Jon Persson and Peter Kovacs
Effect of Energy Storage on Self-Consumption and Self-Sufficiency: A Field Study in a Nordic Climate
38th European Photovoltaic Solar Energy Conference and Exhibition, 2021
10.4229/EUPVSEC20212021-6BV.5.16.

This paper examines the variation in self-consumption (SC) and self-sufficiency (SS) for eight residential-size solar photovoltaic systems under Nordic climate conditions. The work uses measured photovoltaic array performances with a 30-second temporal resolution and is evaluated for an entire year's operation. One of the systems is operated with battery storage to examine the effect on the system's SC and SS, where the simulated load profile is taken from a single-family residential building in Sweden. The results show a consistent negative correlation between array size and SC. The relation between array size and SS is more sensitive and affected by the mix of PV technologies represented in the test. Adding battery storage increases the weekly SC by 0–30 percentage points. Furthermore, the variation of SC and SS follows the seasonal variation in solar resource and load size and illustrates the battery's eventual redundancy in the winter when the battery's objective function is to maximise SC.

CHAPTER 9

CONCLUDING REMARKS AND FUTURE WORK

Conclusions

This thesis assesses the viability of internal direct current (DC) building distribution, solar photovoltaic (PV) generation and stationary battery storage. The included papers and the results examine these viabilities for various building types and scenarios.

First and foremost, ignoring the load-dependant characteristics of the power electronic converter (PEC) efficiencies or the battery cell's internal resistance when studying energy losses in buildings is proven erroneous in Papers III and IV and for the battery system in Paper I. For the comparison of AC and DC distribution for a single-family building, the use of a constant efficiency for the grid-tied converter (GC) results in an underestimation of the losses by 34% (63 kWh/a) and 29% (110 kWh/a). Using the battery round trip approximation for the battery system losses results in annual loss discrepancies between -5% to 29%, depending on the scenario.

Secondly, the techno-economic potential for DC building distribution is proven dependent on the building type, PV and load correlation, the PEC design, and the inclusion of DC sources (PV and battery storage). From the modelling of the single-family building in Borås and considering the PEC's load-dependent characteristics, the results show that the inclusion of PV alone is not enough to achieve loss savings with DC operation; +6.7% and +5.4% for a PV-to-load share of 50% and 100%, respectively. However, adding battery storage, DC operation reduces the losses for the same case by −15.8% to −17.7%, depending on the PV and battery sizing. For the three office buildings in Gothenburg, Denver and Phoenix, the results confirm the positive effect of PV and load correlation on DC loss savings, where the two latter cases show savings from the mere inclusion of PV (without storage). At the same time, a battery is needed in Gothenburg to achieve savings. The parametric sweep of PV and battery sizes highlights the effect of GC sizing, where a GC that is too large results in more frequent partial-load operation with higher relative losses. The parametric sweep shows that peak savings for the three locations occur for the largest battery size and a PV-to-load share of 50% in Gothenburg (−24%), 75% in Denver (−36%), and 100% in Phoenix (−39%).

Thirdly, a modular GC design with a smaller and larger converter operated in parallel is presented to reduce the effect of the GC losses on the DC performance. For an optimal 15/85% size configuration, DC operation results in a 26% loss reduction compared to AC for the single-family residential building. The same GC size distribution for an office building results in more than 40% (−13 MWh/a) loss reduction. The GC design primarily enhances the performance for scenarios with smaller or no battery storage, reducing the effect of partial load GC operation. For Gothenburg—with the most significant relative gains from GC design operation—and the scenarios without battery storage, the GC design enables loss savings relative to AC even without battery storage, in contrast to the reference operation with $\chi = 0\%$.

Moreover, the battery representation from Paper I—derived from experimental measurements on a cell—has proven accurate in modelling the current–voltage characteristics, with an RMSE<7 mV relative to the measurements. Significant loss discrepancies are shown for the other two models (round trip efficiency and fixed internal resistance, $\mathrm{R_0}$) for annual battery system losses: −5 to 29% for the round trip approximation and −21 to −39% using $\mathrm{R_0}$. The results also prove that cell losses cannot be ignored and that its effect is enhanced with increased converter loading. The cells' loss contribution ranges between 22% and 45% depending on the studied scenarios.

Furthermore, the electrification of the transport sector is a significant challenge for the electric grid. Paper II examines this challenge for a domestic airport in Sweden and a forward-looking scenario with electric aviation (EA) and electric vehicles (EVs), presenting significant increases in energy (+89.4%) and power demands (+1 MW) compared to today's situation. Including PV reduces energy grid imports (−871 MWh/a) from self-consumption (SC) while marginally affecting the peak power imports. In contrast, including battery storage—depending on the operation algorithm—affects both the grid import demand and peak powers. The PV and battery investments' payback period (PBP) is promising, depending on the economic assumptions of battery investment price and peak power tariff. A sensitivity analysis shows the effect on PBP depending on the battery operation algorithm. The techno-economic performance of the proposed novel battery operation is proven feasible, with a PBP of 6.9 years for the nominal economic assumptions.

Lastly, in Paper VII, the effect on SC and self-sufficiency from the battery showed gains up to 30 to 40 percentage points (up to 738 kWh/a). However, most importantly, the empirical evaluation of single-objective battery operation for SC maximisation in a Nordic climate showed poor battery utilisation during periods of low irradiance and highlighted the necessity for multi-objective battery operation for optimal usage.

Finally, building energy modelling is complex and requires accurate models of the components for representative performance results. This work compares and quantifies the erroneous use of simple assumptions compared to empirically derived models. On top of that, the effect of component sizing is examined, and its effects are highlighted. To conclude, a recommendation from the author when modelling the performance of building energy systems is to use PEC and battery models that account for the load-dependant characteristics and to perform a parametric sweep for crucial component sizes. Abiding by this will get you one step further towards accurately modelling optimal building energy performance.

Future Work

Research efforts are identified to deepen the analysis based on the works in this thesis. Here are a few suggestions:

- Previous efforts on techno-economic studies on AC and DC distribution are typically based on single or homogeneous load profiles, e.g., [14], [43], [52], [53]. Analysis of more extensive and heterogeneous data sets is required to deepen the understanding of DC viability, preferably including various building types and statistical examinations of decisive factors. Furthermore, such a study could be combined with a more thorough design of the PV arrays to enhance the load correlation [173].

- Electric Vehicles (EVs) with vehicle–to–home (V2H) abilities with internal DC distribution is an interesting case to investigate further. Unlocking the EV potential for external services offers great potential, especially for building DC distribution as an inherited DC source. Research questions include: How is the loss savings potential affected by V2H, and to what extent could it replace or complement stationary storage?

- As concluded in Paper II, the proposed multi-objective (MO) battery dispatch could be further examined. One suggestion is to perform a sensitivity analysis on the δ_{soc} ($\pm 5\%$ in Paper II). The dispatch shall also be applied to other cases to test its viability. Currently, the MO dispatch combines SC maximisation and peak power shaving. An extension of this includes other combinations of battery services that could be applied, e.g., grid services and market arbitrage.

- This work examines the viability of PV, battery storage and DC distribution from a building's perspective. For a continuation, the system boundary could be expanded to include the external grid and the interplay between buildings. The consequence of PV and battery storage on the grid is well-known, but the aspect of DC could be explored further considering power quality.

- This work briefly touches upon the economic aspect of building DC distribution. Although considering the uncertainties in DC investment prices [144], the economic viability of DC operation could be further investigated.

APPENDIX A

Taxonomy Table of Previous Works on DC Building Distribution

Table A.1 shows a taxonomy table of related journal publications on technical comparisons of AC and DC building distribution, including the works in Papers III–V (PIII–V) and the unpublished work for the office building. Each work is evaluated for case studied (Residential or Commercial building), data profiles (Synthetic or Measured), consideration of PEC and battery load-dependant (f(s)) or Fixed efficiencies, the inclusion of DC sources and studied time period (Day(s) or Annual operation).

Table A.1: Taxonomy table of publications on AC vs. DC in buildings; methods, data profiles, DC sources included, data period analysed and presented energy savings.

		PEC eff.		**Data**		**BESS eff.**		**Sources**		**Period**		**Savings⋆**
Ref.	Case	*f*(s)	Fixed	Synth.	Meas.	*f*(s)	Fixed	PV	Battery	Day(s)	Ann.	%
[55]	Res.	(✓)[a]			✓		✓	✓	✓		✓	9–20[b]
[42]	Res.		✓[c]	✓			✓	✓	✓		✓	5[d]
[43]	Res.		✓	✓		–	–	✓			✓[e]	4–10%[f]
[49]	Res.		✓	✓		–	–				✓[e]	−6/−2%
[50]	Res.	(✓)[g]		✓		✓[g]		✓	✓	✓		_[h]
[11]	Com.	(✓)[g]		✓			✓	✓	✓		✓	1–18%[i]
[48]	Res.	✓		✓		–	–	✓		✓		_[h]
[53]	Com.	✓			✓		✓	✓	✓		✓	5%
[14]	Com.	(✓)[j]		✓		✓		✓	✓		✓	2–5%
[52]	Res.		(✓)[k]		✓	–	–	✓		✓		_[h]
PIII	Res.	✓			✓	✓		✓	✓		✓	Section 4
PIV	Res.	✓		✓		✓		✓	✓		✓	
PV	Res.	✓			✓	✓		✓	✓		✓	
Unpub.	Com.	✓		✓		✓		✓	✓		✓	

⋆ Savings are either reported as energy savings in [42], [53], [55], or as system efficiency savings [11], [14], [43], [48]–[50]. For a definition of the system efficiency, see [11].

[a] Presents max and min values for the converters and claims that the same efficiency degradation is used for the AC/DC and DC/DC PECs. However, whether the loss analysis considers the full efficiency range is unclear.

[b] The savings increase to 14–25% with battery storage.

[c] Acknowledge the efficiency degradation at part-load but only consider a single efficiency point below 20% of full-load operation.

[d] The savings increase to 14% with battery storage.

[e] Not explicitly mentioned, but it seems that the analysis is done for annual operation.

[f] The savings depend on the DC distribution voltage (48–380 VDC) and wire gauge.

[g] Presents efficiency curves for the PECs but only down to 10% part load. Thus, it is unclear how the efficiency is treated in loading cases below 10%.

[h] Only compared for a single day's operation and thus not relevant to present the savings.

[i] The span represents the result from parametric simulations with varying PV and battery sizes for a small and medium zero net energy office building.

[j] Presents PEC efficiency curves down to 20% part-load operation, but how the efficiency is treated below that loading is unclear.

[k] It remains unclear how the converter losses are treated.

APPENDIX B

Complementary Tables and Figures – AC vs DC Distribution Comparison

B.1 Single-family buildings – Borås and Phoenix

Tables B.1 and B.2 give numerical summaries of the results for the simulated single-family residential buildings in Borås and Phoenix with AC and DC distribution and the two PV and battery systems.

Table B.1: Numerical summary of the results for **Borås, Sweden**, with AC and DC distribution and the two modelled PV and battery systems.

	3.6 kWp/0 kWh			3.6 kWp/7.5 kWh		
	AC	**DC_1**	**Diff.**[a] [%]	**AC**	**DC_1**	**Diff.**[a] [%]
Losses [kWh/a]	671	544	−**19.0**	831	556	−**33.1**
Grid-tied converter	0	353		0	288	
Battery converter	0	0		125	39	
PV converter	235	77		235	77	
Battery cells	0	0		35	38	
Rect. (AC/DC)	322	0		322	0	
Conversion (DC/DC)	114	114		114	114	
κ_{system} [%]	93.8	94.9	+**1.2**	92.3	94.8	+**2.7**
κ_{pv} [%]	94.0	98.0	+**4.3**	89.9	96.1	+**6.9**

[a] 'Diff.' refers to the difference relative AC performance.

Table B.2: Numerical summary of the results for **Phoenix, USA**, with AC and DC distribution and the two modelled PV and battery systems.

	3.6 kWp/0 kWh			3.6 kWp/7.5 kWh		
	AC	**DC_1**	**Diff.**[a] [%]	**AC**	**DC_1**	**Diff.**[a] [%]
Losses [kWh/a]	908	649	−**28.5**	1222	689	−**43.6**
Grid-tied converter	0	384		0	267	
Battery converter	0	0		243	77	
PV converter	436	151		436	151	
Battery cells	0	0		71	80	
Rect. (AC/DC)	358	0		358	0	
Conversion (DC/DC)	114	114		114	114	
κ_{system} [%]	92.4	94.6	+**2.4**	89.8	94.2	+**4.9**
κ_{pv} [%]	94.2	98.0	+**4.0**	90.1	95.9	+**6.4**

[a] 'Diff.' refers to the difference relative AC performance.

B.2 Office Buildings – Gothenburg, Denver and Phoenix

Figure B.1 shows the absolute annual loss savings from DC distribution in an office building located in Gothenburg (top), Denver (middle), and Phoenix (bottom). The results are shown for RBS (0–1.5 kWh/kWp) and PV-to-load share (0–150%).

Figures B.2 and B.3 show the relative and absolute effect on the DC performance from modular GG design and for varying size distribution (χ) and RBS. The comparison is for a PV-to-load share of 100%. For the same PV-to-load share, the absolute savings for modular GC design compared to AC and varying RBS is shown in Fig. B.4.

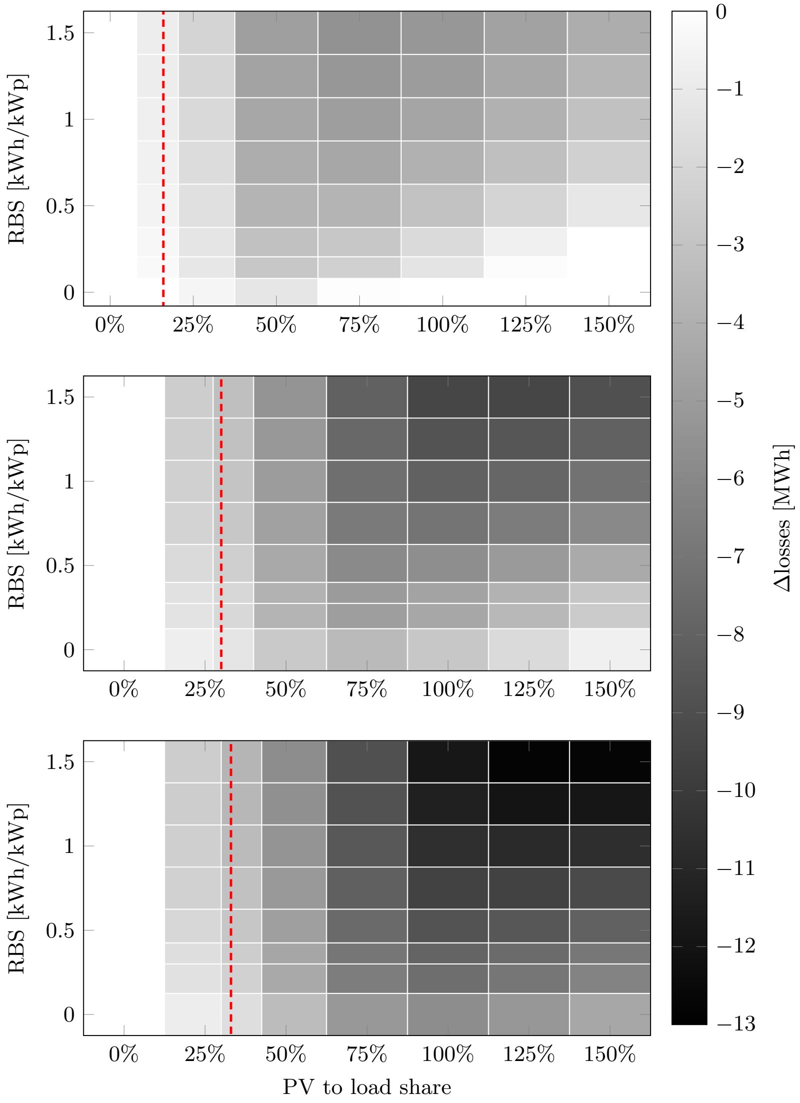

Figure B.1: Absolute effect on annual losses (DC – AC) from varying PV and battery sizes for: Gothenburg (**top**), Denver (**middle**), and Phoenix (**bottom**). The dashed lines are the reference PV sizes from Table 3.4.

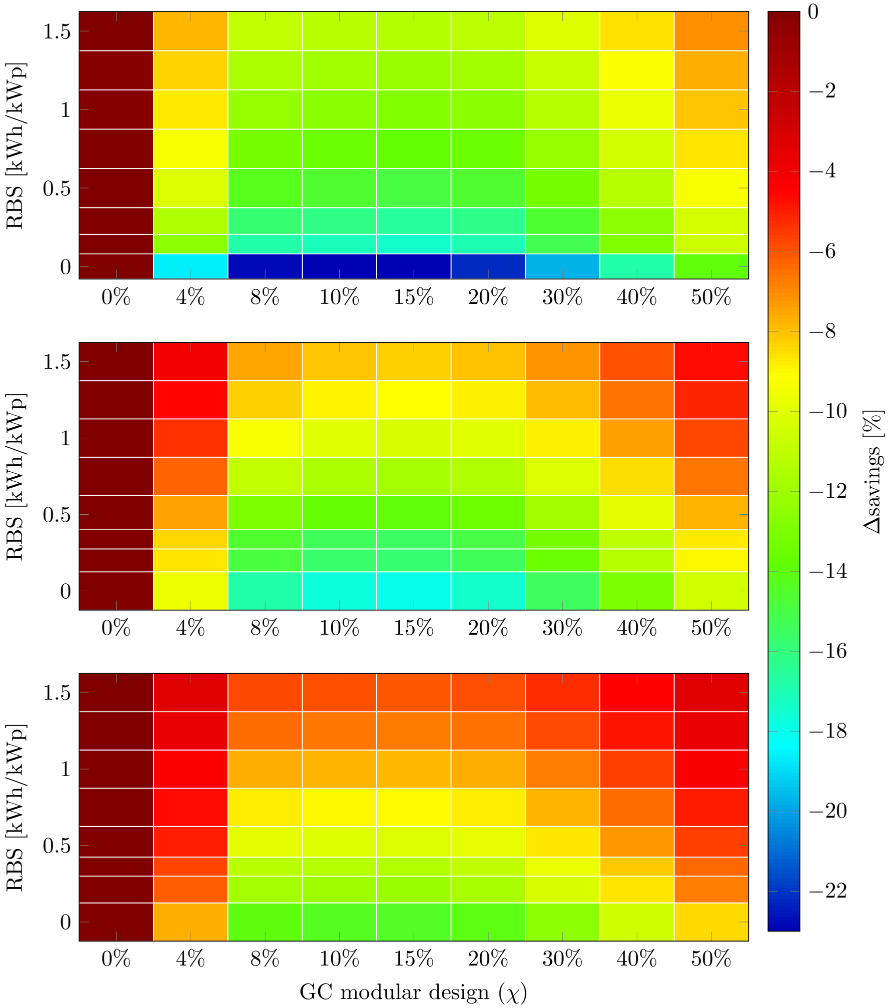

Figure B.2: Relative effect on DC loss savings from modular GC operation with varying design (χ) and battery size for Gothenburg (**top**), Denver (**middle**), and Phoenix (**bottom**). The PV-to-load share is 100%.

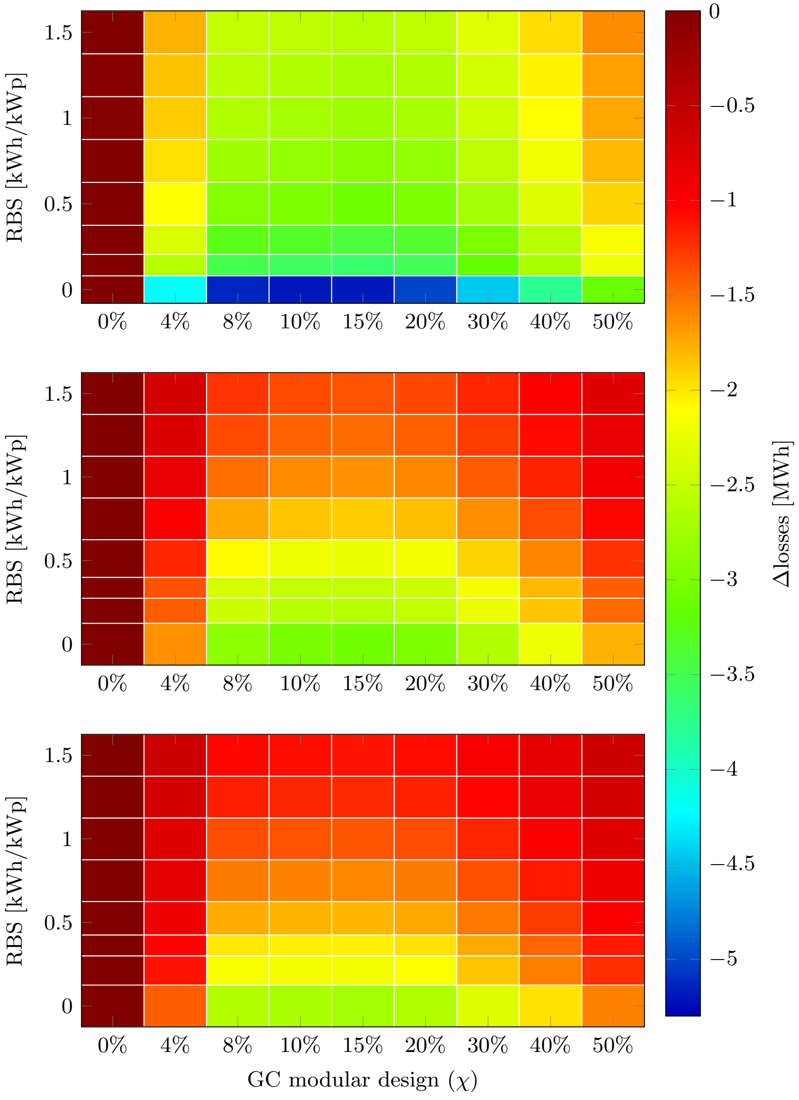

Figure B.3: Absolute effect on DC performance from modular GC design and varying size distribution (χ) and battery storage for Gothenburg (**top**), Denver (**middle**), and Phoenix (**bottom**). The PV-to-load share is 100%.

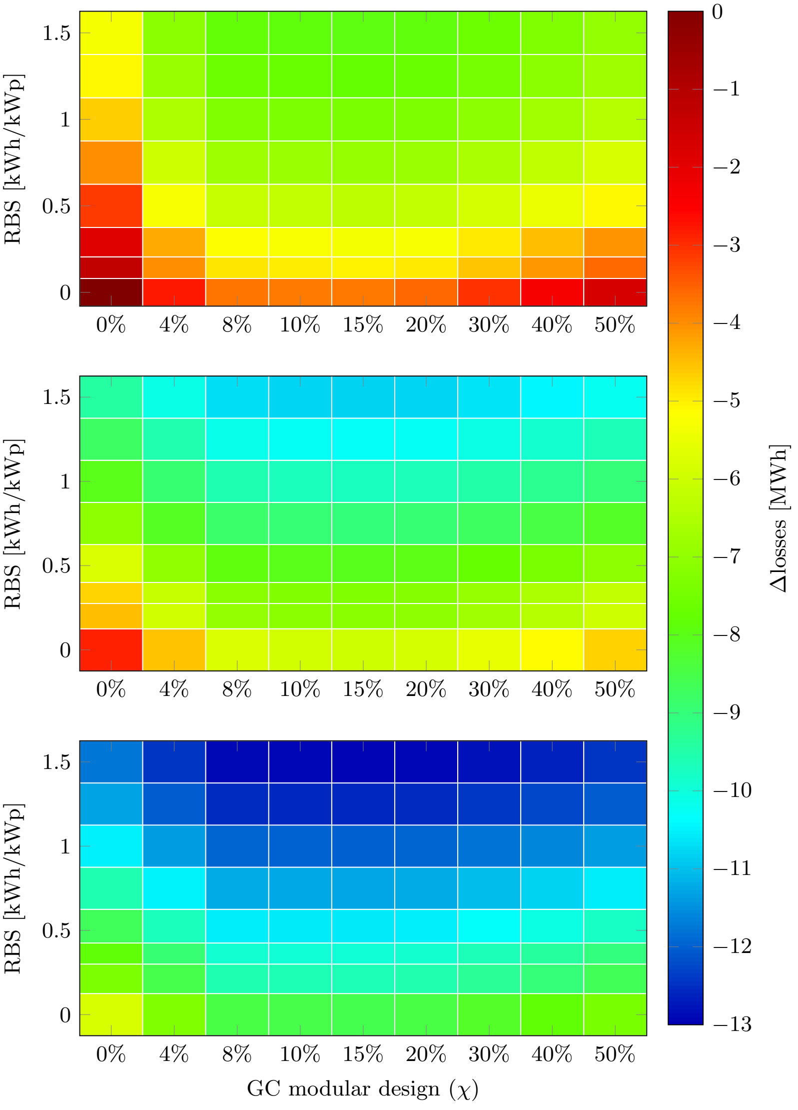

Figure B.4: Absolute loss savings from modular DC operation versus AC with varying GC load distribution (χ) and battery size for Gothenburg (**top**), Denver (**middle**), and Phoenix (**bottom**).

APPENDIX C

Converter Characteristics and Numerical Values for Curve-Fits

C.1 Modelled converters

Table C.1 shows the technical specifications of the measured DC converters, Fig. C.1 the measurements (markers) and curve-fits, and Table C.2 the numerical values for the curve-fitted efficiency characteristics used in (3.2).

C.2 Internal Cell Resistance as a Function of Current

Table C.3 shows the numerical values for the curve-fitted internal battery cell resistance as a function of current used in (5.2).

Table C.1: Technical specifications of the measured power electronic converters.

Converter	Quantity	Unit	Value
Bi-directional (AC/DC)	P_{rated}	kVA	14
	$U^{\mathrm{AC}}_{\mathrm{RMS}}$	VAC	400
	$I^{\mathrm{DC}}_{\max}$	A	±20
	U_{DC}	VDC	±380
Bi-directional (DC/DC)	P_{rated}	kVA	6
	U_{batt}	VDC	120–720
	I_{batt}	A	±10
	U_{DC}	VDC	740–780[a]
	I_{DC}	A	9
Unidirectional (DC/DC)	P_{rated}	kVA	6
	$U^{\mathrm{OCV}}_{\max}$	VDC	1000
	$I^{\mathrm{SC}}_{\max}$	A	9.5
	U_{MPP}	VDC	120–720
	U_{DC}	VDC	740–780[a]
	$I^{\mathrm{DC}}_{\max}$	A	9

[a] Nominal voltage: 760 VDC.

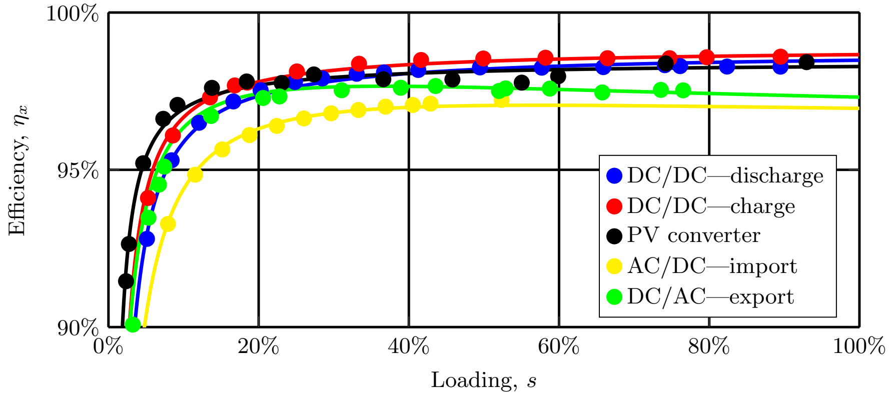

Figure C.1: Measured converter efficiency (markers) and curve fits (solid lines).

Table C.2: Numerical values for the modelled converters in (3.2).

	DC/DC$_{\text{ch.}}$	**DC/DC**$_{\text{dis.}}$	**PV**$_{\text{inv}}$	**AC/DC**	**DC/AC**
k_1	0.9887	0.9876	0.9843	0.9617	0.9621
k_2	4.8×10^{-7}	4.2×10^{-6}	7.3×10^{-6}	0.607	0.662
k_3	-3.1×10^{-9}	-4.6×10^{-10}	-9.9×10^{-11}	-4.7×10^{-7}	-4.3×10^{-8}
m_1	0.0021	0.0028	0.0015	0.615	0.667
m_2	1.78×10^{-5}	2.07×10^{-5}	4.6×10^{-6}	0.003	0.002
R^2	1.000	1.000	0.999	0.999	1.000
RMSE	0.0019	0.0014	0.0024	0.0019	0.0008

Table C.3: Numerical values from the curve fit in (5.2) for the internal resistance variation in the battery cell as a function of current.

Coefficient	**Value**
p_1	-0.4651×10^{-3}
p_2	17.96×10^{-3}
p_3	23.02×10^{-3}
q_1	15.79×10^{-3}
R^2	1
RMSE	0.5171×10^{-3}

APPENDIX D

Battery Dispatch Flow-Charts

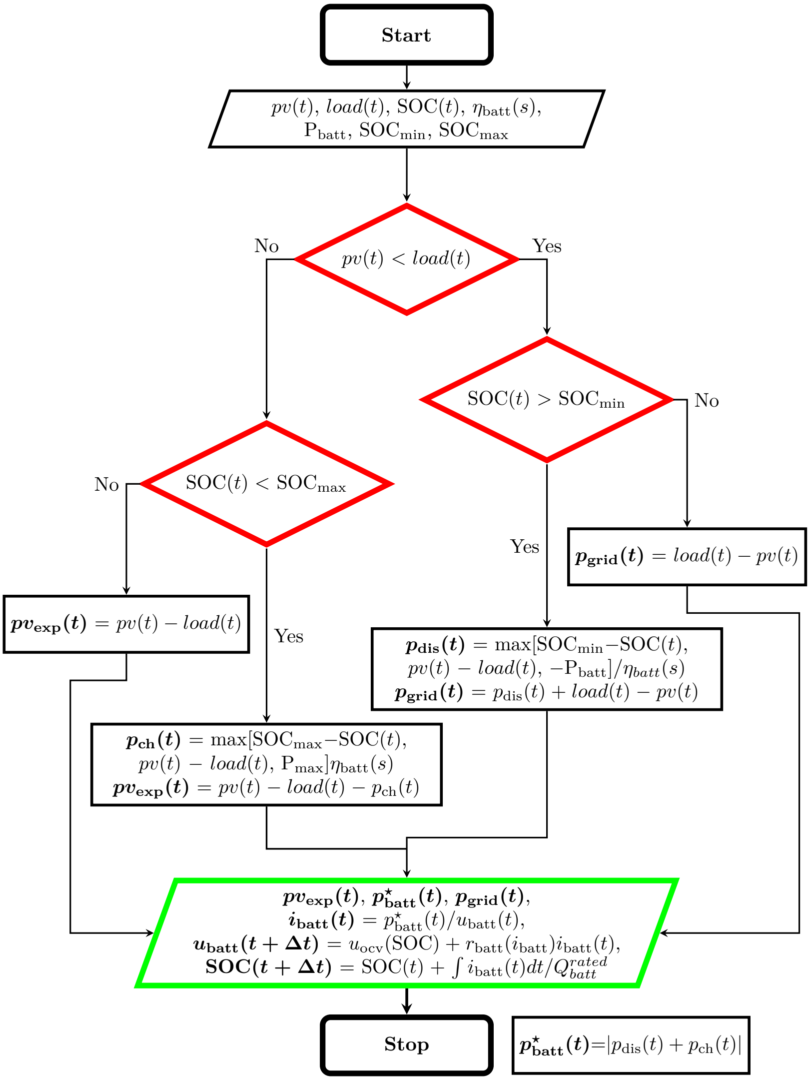

Figure D.1: Flow chart of battery charge and discharge control to maximise self-consumption.

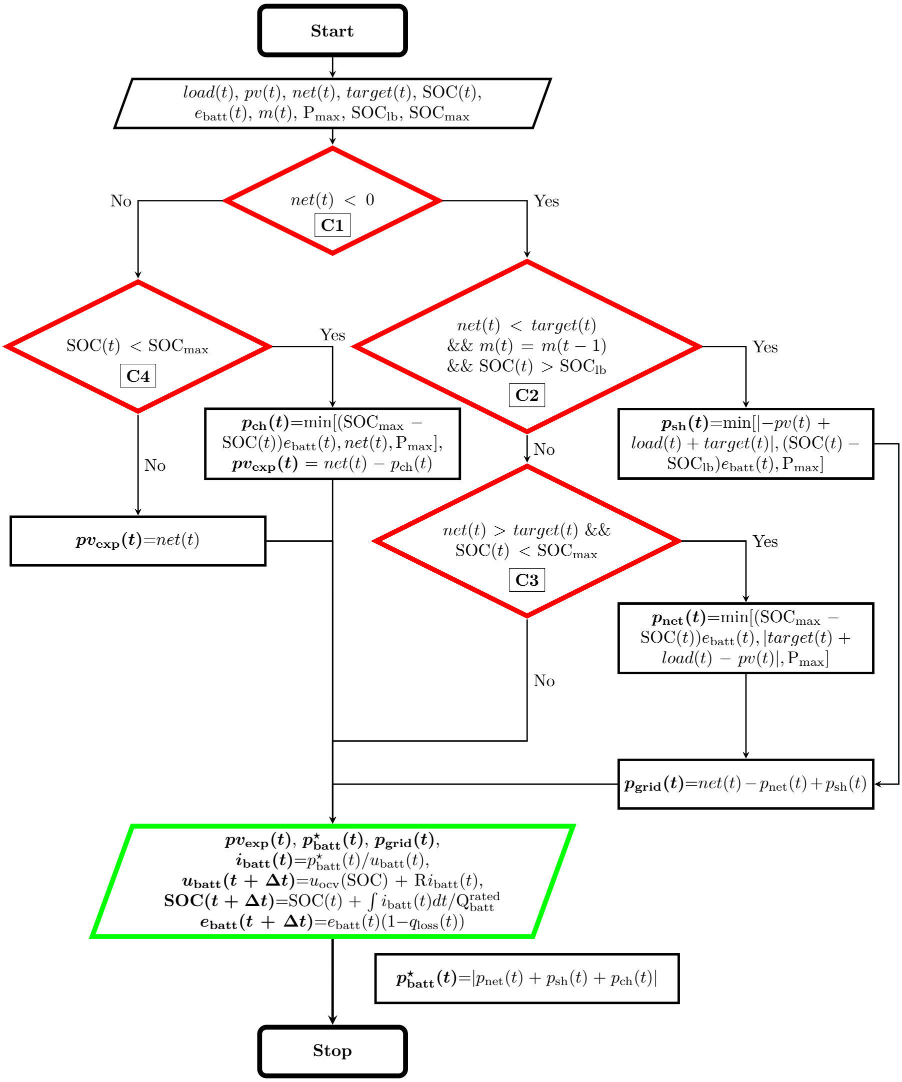

Figure D.2: Flow chart of battery charge and discharge control for peak-shaving with PV.

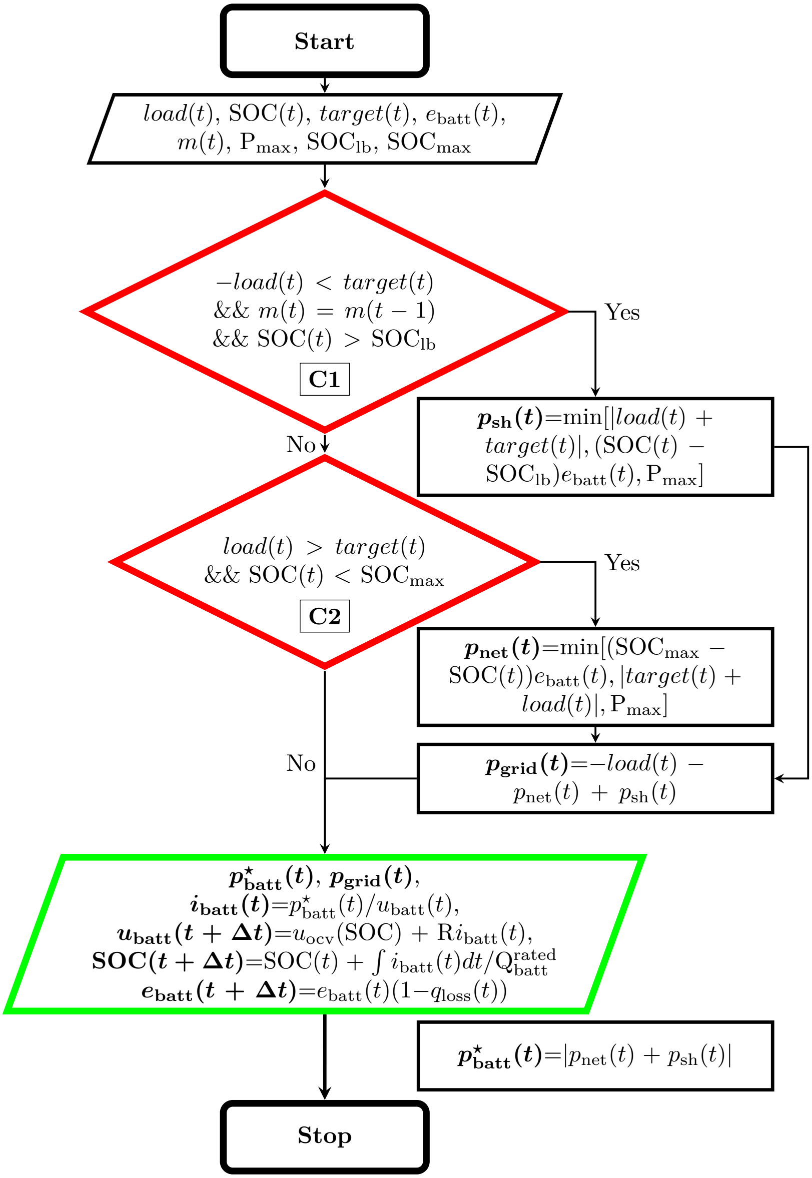

Figure D.3: Flow chart of battery charge and discharge control for peak-shaving without PV.

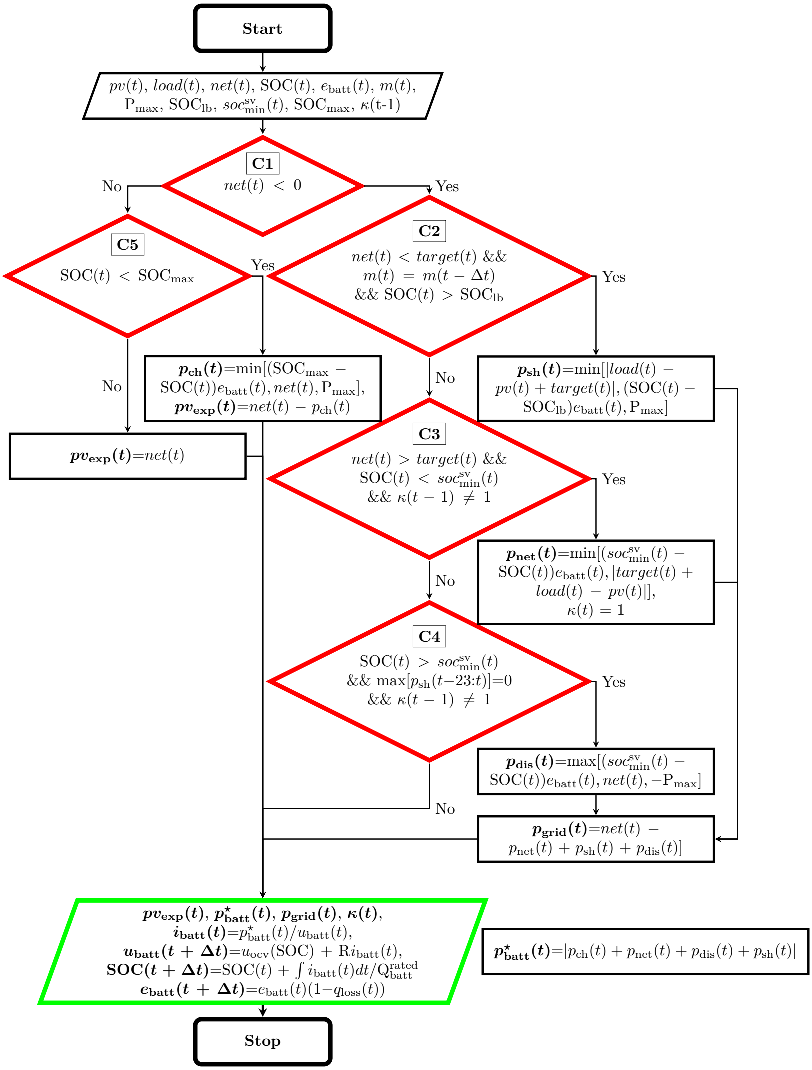

Figure D.4: Flow chart of battery charge and discharge control for rule-based multi-objective (MO) dispatch.

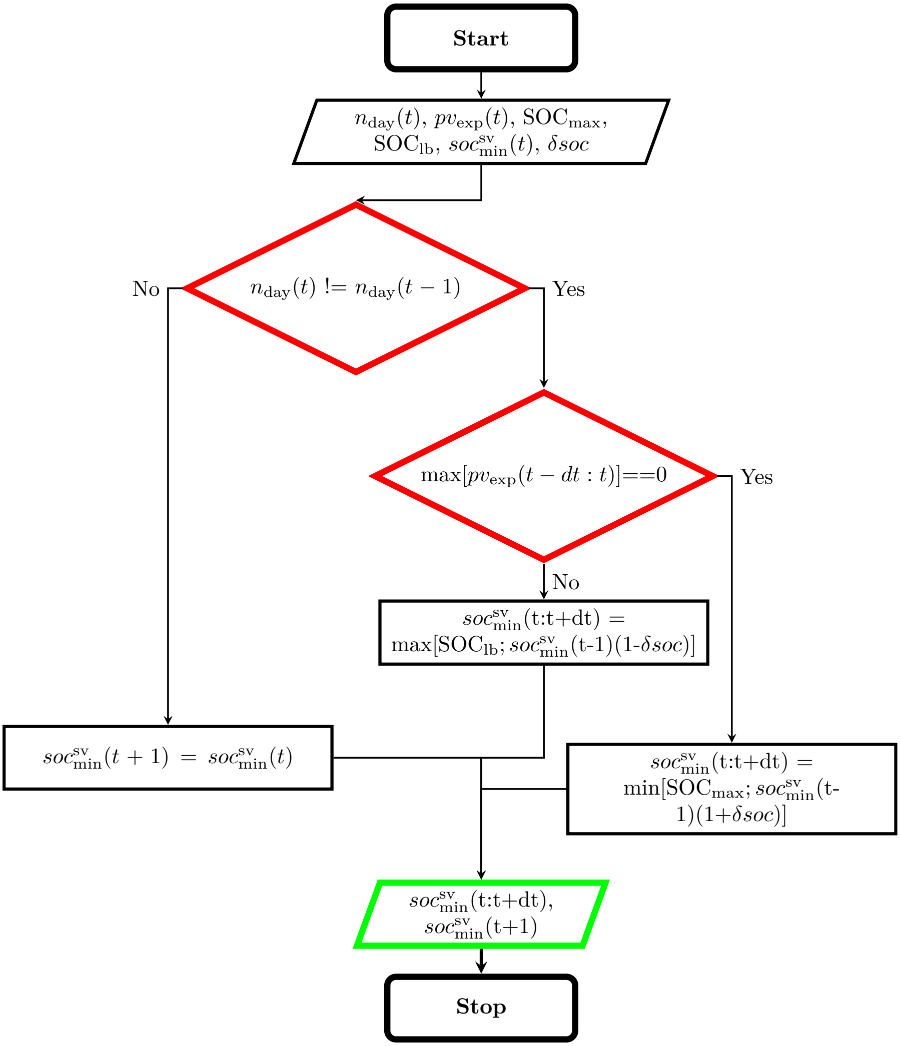

Figure D.5: Rule-based operation of the minimum state-of-charge variation, $soc^{sv}_{min}(t)$, used in Fig. D.4.

REFERENCES

[1] IEA, “Buildings,” International Energy Agency, Tech. Rep., 2022.

[2] European Commission, “Proposal for a directive of the european parliament and of the council on the energy performance of buildings (recast),” *Brussels*, 2021.

[3] G. Masson and I. Kaizuka, “Trends in photovoltaic applications 2020.,” International Energy Agency Photovoltaic Power Systems Programme, Tech. Rep., 2020.

[4] IEA, *Share of cumulative power capacity by technology, 2010-2027*, `https://www.iea.org/data-and-statistics/charts/share-of-cumulative-power-capacity-by-technology-2010-2027`, IEA. Licence: CC BY 4.0, 2022.

[5] A. T. Elsayed, A. A. Mohamed, and O. A. Mohammed, “DC microgrids and distribution systems: An overview,” *Electric Power Systems Research*, vol. 119, pp. 407–417, 2015.

[6] B. T. Patterson, “DC, come home: DC microgrids and the birth of the" enernet",” *IEEE Power and Energy Magazine*, vol. 10, no. 6, pp. 60–69, 2012.

[7] A. Chub, D. Vinnikov, O. Korkh, M. Malinowski, and S. Kouro, “Ultrawide voltage gain range microconverter for integration of silicon and thin-film photovoltaic modules in dc microgrids,” *IEEE Transactions on Power Electronics*, 2021.

[8] E. Rodriguez-Diaz, M. Savaghebi, J. C. Vasquez, and J. M. Guerrero, “An overview of low voltage DC distribution systems for residential applications,” in *2015 IEEE 5th International Conference on Consumer Electronics-Berlin (ICCE-Berlin)*, IEEE, 2015, pp. 318–322.

[9] V. Vossos, K. Johnson, M. Kloss, M. Khattar, D. Gerber, and R. Brown, “Review of DC power distribution in buildings: A technology and market assessment,” *LBNL Report, Berkeley*, 2017.

[10] F. Dastgeer, H. E. Gelani, H. M. Anees, Z. J. Paracha, and A. Kalam, “Analyses of efficiency/energy-savings of DC power distribution systems/microgrids: Past, present and future,” *International Journal of Electrical Power & Energy Systems*, vol. 104, pp. 89–100, 2019.

[11] D. L. Gerber, V. Vossos, W. Feng, C. Marnay, B. Nordman, and R. Brown, “A simulation-based efficiency comparison of AC and DC power distribution networks in commercial buildings,” *Applied Energy*, vol. 210, pp. 1167–1187, 2018.

[12] B. Glasgo, I. L. Azevedo, and C. Hendrickson, “Expert assessments on the future of direct current in buildings,” *Environmental Research Letters*, vol. 13, no. 7, p. 074 004, 2018.

[13] H. E. Gelani, F. Dastgeer, M. Nasir, S. Khan, and J. M. Guerrero, “AC vs. DC distribution efficiency: Are we on the right path?” *Energies*, vol. 14, no. 13, p. 4039, 2021.

[14] K. Spiliotis, J. E. Gonçalves, D. Saelens, K. Baert, and J. Driesen, “Electrical system architectures for building-integrated photovoltaics: A comparative analysis using a modelling framework in modelica,” *Applied Energy*, vol. 261, p. 114 247, 2020.

[15] H. Erteza Gelani, F. Dastgeer, S. A. Ali Shah, *et al.*, “Comparative efficiency and sensitivity analysis of ac and dc power distribution paradigms for residential localities,” *Sustainability*, vol. 14, no. 13, p. 8220, 2022.

[16] J. Hoppmann, J. Volland, T. S. Schmidt, and V. H. Hoffmann, “The economic viability of battery storage for residential solar photovoltaic systems–a review and a simulation model,” *Renewable and Sustainable Energy Reviews*, vol. 39, pp. 1101–1118, 2014.

[17] T. Beck, H. Kondziella, G. Huard, and T. Bruckner, "Assessing the influence of the temporal resolution of electrical load and pv generation profiles on self-consumption and sizing of pv-battery systems," *Applied energy*, vol. 173, pp. 331–342, 2016.

[18] S. Schopfer, V. Tiefenbeck, and T. Staake, "Economic assessment of photovoltaic battery systems based on household load profiles," *Applied energy*, vol. 223, pp. 229–248, 2018.

[19] M. Bortolini, M. Gamberi, and A. Graziani, "Technical and economic design of photovoltaic and battery energy storage system," *Energy Conversion and Management*, vol. 86, pp. 81–92, 2014.

[20] A. Pena-Bello, M. Burer, M. K. Patel, and D. Parra, "Optimizing pv and grid charging in combined applications to improve the profitability of residential batteries," *Journal of Energy Storage*, vol. 13, pp. 58–72, 2017.

[21] U. Mulleriyawage and W. Shen, "Optimally sizing of battery energy storage capacity by operational optimization of residential pv-battery systems: An australian household case study," *Renewable Energy*, vol. 160, pp. 852–864, 2020.

[22] M. I. Hlal, V. K. Ramachandaramurthy, A. Sarhan, A. Pouryekta, and U. Subramaniam, "Optimum battery depth of discharge for off-grid solar pv/battery system," *Journal of Energy Storage*, vol. 26, p. 100 999, 2019.

[23] A. Dietrich and C. Weber, "What drives profitability of grid-connected residential pv storage systems? a closer look with focus on germany," *Energy Economics*, vol. 74, pp. 399–416, 2018.

[24] B. Battke, T. S. Schmidt, D. Grosspietsch, and V. H. Hoffmann, "A review and probabilistic model of lifecycle costs of stationary batteries in multiple applications," *Renewable and Sustainable Energy Reviews*, vol. 25, pp. 240–250, 2013.

[25] D. Parra, M. Gillott, S. A. Norman, and G. S. Walker, "Optimum community energy storage system for pv energy time-shift," *Applied Energy*, vol. 137, pp. 576–587, 2015.

[26] S. Vonsien and R. Madlener, “Li-ion battery storage in private households with pv systems: Analyzing the economic impacts of battery aging and pooling,” *Journal of Energy Storage*, vol. 29, p. 101 407, 2020.

[27] E. Tervo, K. Agbim, F. DeAngelis, J. Hernandez, H. K. Kim, and A. Odukomaiya, “An economic analysis of residential photovoltaic systems with lithium ion battery storage in the united states,” *Renewable and Sustainable Energy Reviews*, vol. 94, pp. 1057–1066, 2018.

[28] E. A. Grunditz and T. Thiringer, “Characterizing bev powertrain energy consumption, efficiency, and range during official and drive cycles from gothenburg, sweden,” *IEEE Transactions on Vehicular Technology*, vol. 65, no. 6, pp. 3964–3980, 2015.

[29] S. Skoog, “Parameterization of equivalent circuit models for high power lithium-ion batteries in hev applications,” in *2016 18th European Conference on Power Electronics and Applications (EPE’16 ECCE Europe)*, IEEE, 2016, pp. 1–10.

[30] O. Theliander, A. Kersten, M. Kuder, E. Grunditz, and T. Thiringer, “Lifep0 4 battery modeling and drive cycle loss evaluation in cascaded h-bridge inverters for vehicles,” in *2019 IEEE Transportation Electrification Conference and Expo (ITEC)*, IEEE, 2019, pp. 1–7.

[31] A. Chaudhry, “Investigation of lithium-ion battery parameters using pulses and eis,” *BSc. Thesis, Chalmers University of Technology*, 2018.

[32] European Commission, *Reducing emissions from aviation*, `https://climate.ec.europa.eu/eu-action/transport-emissions/reducing-emissions-aviation_en#links`, Accessed: 06–March–2023.

[33] International Civil Aviation Organization, *Trends in emissions that affect climate change*, `https://www.icao.int/environmental-protection/Pages/ClimateChange_Trends.aspx`, Accessed: 06–March–2023.

[34] A. D. Cristea, “The role of aviation networks for urban development,” *Journal of Regional Science*, 2017.

[35] B. Graver, D. Rutherford, and S. Zheng, “Co2 emissions from commercial aviation 2013, 2018, and 2019,” The International Council on Clean Transportation, Tech. Rep., 2020.

[36] A. W. Schäfer, S. R. Barrett, K. Doyme, *et al.*, “Technological, economic and environmental prospects of all-electric aircraft,” *Nature Energy*, vol. 4, no. 2, pp. 160–166, 2019.

[37] B. Hou, S. Bose, and K. Haran, “Powering electric aircraft at o’hare airport: A case study,” in *2020 IEEE Power & Energy Society General Meeting (PESGM)*, IEEE, 2020, pp. 1–5.

[38] S. L. B. Santa, J. M. P. Ribeiro, G. Mazon, J. Schneider, R. L. Barcelos, J. B. S. O. de Andrade, *et al.*, “A green airport model: Proposition based on social and environmental management systems,” *Sustainable Cities and Society*, vol. 59, p. 102 160, 2020.

[39] Y. Xiang, H. Cai, J. Liu, and X. Zhang, “Techno-economic design of energy systems for airport electrification: A hydrogen-solar-storage integrated microgrid solution,” *Applied energy*, vol. 283, p. 116 374, 2021.

[40] B. J. Brelje and J. R. Martins, “Electric, hybrid, and turboelectric fixed-wing aircraft: A review of concepts, models, and design approaches,” *Progress in Aerospace Sciences*, vol. 104, pp. 1–19, 2019.

[41] M. Jiang, L. Qi, Z. Yu, *et al.*, “National level assessment of using existing airport infrastructures for photovoltaic deployment,” *Applied Energy*, vol. 298, p. 117 195, 2021.

[42] V. Vossos, K. Garbesi, and H. Shen, “Energy savings from direct-DC in US residential buildings,” *Energy and Buildings*, vol. 68, pp. 223–231, 2014.

[43] K. Siraj and H. A. Khan, “DC distribution for residential power networks—a framework to analyze the impact of voltage levels on energy efficiency,” *Energy Reports*, vol. 6, pp. 944–951, 2020.

[44] M. Starke, L. M. Tolbert, and B. Ozpineci, “AC vs. DC distribution: A loss comparison,” in *2008 IEEE/PES Transmission and Distribution Conference and Exposition*, IEEE, 2008, pp. 1–7.

[45] R. Weiss, L. Ott, and U. Boeke, “Energy efficient low-voltage DC-grids for commercial buildings,” in *2015 IEEE First International Conference on DC Microgrids (ICDCM)*, IEEE, 2015, pp. 154–158.

[46] G.-S. Seo, J. Baek, K. Choi, H. Bae, and B. Cho, “Modeling and analysis of DC distribution systems,” in *8th International Conference on Power Electronics-ECCE Asia*, IEEE, 2011, pp. 223–227.

[47] P. Ollas, “Energy savings using a direct-current distribution network in a pv & battery equipped residential building,” Department of Electrical Engineering, Chalmers University of Technology, Tech. Rep., 2020.

[48] F. Ahmad, F. Dastgeer, H. E. Gelani, S. Khan, and M. Nasir, “Comparative analyses of residential building efficiency for ac and dc distribution networks,” *Bulletin of the Polish Academy of Sciences: Technical Sciences*, e136732–e136732, 2021.

[49] F. Dastgeer and H. E. Gelani, “A comparative analysis of system efficiency for AC and DC residential power distribution paradigms,” *Energy and Buildings*, vol. 138, pp. 648–654, 2017.

[50] H. E. Gelani, F. Dastgeer, K. Siraj, M. Nasir, K. A. K. Niazi, and Y. Yang, “Efficiency comparison of ac and dc distribution networks for modern residential localities,” *Applied Sciences*, vol. 9, no. 3, p. 582, 2019.

[51] H. E. Gelani and F. Dastgeer, “Efficiency analyses of a DC residential power distribution system for the modern home,” *Advances in Electrical and Computer Engineering*, vol. 15, no. 1, pp. 135–143, 2015.

[52] N. D. Chinnathambi, K. Nagappan, C. R. Samuel, and K. Tamilarasu, “Internet of things-based smart residential building energy management system for a grid-connected solar photovoltaic-powered dc residential building,” *International Journal of Energy Research*, vol. 46, no. 2, pp. 1497–1517, 2022.

[53] M. Alshammari and M. Duffy, “Feasibility analysis of a dc distribution system for a 6 kw photovoltaic installation in ireland,” *Energies*, vol. 14, no. 19, p. 6265, 2021.

[54] A. Ammous, A. Assaedi, A. Al Ahdal, and K. Ammous, “Energy efficiency of a novel low voltage direct current supply for the future building,” *International Journal of Energy Research*, vol. 45, no. 10, pp. 15 360–15 371, 2021.

[55] B. Glasgo, I. L. Azevedo, and C. Hendrickson, “How much electricity can we save by using direct current circuits in homes? understanding the potential for electricity savings and assessing feasibility of a transition towards DC powered buildings,” *Applied energy*, vol. 180, pp. 66–75, 2016.

[56] V. Boscaino, J. Guerrero, I. Ciornei, L. Meng, E. R. Sanseverino, and G. Zizzo, "Online optimization of a multi-conversion-level dc home microgrid for system efficiency enhancement," *Sustainable cities and society*, vol. 35, pp. 417–429, 2017.

[57] E. R. Sanseverino, S. Favuzza, M. L. Di Silvestre, *et al.*, "Improved primary regulation for minimum energy losses in islanded microgrids," in *2017 IEEE PES Innovative Smart Grid Technologies Conference Europe (ISGT-Europe)*, IEEE, 2017, pp. 1–6.

[58] J. M. Guerrero, J. C. Vasquez, J. Matas, L. G. De Vicuña, and M. Castilla, "Hierarchical control of droop-controlled ac and dc microgrids—a general approach toward standardization," *IEEE Transactions on industrial electronics*, vol. 58, no. 1, pp. 158–172, 2010.

[59] V. Nasirian, A. Davoudi, F. L. Lewis, and J. M. Guerrero, "Distributed adaptive droop control for dc distribution systems," *IEEE Transactions on Energy Conversion*, vol. 29, no. 4, pp. 944–956, 2014.

[60] L. Meng, T. Dragicevic, J. C. Vasquez, and J. M. Guerrero, "Tertiary and secondary control levels for efficiency optimization and system damping in droop controlled dc–dc converters," *IEEE Transactions on Smart Grid*, vol. 6, no. 6, pp. 2615–2626, 2015.

[61] Y. Ru, J. Kleissl, and S. Martinez, "Storage size determination for grid-connected photovoltaic systems," *IEEE Transactions on sustainable energy*, vol. 4, no. 1, pp. 68–81, 2012.

[62] P. Mirzania, N. Balta-Ozkan, and A. Ford, "An innovative viable model for community-owned solar pv projects without fit: Comprehensive techno-economic assessment," *Energy Policy*, vol. 146, p. 111 727, 2020.

[63] D. Parra and M. K. Patel, "Effect of tariffs on the performance and economic benefits of pv-coupled battery systems," *Applied Energy*, vol. 164, pp. 175–187, 2016.

[64] N. Munzke, B. Schwarz, F. Büchle, and M. Hiller, "Evaluation of the efficiency and resulting electrical and economic losses of photovoltaic home storage systems," *Journal of Energy Storage*, vol. 33, p. 101 724, 2021.

[65] N. Munzke, F. Büchle, A. Smith, and M. Hiller, “Influence of efficiency, aging and charging strategy on the economic viability and dimensioning of photovoltaic home storage systems,” *Energies*, vol. 14, no. 22, p. 7673, 2021.

[66] V. Bertsch, J. Geldermann, and T. Lühn, “What drives the profitability of household pv investments, self-consumption and self-sufficiency?” *Applied Energy*, vol. 204, pp. 1–15, 2017.

[67] A. Pena-Bello, E. Barbour, M. C. Gonzalez, S. Yilmaz, M. K. Patel, and D. Parra, “How does the electricity demand profile impact the attractiveness of pv-coupled battery systems combining applications?” *Energies*, vol. 13, no. 15, p. 4038, 2020.

[68] Y. Zhang, T. Ma, P. E. Campana, Y. Yamaguchi, and Y. Dai, “A techno-economic sizing method for grid-connected household photovoltaic battery systems,” *Applied Energy*, vol. 269, p. 115 106, 2020.

[69] C. Truong, M. Naumann, R. Karl, M. Müller, A. Jossen, and H. Hesse, “Economics of residential photovoltaic battery systems in germany: The case of tesla’s powerwall,” *Batteries*, vol. 2, no. 2, p. 14, 2016.

[70] J. Weniger, T. Tjaden, J. Bergner, and V. Quaschning, “Sizing of battery converters for residential pv storage systems,” *Energy Procedia*, vol. 99, pp. 3–10, 2016.

[71] C. Goebel, V. Cheng, and H.-A. Jacobsen, “Profitability of residential battery energy storage combined with solar photovoltaics,” *Energies*, vol. 10, no. 7, p. 976, 2017.

[72] M. Astaneh, R. Roshandel, R. Dufo-López, and J. L. Bernal-Agustín, “A novel framework for optimization of size and control strategy of lithium-ion battery based off-grid renewable energy systems,” *Energy conversion and management*, vol. 175, pp. 99–111, 2018.

[73] A. Micallef, J. M. Guerrero, and J. C. Vasquez, “New horizons for microgrids: From rural electrification to space applications,” *Energies*, vol. 16, no. 4, p. 1966, 2023.

[74] Z. Guo, B. Li, G. Taylor, and X. Zhang, “Infrastructure planning for airport microgrid integrated with electric aircraft and parking lot electric vehicles,” *eTransportation*, p. 100 257, 2023.

[75] S. Jin and Y. Li, “Analyzing the performance of electricity, heating, and cooling supply nexus in a hybrid energy system of airport under uncertainty,” *Energy*, vol. 272, p. 127 138, 2023.

[76] M. Alruwaili and L. Cipcigan, “Optimal annual operational cost of a hybrid renewable-based microgrid to increase the power resilience of a critical facility,” *Energies*, vol. 15, no. 21, p. 8040, 2022.

[77] H. Zhao, Y. Xiang, Y. Shen, *et al.*, “Resilience assessment of hydrogen-integrated energy system for airport electrification,” *IEEE Transactions on Industry Applications*, vol. 58, no. 2, pp. 2812–2824, 2021.

[78] L. Trainelli, F. Salucci, C. E. Riboldi, A. Rolando, and F. Bigoni, “Optimal sizing and operation of airport infrastructures in support of electric-powered aviation,” *Aerospace*, vol. 8, no. 2, p. 40, 2021.

[79] Y. Zhang, A. Lundblad, P. E. Campana, F. Benavente, and J. Yan, “Battery sizing and rule-based operation of grid-connected photovoltaic-battery system: A case study in sweden,” *Energy conversion and management*, vol. 133, pp. 249–263, 2017.

[80] A. Stephan, B. Battke, M. D. Beuse, J. H. Clausdeinken, and T. S. Schmidt, “Limiting the public cost of stationary battery deployment by combining applications,” *Nature Energy*, vol. 1, no. 7, pp. 1–9, 2016.

[81] X. Han, J. Garrison, and G. Hug, “Techno-economic analysis of pv-battery systems in switzerland,” *Renewable and Sustainable Energy Reviews*, vol. 158, p. 112 028, 2022.

[82] W. Seward, M. Qadrdan, and N. Jenkins, “Revenue stacking for behind the meter battery storage in energy and ancillary services markets,” *Electric Power Systems Research*, vol. 211, p. 108 292, 2022.

[83] S. Englberger, A. Jossen, and H. Hesse, “Unlocking the potential of battery storage with the dynamic stacking of multiple applications,” *Cell reports physical science*, vol. 1, no. 11, p. 100 238, 2020.

[84] A. Narula, “Modeling of ageing of lithium ion battery at low temperatures,” *Department of Electric Power Engineering Chalmers, Gothenburg*, 2014.

[85] Z. Geng, T. Thiringer, Y. Olofsson, J. Groot, and M. West, "On-board impedance diagnostics method of li-ion traction batteries using pseudo-random binary sequences," in *2018 20th European Conference on Power Electronics and Applications (EPE'18 ECCE Europe)*, IEEE, 2018, P–1.

[86] V. Johnson, "Battery performance models in advisor," *Journal of power sources*, vol. 110, no. 2, pp. 321–329, 2002.

[87] G. L. Plett, "Extended kalman filtering for battery management systems of lipb-based hev battery packs: Part 3. state and parameter estimation," *Journal of Power sources*, vol. 134, no. 2, pp. 277–292, 2004.

[88] S. Song, S. Munk-Nielsen, V. Knap, and C. Uhrenfeldt, "Performance evaluation of lithium-ion batteries (lifepo4 cathode) from novel perspectives using a new figure of merit, temperature distribution analysis, and cell package analysis," *Journal of Energy Storage*, vol. 44, p. 103 413, 2021.

[89] V. Ovejas and A. Cuadras, "Effects of cycling on lithium-ion battery hysteresis and overvoltage," *Scientific reports*, vol. 9, no. 1, pp. 1–9, 2019.

[90] S. Nejad, D. Gladwin, and D. Stone, "A systematic review of lumped-parameter equivalent circuit models for real-time estimation of lithium-ion battery states," *Journal of Power Sources*, vol. 316, pp. 183–196, 2016.

[91] E. Nyholm, J. Goop, M. Odenberger, and F. Johnsson, "Solar photovoltaic-battery systems in swedish households–self-consumption and self-sufficiency," *Applied energy*, vol. 183, pp. 148–159, 2016.

[92] G. Litjens, E. Worrell, and W. Van Sark, "Economic benefits of combining self-consumption enhancement with frequency restoration reserves provision by photovoltaic-battery systems," *Applied energy*, vol. 223, pp. 172–187, 2018.

[93] K. Heine, A. Thatte, and P. C. Tabares-Velasco, "A simulation approach to sizing batteries for integration with net-zero energy residential buildings," *Renewable energy*, vol. 139, pp. 176–185, 2019.

[94] Y. Liu, L. Zhang, J. Jiang, S. Wei, S. Liu, and W. Zhang, “A data-driven learning-based continuous-time estimation and simulation method for energy efficiency and coulombic efficiency of lithium ion batteries,” *Energies*, vol. 10, no. 5, p. 597, 2017.

[95] J. Kang, F. Yan, P. Zhang, and C. Du, “A novel way to calculate energy efficiency for rechargeable batteries,” *Journal of Power Sources*, vol. 206, pp. 310–314, 2012.

[96] N. Collath, B. Tepe, S. Englberger, A. Jossen, and H. Hesse, “Aging aware operation of lithium-ion battery energy storage systems: A review,” *Journal of Energy Storage*, vol. 55, p. 105 634, 2022.

[97] I. Bloom, B. Cole, J. Sohn, *et al.*, “An accelerated calendar and cycle life study of li-ion cells,” *Journal of power sources*, vol. 101, no. 2, pp. 238–247, 2001.

[98] J. Wang, P. Liu, J. Hicks-Garner, *et al.*, “Cycle-life model for graphite-lifepo4 cells,” *Journal of power sources*, vol. 196, no. 8, pp. 3942–3948, 2011.

[99] S. K. Fuller and S. R. Petersen, “Life cycle costing manual,” *NIST handbook*, vol. 135, 1995.

[100] P. L. C. García-Miguel, J. Alonso-Martínez, S. Arnaltes Gómez, M. García Plaza, and A. P. Asensio, “A review on the degradation implementation for the operation of battery energy storage systems,” *Batteries*, vol. 8, no. 9, p. 110, 2022.

[101] L. Calearo and M. Marinelli, “Profitability of frequency regulation by electric vehicles in denmark and japan considering battery degradation costs,” *World Electric Vehicle Journal*, vol. 11, no. 3, p. 48, 2020.

[102] C. S. Lai, Y. Jia, Z. Xu, *et al.*, “Levelized cost of electricity for photovoltaic/biogas power plant hybrid system with electrical energy storage degradation costs,” *Energy conversion and management*, vol. 153, pp. 34–47, 2017.

[103] A. Ahmadian, M. Sedghi, B. Mohammadi-ivatloo, A. Elkamel, M. A. Golkar, and M. Fowler, “Cost-benefit analysis of v2g implementation in distribution networks considering pevs battery degradation,” *IEEE Transactions on Sustainable Energy*, vol. 9, no. 2, pp. 961–970, 2017.

[104] R. Luthander, J. Widén, D. Nilsson, and J. Palm, "Photovoltaic self-consumption in buildings: A review," *Applied energy*, vol. 142, pp. 80–94, 2015.

[105] P. Ollas, J. Persson, C. Markusson, and U. Alfadel, "Impact of battery sizing on self-consumption, self-sufficiency and peak power demand for a low energy single-family house with pv production in sweden," in *2018 IEEE 7th World Conference on Photovoltaic Energy Conversion (WCPEC)(A Joint Conference of 45th IEEE PVSC, 28th PVSEC & 34th EU PVSEC)*, IEEE, 2018, pp. 0618–0623.

[106] IEC, "Conductors of insulated cables," International Electrotechnical Commission, Tech. Rep. IEC 60228:2004, 2004.

[107] C. P. Chioncel, D. Kohake, L. Augustinov, P. Chioncel, and G. O. Tirian, "Yield factors of a photovoltaic plant," *Acta Tech Corvin Bull Eng (Fascicule)*, vol. 2, pp. 63–66, 2010.

[108] A. M. Khalid, I. Mitra, W. Warmuth, and V. Schacht, "Performance ratio–crucial parameter for grid connected pv plants," *Renewable and Sustainable Energy Reviews*, vol. 65, pp. 1139–1158, 2016.

[109] Y. B. Assoa, D. Valencia-Caballero, E. Rico, T. Del Caño, and J. V. Furtado, "Performance of a large size photovoltaic module for façade integration," *Renewable Energy*, vol. 211, pp. 903–917, 2023.

[110] E. Fuster-Palop, C. Vargas-Salgado, J. C. Ferri-Revert, and J. Payá, "Performance analysis and modelling of a 50 mw grid-connected photovoltaic plant in spain after 12 years of operation," *Renewable and Sustainable Energy Reviews*, vol. 170, p. 112 968, 2022.

[111] International Electrotechnical Commission, *Photovoltaic system performance monitoring-guidlines for measurement, data exchange and analysis*, 1998.

[112] International Electrotechnical Commission, *Terrestrial photovoltaic (pv) modules - design qualification and type approval - part 2: Test procedures*, 2017.

[113] International Electrotechnical Commission, *Photovoltaic system performance - part 1: Monitoring*, 2017.

[114] T. Dierauf, A. Growitz, S. Kurtz, J. L. B. Cruz, E. Riley, and C. Hansen, "Weather-corrected performance ratio," National Renewable Energy Lab.(NREL), Golden, CO (United States), Tech. Rep., 2013.

[115] A. Louwen, A. C. de Waal, R. E. Schropp, A. P. Faaij, and W. G. van Sark, "Comprehensive characterisation and analysis of pv module performance under real operating conditions," *Progress in Photovoltaics: Research and Applications*, vol. 25, no. 3, pp. 218–232, 2017.

[116] N. G. Bhat, B. R. Prusty, and D. Jena, "Cumulant-based correlated probabilistic load flow considering photovoltaic generation and electric vehicle charging demand," *Frontiers in Energy*, vol. 11, no. 2, pp. 184–196, 2017.

[117] J. Hernández, F. Ruiz-Rodriguez, and F. Jurado, "Modelling and assessment of the combined technical impact of electric vehicles and photovoltaic generation in radial distribution systems," *Energy*, vol. 141, pp. 316–332, 2017.

[118] M. N. Kabir, Y. Mishra, and R. Bansal, "Probabilistic load flow for distribution systems with uncertain pv generation," *Applied Energy*, vol. 163, pp. 343–351, 2016.

[119] G. Yang, M. Zhou, B. Lin, and W. Du, "Optimal scheduling the wind-solar-storage hybrid generation system considering wind-solar correlation," in *2013 IEEE PES Asia-Pacific Power and Energy Engineering Conference (APPEEC)*, IEEE, 2013, pp. 1–6.

[120] F. Issi and O. Kaplan, "The determination of load profiles and power consumptions of home appliances," *Energies*, vol. 11, no. 3, p. 607, 2018.

[121] M. Pipattanasomporn, M. Kuzlu, S. Rahman, and Y. Teklu, "Load profiles of selected major household appliances and their demand response opportunities," *IEEE Transactions on Smart Grid*, vol. 5, no. 2, pp. 742–750, 2013.

[122] H. Chen and C. Markusson, "Demand controlled ventilation in residential buildings," in *Cold Climate HVAC Conference*, Springer, 2018, pp. 111–122.

[123] P. Levin *et al.*, "Brukarindata för energiberäkningar i bostäder," *SVEBY, Tech. Rep.*, 2009.

[124] B. Stephens, J. A. Siegel, and A. Novoselac, "Operational characteristics of residential and light-commercial air-conditioning systems in a hot and humid climate zone," *Building and Environment*, vol. 46, no. 10, pp. 1972–1983, 2011.

[125] NREL, *System advisor model (sam)*, 2021.

[126] M. Z. Jacobson and V. Jadhav, "World estimates of pv optimal tilt angles and ratios of sunlight incident upon tilted and tracked pv panels relative to horizontal panels," *Solar Energy*, vol. 169, pp. 55–66, 2018.

[127] H. E. Beck, N. E. Zimmermann, T. R. McVicar, N. Vergopolan, A. Berg, and E. F. Wood, "Present and future köppen-geiger climate classification maps at 1-km resolution," *Scientific data*, vol. 5, no. 1, pp. 1–12, 2018.

[128] Climate.OneBuilding.Org, *Repository of free climate data for building performance simulation*, `https://climate.onebuilding.org/default.html`, Accessed: 30–November–2023.

[129] S. N. Backhaus, G. W. Swift, S. Chatzivasileiadis, *et al.*, "DC microgrids scoping study. estimate of technical and economic benefits," Los Alamos National Lab.(LANL), Los Alamos, NM (United States), Tech. Rep., 2015.

[130] D. Fregosi, S. Ravula, D. Brhlik, *et al.*, "A comparative study of DC and AC microgrids in commercial buildings across different climates and operating profiles," in *2015 IEEE First International Conference on DC Microgrids (ICDCM)*, IEEE, 2015, pp. 159–164.

[131] M. Noritake, K. Yuasa, T. Takeda, H. Hoshi, and K. Hirose, "Demonstrative research on DC microgrids for office buildings," in *2014 IEEE 36th International Telecommunications Energy Conference (INTELEC)*, IEEE, 2014, pp. 1–5.

[132] E. Planas, J. Andreu, J. I. Gárate, I. M. De Alegría, and E. Ibarra, "AC and DC technology in microgrids: A review," *Renewable and Sustainable Energy Reviews*, vol. 43, pp. 726–749, 2015.

[133] T. Castillo-Calzadilla, M. Cuesta, C. Olivares-Rodriguez, A. Macarulla, J. Legarda, and C. Borges, “Is it feasible a massive deployment of low voltage direct current microgrids renewable-based? a technical and social sight,” *Renewable and Sustainable Energy Reviews*, vol. 161, p. 112 198, 2022.

[134] A. Khorsandi, M. Ashourloo, H. Mokhtari, and R. Iravani, “Automatic droop control for a low voltage dc microgrid,” *IET Generation, Transmission & Distribution*, vol. 10, no. 1, pp. 41–47, 2016.

[135] E. Alliance, “380 vDC architectures for the modern data center,” *EMerge Alliance, San Ramon, CA, USA*, 2013.

[136] D. E. Geary, D. P. Mohr, D. Owen, M. Salato, and B. Sonnenberg, “380v DC eco-system development: Present status and future challenges,” in *Intelec 2013; 35th International Telecommunications Energy Conference, SMART POWER AND EFFICIENCY*, VDE, 2013, pp. 1–6.

[137] D. J. Becker and B. Sonnenberg, “DC microgrids in buildings and data centers,” in *2011 IEEE 33rd International Telecommunications Energy Conference (INTELEC)*, IEEE, 2011, pp. 1–7.

[138] U. Manandhar, A. Ukil, and T. K. K. Jonathan, “Efficiency comparison of DC and AC microgrid,” in *2015 IEEE Innovative Smart Grid Technologies-Asia (ISGT ASIA)*, IEEE, 2015, pp. 1–6.

[139] D. L. Gerber, R. Liou, and R. Brown, “Energy-saving opportunities of direct-DC loads in buildings,” *Applied Energy*, vol. 248, pp. 274–287, 2019.

[140] ISO, “Electrically propelled road vehicles — safety specifications — part 1: Rechargeable energy storage system (ress),” International Organization for Standardization, Tech. Rep. ISO 6469-1:2019, 2019.

[141] F. Spertino, F. Corona, and P. Di Leo, “Limits of advisability for master–slave configuration of dc–ac converters in photovoltaic systems,” *IEEE Journal of Photovoltaics*, vol. 2, no. 4, pp. 547–554, 2012.

[142] F. Gao, R. Kang, J. Cao, and T. Yang, “Primary and secondary control in dc microgrids: A review,” *Journal of Modern Power Systems and Clean Energy*, vol. 7, no. 2, pp. 227–242, 2019.

[143] R. Luthander, J. Widén, J. Munkhammar, and D. Lingfors, “Self-consumption enhancement and peak shaving of residential photovoltaics using storage and curtailment,” *Energy*, vol. 112, pp. 221–231, 2016.

[144] V. Vossos, D. Gerber, Y. Bennani, R. Brown, and C. Marnay, “Techno-economic analysis of dc power distribution in commercial buildings,” *Applied energy*, vol. 230, pp. 663–678, 2018.

[145] E. Wikner and T. Thiringer, “Extending battery lifetime by avoiding high soc,” *Applied Sciences*, vol. 8, no. 10, p. 1825, 2018.

[146] V. Vossos, D. L. Gerber, M. Gaillet-Tournier, *et al.*, “Adoption pathways for dc power distribution in buildings,” *Energies*, vol. 15, no. 3, p. 786, 2022.

[147] N. Somakettarin and T. Funaki, “Study on factors for accurate open circuit voltage characterizations in mn-type li-ion batteries,” *Batteries*, vol. 3, no. 1, p. 8, 2017.

[148] M. S. Ahmed, S. A. Raihan, and B. Balasingam, “A scaling approach for improved state of charge representation in rechargeable batteries,” *Applied Energy*, vol. 267, p. 114 880, 2020.

[149] A. Fly and R. Chen, “Rate dependency of incremental capacity analysis (dq/dv) as a diagnostic tool for lithium-ion batteries,” *Journal of Energy Storage*, vol. 29, p. 101 329, 2020.

[150] H. C. Hesse, M. Schimpe, D. Kucevic, and A. Jossen, “Lithium-ion battery storage for the grid—a review of stationary battery storage system design tailored for applications in modern power grids,” *Energies*, vol. 10, no. 12, p. 2107, 2017.

[151] M. Sandelic, A. Sangwongwanich, and F. Blaabjerg, “Reliability evaluation of pv systems with integrated battery energy storage systems: Dc-coupled and ac-coupled configurations,” *Electronics*, vol. 8, no. 9, p. 1059, 2019.

[152] C. Patsios, B. Wu, E. Chatzinikolaou, *et al.*, “An integrated approach for the analysis and control of grid connected energy storage systems,” *Journal of Energy Storage*, vol. 5, pp. 48–61, 2016.

[153] Z. Zhou, B. Duan, Y. Kang, N. Cui, Y. Shang, and C. Zhang, “A low-complexity state of charge estimation method for series-connected lithium-ion battery pack used in electric vehicles,” *Journal of Power Sources*, vol. 441, p. 226 972, 2019.

[154] R. L. Fares and M. E. Webber, “The impacts of storing solar energy in the home to reduce reliance on the utility,” *Nature Energy*, vol. 2, no. 2, p. 17 001, 2017.

[155] A. A. Kebede, T. Coosemans, M. Messagie, *et al.*, “Techno-economic analysis of lithium-ion and lead-acid batteries in stationary energy storage application,” *Journal of Energy Storage*, vol. 40, p. 102 748, 2021.

[156] H. Alfredsson, J. Nyman, J. Nilsson, and I. Staack, “Infrastructure modeling for large-scale introduction of electric aviation,” in *35th International Electric Vehicle Symposium and Exhibition (EVS35) Oslo, Norway, June 11-15, 2022*, 2022.

[157] K. Qian, R. Fachrizal, J. Munkhammar, T. Ebel, and R. Adam, “The impact of considering state of charge dependent maximum charging powers on the optimal electric vehicle charging scheduling,” *IEEE Transactions on Transportation Electrification*, 2023.

[158] S. Sreenath, K. Sudhakar, A. Yusop, E. Cuce, and E. Solomin, “Analysis of solar pv glare in airport environment: Potential solutions,” *Results in Engineering*, vol. 5, p. 100 079, 2020.

[159] S. Sreenath, K. Sudhakar, and A. Yusop, “Solar photovoltaics in airport: Risk assessment and mitigation strategies,” *Environmental Impact Assessment Review*, vol. 84, p. 106 418, 2020.

[160] S. Barrett and P. DeVita, “Technical guidance for evaluating selected solar technologies on airports,” *Washington, ABD: Federal Aviation Administration*, 2018.

[161] aurora, *Helioscope*, 2022.

[162] NordPool, *Day-ahead prices*, `https://www.nordpoolgroup.com/en/Market-data1/Dayahead/Area-Prices/ALL1/Hourly/?view=table`, [Online; accessed 03–March–2023], 2023.

[163] J. Lindahl, A. Oller Westerberg, and V. K, *National survey report of pv power applications in sweden 2020, international energy agency (iea)*, 2021.

[164] D. Feldman, V. Ramasamy, R. Fu, A. Ramdas, J. Desai, and R. Margolis, “Us solar photovoltaic system and energy storage cost benchmark (q1 2020),” National Renewable Energy Lab.(NREL), Golden, CO (United States), Tech. Rep., 2021.

[165] C. Montes, R. Dorta-Guerra, B. González-Díaz, S. González-Pérez, L. Ocaña, and E. Llarena, “Study of the evolution of the performance ratio of photovoltaic plants operating in a utility-scale installation located at a subtropical climate zone using mixed-effects linear modeling,” *Applied Sciences*, vol. 12, no. 21, p. 11 306, 2022.

[166] E. Ogliari, S. Leva, M. Polenghi, and L. De Ciechi, “Comparative performance analysis of different pv plants in italy,” in *2023 IEEE International Conference on Environment and Electrical Engineering and 2023 IEEE Industrial and Commercial Power Systems Europe (EEEIC/I&CPS Europe)*, IEEE, 2023, pp. 1–6.

[167] A. Gopi, K. Sudhakar, N. W. Keng, and A. R. Krishnan, “Comparison of normal and weather corrected performance ratio of photovoltaic solar plants in hot and cold climates,” *Energy for Sustainable Development*, vol. 65, pp. 53–62, 2021.

[168] D. A. Quansah and M. S. Adaramola, “Assessment of early degradation and performance loss in five co-located solar photovoltaic module technologies installed in ghana using performance ratio time-series regression,” *Renewable energy*, vol. 131, pp. 900–910, 2019.

[169] M. Jaszczur, Q. Hassan, A. M. Abdulateef, and J. Abdulateef, “Assessing the temporal load resolution effect on the photovoltaic energy flows and self-consumption,” *Renewable Energy*, vol. 169, pp. 1077–1090, 2021.

[170] A. Rashid and G. Safari, “Technical performance evaluation of solar photovoltaic systems: A case study of eight pv systems on the swedish market installed at rise research facilities,” Mälardalen University, Tech. Rep., 2021.

[171] A. Livera, M. Theristis, E. Koumpli, *et al.*, “Data processing and quality verification for improved photovoltaic performance and reliability analytics,” *Progress in Photovoltaics: Research and Applications*, vol. 29, no. 2, pp. 143–158, 2021.

[172] G. Li, Z. Duan, L. Liang, *et al.*, “Outlier data mining method considering the output distribution characteristics for photovoltaic arrays and its application,” *Energy Reports*, vol. 6, pp. 2345–2357, 2020.

[173] H. Awad and M. Gül, “Load-match-driven design of solar pv systems at high latitudes in the northern hemisphere and its impact on the grid,” *Solar Energy*, vol. 173, pp. 377–397, 2018.